

INVESTIGATION OF STRUCTURAL AND ELECTRONIC PROPERTIES OF
ZNCDTE TERNARY ALLOY NANOSTRUCTURES

A THESIS SUBMITTED TO
THE GRADUATE SCHOOL OF NATURAL AND APPLIED SCIENCES
OF
MIDDLE EAST TECHNICAL UNIVERSITY

BY

MUSTAFA KURBAN

IN PARTIAL FULFILLMENT OF THE REQUIREMENTS
FOR
THE DEGREE OF DOCTOR OF PHILOSOPHY
IN
PHYSICS

April 2016

Approval of the Thesis:

**INVESTIGATION OF STRUCTURAL AND ELECTRONIC PROPERTIES
OF ZNCDTE TERNARY ALLOY NANOSTRUCTURES**

submitted by **MUSTAFA KURBAN** in partial fulfillment of the requirements for the degree of **Doctor of Philosophy in Physics Department, Middle East Technical University** by,

Prof. Dr. Gülbin Dural Ünver
Dean, Graduate School of **Natural and Applied Sciences**

Prof. Dr. Mehmet Zeyrek
Head of Department, **Physics**

Prof. Dr. Şakir Erkoç
Supervisor, **Physics Department, METU**

Examining Committee Members:

Prof. Dr. Hamit Yurtseven
Physics Department, METU

Prof. Dr. Şakir Erkoç
Physics Department, METU

Assoc. Prof. Dr. Hüseyin Oymak
Faculty of Engineering, Physics Group, Atılım University

Assoc. Prof. Dr. Hande Toffoli
Physics Department, METU

Assoc. Prof. Dr. Rengin Peköz
Faculty of Engineering, Physics Group, Atılım University

Date:20.04.2016

I hereby declare that all information in this document has been obtained and presented in accordance with academic rules and ethical conduct. I also declare that, as required by these rules and conduct, I have fully cited and referenced all material and results that are not original to this work.

Name, Last Name: Mustafa Kurban

Signature :

ABSTRACT

INVESTIGATION OF STRUCTURAL AND ELECTRONIC PROPERTIES OF ZNCDTE TERNARY ALLOY NANOSTRUCTURES

Kurban, Mustafa

Ph.D., Department of Physics

Supervisor: Prof. Dr. Şakir Erkoç

April 2016, 145 pages

Nanostructures, including II-VI compound semiconductors, have attracted enormous attention in a wide range of applications of nanotechnology due to the unusual mechanical, electrical and thermal properties under varying size, geometry, temperature and pressure when compared to corresponding bulk materials. However, these properties are not directly measurable by experiments because of the methods or the availability of the experimental tools, so theoretical models and computations play an important role in the study of the nanostructures to obtain detailed information on atomic and molecular structures. This is the reason why other techniques are being developed as simulation and modeling methods. This thesis aims to deepen into the structural and electronic properties of ZnCdTe ternary alloy nanostructures, such as nanoparticles and nanowires, by performing classical molecular dynamics computer simulations and density functional theory calculations.

Key Words: CdZnTe nanostructures, Molecular Dynamics Simulations, Density Functional Theory, Heat Capacity, Stretching, Compression.

ÖZ

ZNCDTE ÜÇLÜ ALAŞIM NANOYAPILARININ YAPILARI VE ELEKTRONİK ÖZELLİKLERİNİN İNCELENMESİ

Kurban, Mustafa

Doktora, Fizik Bölümü

Tez Yöneticisi : Prof. Dr. Şakir Erkoç

Nisan 2016, 145 sayfa

Yarıiletken nanoyapılar, değişen boyut, geometri, sıcaklık ve basınç gibi faktörler altında eşsiz mekanik, elektrik ve termal özelliklere sahip olduğundan nanoteknoloji uygulamalarında önemli bir yere sahiptir. Ancak nanoyapıların bu özellikleri, deneysel araçların kullanılabilirliği ve metodların yetersizliğinden dolayı doğrudan deneysel araştırmalar ile ölçülemez. Bu nedenle teorik modellemeler ve hesaplamalar, atomik ve moleküler yapılar hakkında detaylı bilgi elde etmek için önemlidir. Bu tezde, üçlü CdZnTe nanoyapılarının yapıları ve elektronik özellikleri klasik molekül-dinamiği benzetişimi ve yoğunluk fonksiyonu teorisi ile incelenecektir.

Anahtar Kelimeler: CdZnTe Nanoyapıları, Molekül-dinamiği Benzetişimleri, Yoğunluk Fonksiyoneli Kuramı, Isı sığası, Gerdirme, Sündürme.

To My Dearest Family

ACKNOWLEDGEMENTS

I would like to thank Prof. Dr. Şakir Erkoç for his invaluable support, kind guidance, patience, inspiration, encouragement through all steps of this thesis and giving me the opportunity of working with him. I am indebted to him for giving me so much of his time and educating me in various aspects of Molecular Dynamics and Density Functional Theory techniques. His willingness to help with anything at any time is greatly appreciated.

I would also like to thank to Dr. Emre S. Taşçı and Dr. O. Barış Malcıoğlu for helping me to develop the skills to finish my thesis. I would also like to thank to Atomic and Molecular Physics Group family. Moreover, I am grateful to Dr. Donald K. Ward for providing a recently developed CdZnTe bond order potential and some suggestions for my studies.

The numerical calculations reported in this paper were partially performed at TUBITAK ULAKBIM, High Performance and Grid Computing Center (TRUBA resources).

Many thanks to my family for their love, moral support and pray especially to my wife, my parents and brothers. In addition, my thanks go to all my relatives and friends.

Finally, I would like to thank the members of the jury for their reviewing my thesis and also their instructive and constructive comments.

TABLE OF CONTENTS

ABSTRACT	v
ÖZ	vii
ACKNOWLEDGEMENTS	viii
TABLE OF CONTENTS	ix
LIST OF FIGURES	xii
LIST OF TABLES	xx
CHAPTERS	
1. INTRODUCTION	1
1.2. Physical properties of CdZnTe	2
1.2.1 Crystal Structure.....	2
1.2.2 Band Structure.....	5
1.2.3. Phase Diagram	7
1.3. Potential Applications of CdZnTe	8
1.4. Nanostructured Materials	9
1.4.1 Zero-dimensional (0D) nanostructure	9
1.4.2 One-dimensional (1D) nanostructure	12
1.4.3 Two-dimensional (2D) nanostructure	14
2. METHODS OF CALCULATION	17
2.1 Molecular Dynamics	17
2.1.1 Algorithms to integrate the equations of motion.....	19
2.1.1.1 Verlet Algorithm	19
2.1.1.2 Predictor-Corrector Algorithms	20
2.1.1.3 Nordsieck-Gear Predictor-Corrector Algorithm	20

2.1.1.4 Lanczos recursion algorithm	21
2.1.2 Potential Energy Functions	23
2.1.2.1 Lennard-Jones and Axilrod-Teller PEF	23
2.1.2.1 Analytical bond-order potential (BOP)	26
2.1.3 Periodic Boundary Conditions	27
2.2 Density Functional Theory	28
2.2.1 Born-Oppenheimer approximation	28
2.2.2 Hartree -Fock Approximation	29
2.2.3 The electron density	30
2.2.4 The Hohenberg–Kohn Theorem.....	31
2.2.5 The Kohn-Sham Theorem.....	32
2.2.6 Exchange-Correlation Functionals	33
2.2.7 Basis Sets.....	35
3. RESULTS AND DISCUSSION	37
3.1 Structural properties of $\text{Zn}_x\text{Cd}_{1-x}\text{Te}$ ($x=0.25, 0.50$ and 0.75) ternary nanorods: Molecular Dynamics Simulations	37
3.1.1 Introduction	37
3.1.2 Modelling and calculation procedure	37
3.1.3 Results and Discussions	39
3.2 Investigation of the structural properties of CdTe and ZnTe nanorods under heat treatment: Molecular Dynamics Simulations	46
3.2.1 Introduction	46
3.2.2 Modelling and calculation procedure	46
3.2.3 Results and Discussions	48
3.3 Mechanical properties of CdZnTe nanowires under uniaxial stretching and compression: A Molecular Dynamics Simulation Study	53

3.3.1 Introduction	53
3.3.2 Modelling and calculation procedure	53
3.3.3 Results and Discussions	55
3.4 Structural and electronic properties of $\text{Zn}_m\text{Cd}_n\text{Te}_k$ ($m+n+k = 2-4$) clusters: DFT calculations	62
3.4.1 Introduction	62
3.4.2 Modelling and calculation procedure	62
3.4.3 Results and Discussions	63
3.5 Structural, electronic and thermal properties of AB_6C_8 ternary CdZnTe cubic nanoparticles: MD simulations and DFT calculations	83
3.5.1 Introduction	83
3.5.2 Modelling and calculation procedure	83
3.5.3 Results and Discussions	87
3.6 Structural and thermal properties of Cd-Zn-Te ternary nanoparticles: Molecular-Dynamics Simulations	110
3.6.1 Introduction	110
3.6.2 Modelling and calculation procedure	110
3.6.3 Results and Discussions	112
4. CONCLUSIONS	125
REFERENCES	129
CURRICULUM VITAE	141

LIST OF FIGURES

FIGURES

Figure 1: Zinc Blende Structure	3
Figure 2: The X-ray diffraction curve for $\text{Cd}_{0.9}\text{Zn}_{0.1}\text{Te}$. [15].....	4
Figure 3. Band structure of CdTe [17].	5
Figure 4. Modulation of band-gap and lattice constant of CdTe by incorporation of Zn or Hg instead of Cd atoms [18].	6
Figure 5. Temperature-mole fraction phase diagram for CdTe-ZnTe pseudo-binary [19].	7
Figure 6. The LumaGem molecular breast imaging (MBI) camera is a dedicated breast imaging system with cadmium zinc telluride (CZT) digital detectors [20].	8
Figure 7. Types of nanocrystalline materials by the size of their structural elements: 0D clusters; 1D nanotubes, fibers and rods; 2D films and coats; 3D polycrystals [22].	9
Figure 8. TEM image of Silica nanoparticles (A) [31] and Gold–dendrimer nanoparticles and their biodistribution in vivo (B) [30].	10
Figure 9. CLSM images of CdTe NPs using covalent coupling (a) and (b) the layer-by-layer approach [36].	11
Figure 10. (a) The ZnO nanorods [41] and (b) SEM image from nanorods dispersed on a Si (001) substrate with a native oxide [42].	12
Figure 11. SEM micrograph of the CdZnTe Nanowires after 45 minutes of pulsed electrodeposition. (inset shows magnified image of the nanowires) [46].	14
Figure 12. Triplet configuration of atoms i, j and k in Eq. (2.18) [76].	24
Figure 13. Periodic boundary conditions in two dimensions [89].	27
Figure 14: Schematic diagram of exchange-correlation functionals [97].	34
Figure 15. The energetic relaxation plot for $\text{Zn}_{0.50}\text{Cd}_{0.50}\text{Te}$ nanorod at 600 K.	38
Figure 16. Side and cross section views of the generated structures of (a) $\text{Zn}_{0.25}\text{Cd}_{0.75}\text{Te}$ (b) $\text{Zn}_{0.50}\text{Cd}_{0.50}\text{Te}$ (c) $\text{Zn}_{0.75}\text{Cd}_{0.25}\text{Te}$ nanorod models.	39

Figure 17. The number of Zn atoms variation with temperature for $Zn_xCd_{1-x}Te$ nanorod models.	40
Figure 18. (a) The total interaction energies with respect to temperature and (b) the snapshots of $Zn_{0.25}Cd_{0.75}Te$ nanorod at different temperatures.	43
Figure 19. (a) The total interaction energies with respect to temperature and (b) the snapshots of $Zn_{0.50}Cd_{0.50}Te$ nanorod at different temperatures.	44
Figure 20. (a) The total interaction energies with respect to temperature and (b) the snapshots of $Zn_{0.75}Cd_{0.25}Te$ nanorod at different temperatures.	45
Figure 21. Side and cross section views of the generated structures of (a) ZnTe and (b) CdTe nanorod models.	47
Figure 22. Total energy variation in terms of temperature for ZnTe and CdTe nanorods.	48
Figure 23. The structures of ZnTe nanorod at different temperatures. Pictures show side and cross-section views.	50
Figure 24. The structures of CdTe nanorod at different temperatures. Pictures show side and cross-section views.	51
Figure 25. The number of atoms variation with temperature for ZnTe and CdTe nanorods.	52
Figure 26. Cd atom release with respect to temperature in CdTe nanorod [47].	52
Figure 27. The generated view of the modeled nanowires with (a) 263 atoms (model-1, M1) and (b) 641 atoms (model-2, M2).	53
Figure 28. (a) Stretching model: The NW is stretched a length ΔL along its length. (b) Compression model: The same NW is compressed a length ΔL along its length.	54
Figure 29. Strain energy (ΔE) with respect to strain (ΔL (%)) and the snapshots of stretching process for CdZnTe NW M1 at (a) 1 K and (b) 300 K.	57
Figure 30. Strain energy (ΔE) with respect to strain (ΔL (%)) and the snapshots of the corresponding stretched structures for CdZnTe NW M2 at (a) 1 K and (b) 300 K.	58
Figure 31. The snapshots of the CdZnTe NW M2 at 1 K until 19 compression steps. All the pictures show side views, except #19a is for side view, #19b is for cross view.	60

Figure 32. Dimer geometries (Zn is purple, Cd is grey and Te is orange), spin density (SD), charge density (CD) and electrostatic potential (ESP) pictures of dimers. Green (alpha spin) and blue (beta spin) colors represent the positive and negative spin density, respectively. Electrostatic potential picture: yellow represents positive potential and orange negative potential. The corresponding charge densities for dimer geometries are given in the parenthesis. The color is the same in the following figures.	65
Figure 33. Trimer geometries. The corresponding charge values for trimer geometries are given in the parenthesis.	67
Figure 34. Spin density (SD), charge density (CD) and electrostatic potential (ESP) pictures of trimers.	68
Figure 35. Tetramer geometries. The corresponding charge densities for tetramer geometries are given in the parenthesis.	72
Figure 36. Charge density (CD) and electrostatic potential (ESP) pictures of trimers.	73
Figure 37. HOMO (H) and LUMO (L) pictures of dimers and trimers. Green and red colors represent the positive and negative isosurfaces for HOMO and LUMO, respectively.	78
Figure 38. HOMO (H) and LUMO (L) pictures of tetramers. Green and red colors represent the positive and negative isosurfaces for HOMO and LUMO, respectively.	79
Figure 39. (a) Initial structures and (b) optimized geometries with two different views of the various CdZnTe nanostructures with 15 atoms (Zn is purple, Cd is grey and Te is orange).	86
Figure 40. The change in the structures of the $\text{Zn}_1\text{Cd}_6\text{Te}_8$ nanoparticle at various temperatures.	88
Figure 41. Variation of the order parameter R_{Cd} , R_{Zn} , and R_{Te} with various CdZnTe compounds at (a) 1 K and (b) 300 K.	91
Figure 42. Energy variation with temperature in terms of the composition of nanoparticles (a)-(f) with corresponding calculated heat capacity values C_v	93
Figure 43. Composition dependence of the heat capacity values for various CdZnTe nanoparticles.	97

Figure 44. The calculated excess charges of atoms in each model.	100
Figure 45. HOMO and LUMO pictures of the CdZnTe ternary nanoparticles. Green and red colors represent the positive and negative isosurfaces for HOMO and LUMO, respectively.	102
Figure 46. Charge density (CD) and electrostatic potential (ESP) pictures of CdZnTe ternary nanoparticles. ESP picture: yellow and orange colors represent positive and negative potential, respectively.	104
Figure 47. Spin density (SD) pictures of CdZnTe ternary nanoparticles with nonzero spin. Green (alpha spin) and blue (beta spin) colors represent the positive and negative spin density, respectively.	106
Figure 48. Density of states (DOS) spectra for CdZnTe ternary nanoparticles using Mulliken population analysis.	107
Figure 49. The initial structures of the Cd _{0.50} Zn _{0.50} Te spherical nanoparticle models generated from zinc-blend crystal structure for MD simulations.	111
Figure 50. Variation of the potential energy as a function of temperature according to the size and stoichiometry of the nanoparticles. (a) Cd _{0.25} Zn _{0.75} Te, (b) Cd _{0.50} Zn _{0.50} Te, and (c) Cd _{0.75} Zn _{0.25} Te.	112
Figure 51. Size dependence of the calculated heat capacity C_v for the Cd _{1-x} Zn _x Te nanoparticles in the temperature range 100 K-600 K.	114
Figure 52. Variation of the calculated heat capacity C_v as a function of (a) Zn and (b) Cd concentrations (x) for the sizes N=167, 239, 293 and 357.	115
Figure 53. Experimental heat capacity profile for CdZnTe bulk material. [136]. ...	116
Figure 54. Variation of the order parameter R_{Cd} , R_{Zn} , and R_{Te} with respect to size (N=167, 239, 293 and 357). (a) Cd _{0.25} Zn _{0.75} Te, (b) Cd _{0.50} Zn _{0.50} Te and (c) Cd _{0.75} Zn _{0.25} Te.	117
Figure 55. Variation of the order parameter R_{Cd} , R_{Zn} , and R_{Te} with respect to temperature. (a) Cd _{0.25} Zn _{0.75} Te, (b) Cd _{0.50} Zn _{0.50} Te and (c) Cd _{0.75} Zn _{0.25} Te.	119
Figure 56. The radial distribution function (RDF) of the Cd _{0.50} Zn _{0.50} Te nanoparticle with 357 atoms at (a) 100 K and (b) 600 K.	122
Figure 57. The structures of the Cd _{0.50} Zn _{0.50} Te spherical nanoparticle with 357 atoms at various temperatures.	123

LIST OF TABLES

TABLES

Table 1: Lattice Constants [13], [14].	3
Table 2. Potential parameters used in the calculations.....	25
Table 3. Number of atoms in the ZnCdTe nanorod models at different temperatures.	41
Table 4. Spectroscopic constants of the possible dimer combinations. Dissociation energy (D_e), equilibrium distance (r_e) the vibrational frequency (ω_e), total energy (E_T in Hartree), the multiplicities of the spin system ($2S+1$), the dipole moments (μ in Debye). E_T (Zn) = -226.126, E_T (Cd) = -166.937 and E_T (Te) = -7.974. The corresponding total energies for the triplet states are given in the parenthesis.....	64
Table 5. The binding energies (E_b , in eV), total energy (E_T , in Hartree), the multiplicities of the spin system ($2S+1$), and the dipole moments (μ , in Debyes) of trimer structures with lowest energy. The corresponding total energies for the triplet states are given in the parenthesis.	69
Table 6. The vibrational frequencies (ω , in cm^{-1}) of all the trimer structures with the lowest energy.....	70
Table 7. The binding (E_b , in eV) and total (E_T , in Hartree) energies, the multiplicities of the spin system ($2S+1$), and the dipole moments (μ , in Debyes) for tetramer structures with the lowest energy. The corresponding total energies for the triplet states are given in the parenthesis.	74
Table 8. Calculated vibration harmonic frequencies (in cm^{-1}) of all the tetramer structures with the lowest energy of $\text{Zn}_m\text{Cd}_n\text{Te}_k$ clusters for $m+n+k=4$. Zn_3Te , Cd_3Te and ZnCdTe_2 have one more frequency value 223.0, 163.5 and 285.5, respectively.	75
Table 9. HOMO, LUMO energies (in Hartree) and HOMO–LUMO gap energies (E_g , in eV) of $\text{Zn}_m\text{Cd}_n\text{Te}_k$ clusters for $m+n+k=4$. Entries with α and β correspond to $2S+1=3$, the rest correspond to $2S+1=1$	77

Table 10. Possible dissociation channels and energies (ΔE_d , in eV) of the stable $Zn_mCd_nTe_k$ clusters.	81
Table 11. Basis set data used in DFT calculations.....	84
Table 12. δ values (the deviation of morphology of the nanoparticles from a perfectly cubic structure).....	89
Table 13. Average distances of Cd, Zn and Te atoms.	89
Table 14. HOMO, LUMO energies (in a.u.), HOMO–LUMO gap energies (E_g), total energy (E_T) and the lowest energy multiplicities ($2S+1$) of the spin system for various CdZnTe compounds.....	98
Table 15. The total excess charges (q, in e) and the dipole moments (μ , in Debyes) for various CdZnTe nanoparticles.....	101

CHAPTER 1

INTRODUCTION

Nanostructures have attracted enormous attention in a great deal of applications in biomedical, optical and electronic fields because of the unusual mechanical, electrical and thermal properties under varying size and geometry when compared to corresponding bulk materials. Especially, many nanostructures including II-VI compound semiconductors have been studied both experimentally and theoretically due to their numerous important applications [1]–[3]. Among the semiconductors, cadmium-zinc-telluride (CdZnTe, CZT or $\text{Cd}_{1-x}\text{Zn}_x\text{Te}$) has been the subject of intensive research for its implementation into many commercial systems and variety of applications that are used in solar cells, optoelectronic devices, nano-field-effect transistors, x-ray and γ -ray detectors for medical, industrial imaging systems and security fields [4]–[8] as well as space applications at room temperature. This increasing interest is due to the special detection performance of CdZnTe due to its high average atomic number ensuring high stopping power, suitable wide band-gap giving high resistivity which allows low leakage-current, good electron transport properties, flexibility in configuring contacts and applying a homogeneous electrical field across the device [9], [10]. These features provide high energy resolution and efficient radiation detection at room temperature. However, CdZnTe devices still face many challenges and drawbacks. One of the drawbacks is the understanding of the surfaces of CdZnTe detectors and surface effects on detector quality and performance. Another major drawback is the quality of bulk crystals that are commercially available because commercial crystals have large concentrations of extended defects such as twins, grain boundaries, tellurium inclusions, precipitates and dislocations. Therefore, the focus of much of the research into CdZnTe at present is to eliminate the effect of these defects by improving the yield of the continuum of growth and limiting the quantity of crystal failures and impurities formed to produce material with high purity, large single crystal volumes.

Extensive literature survey revealed that little attention has been paid to cadmium-zinc-tellurium nanostructures in spite of their chemical and technological important. Therefore, in this thesis, the structural, electronic, mechanical and thermal properties of CdZnTe nanostructures such as nanorods (nanowires), small clusters and nanoparticles have been investigated. Using atomistic molecular dynamics method (MD) and density functional theory (DFT) one can get information to synthesize and develop a new functional nanostructured materials. By controlling the nanostructure size and by increasing the number of nanostructures such as nanoparticles and nanorods one can get information to guide the experimentalists. It should be noted that CdZnTe crystals have a variety of applications but the discussion is mostly about its nanostructures and a brief literature survey.

1.2. Physical Properties of CdZnTe

1.2.1 Crystal Structure

The CdZnTe compound crystallizes into the zinc-blende (ZB) (or Zinc Sulfide) structure as shown in Figure 1. In the alloy $\text{Cd}_{1-x}\text{Zn}_x\text{Te}$ the Zn atoms randomly substitute the Cd atoms of the crystal with a fraction of x. The structure of CdZnTe alloy is generally described as a face centered cubic lattice with a cubic crystal system given by

$$\sigma_1 = (0,0,0)$$

$$\sigma_2 = \left(\frac{1}{4}a, \frac{1}{4}a, \frac{1}{4}a\right)$$

The Zn and Cd concentration profiles determine the homogeneity of these mixed crystals, so x is crucial for obtaining a CdZnTe alloy with the required lattice parameter.

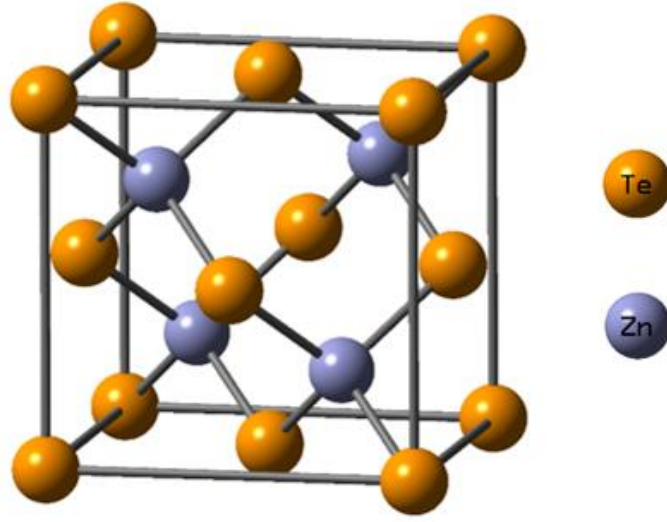


Figure 1: Zinc Blende Structure

The experimental lattice parameter of CdTe and ZnTe is 6.482 Å and 6.104 Å, respectively [11]. The CdZnTe lattice constant can therefore be expressed using Vegard's Law [12] given by

$$a(x) = a_1(1 - x) + a_2x. \quad (1.1)$$

In Eq. (1.1), a_1 is lattice parameter of CdTe and a_2 is lattice parameter of ZnTe, respectively. The difference in the lattice parameters shows that Zn substitution of Cd atoms result in a small variation in the average of the unit cell dimensions. Some lattice constants of CdZnTe alloy with different Zn concentrations are tabulated in Table 1.

Table 1: Lattice Constants [13], [14].

Compound	Lattice Parameter (Å)
Cd _{0.95} Zn _{0.05} Te	6.495
Cd _{0.9} Zn _{0.1} Te	6.441
Cd _{0.7} Zn _{0.3} Te	6.364
Cd _{0.5} Zn _{0.5} Te	6.287

The average lattice constant of the alloy $\text{Cd}_{1-x}\text{Zn}_x\text{Te}$ can also be found by Bragg's law:

$$n\lambda = 2d\sin(\theta) \quad (1.2)$$

In Eq. (1.2), λ and d are the wavelength of the incident radiation and the distance between crystal planes, respectively as well as θ and n are the angle of incidence and a positive integer, respectively. Lattice constant is proportional the distance d . Therefore, using the position of the diffraction peak, composition of $\text{Cd}_{1-x}\text{Zn}_x\text{Te}$ ternary alloy can be determined.

Figure 2 shows the X-ray diffraction curve for $\text{Cd}_{0.9}\text{Zn}_{0.1}\text{Te}$. The amount of Zn in $\text{Cd}_{0.9}\text{Zn}_{0.1}\text{Te}$ sample can be found from the position of the (220) peak which accurately determines the value of the lattice constant using Equation (1.2).

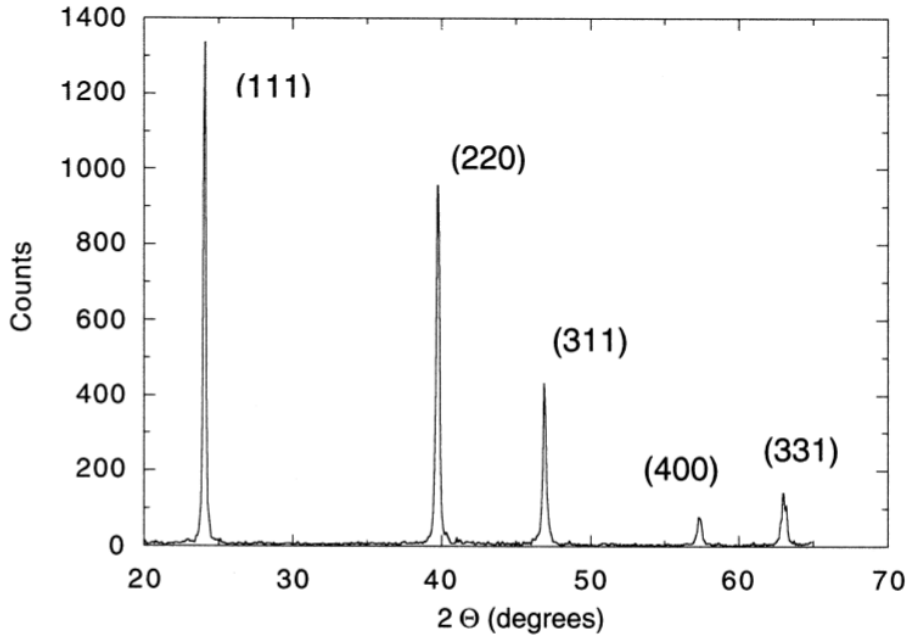


Figure 2: The X-ray diffraction curve for $\text{Cd}_{0.9}\text{Zn}_{0.1}\text{Te}$. [15].

The knowledge of the lattice constant is especially important in the infrared detector industry. Commercial infrared $\text{Hg}_{0.8}\text{Cd}_{0.2}\text{Te}$ detectors are mostly grown on

$\text{Cd}_{0.96}\text{Zn}_{0.04}\text{Te}$ substrates due to matching of lattice constants, which suppresses the formation of an interface stress.

1.2.2 Band Structure

Band theory, in the solid materials, is dependent on the spatial periodicity of a lattice. This property does not exist in an alloy material due to local fluctuations in the composition. Thus, it is difficult to obtain the band structure of ternary semiconductor CdZnTe . The band structure of CdZnTe is, in general, related with the structure of binary CdTe and ZnTe as a linear interpolation between those of two compounds. CdTe and ZnTe are binary alloy semiconductors with the forbidden gap and a direct band gap of 1.5 eV and 2.2 eV, respectively [16]. A direct band-gap materials are capable of emission of photon, thus these materials are useful for optical devices like light-emitting and laser diodes. **Figure 3** shows the band structure for CdTe binary alloy.

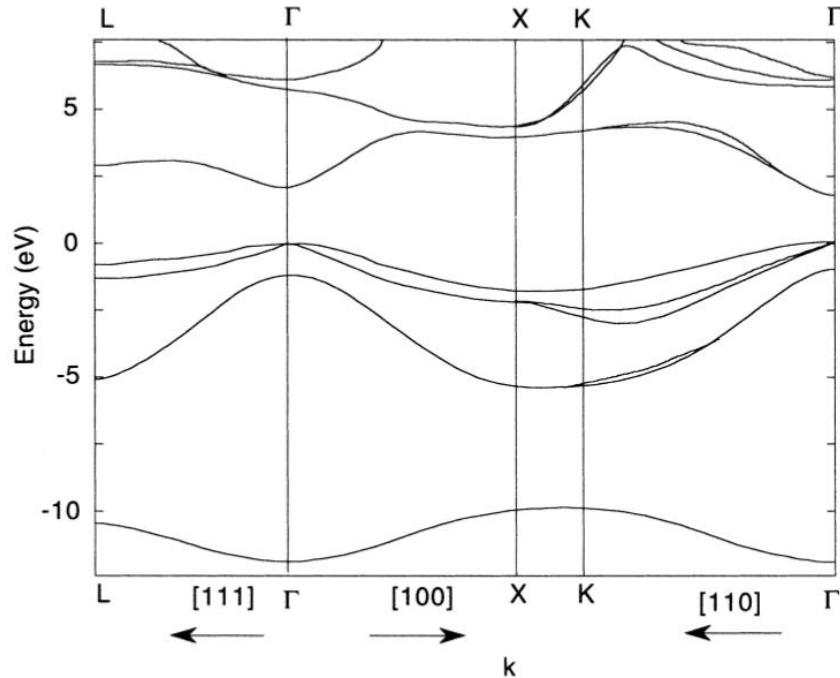


Figure 3. Band structure of CdTe [17].

The forbidden band-gap width can be modulated by a substitution of Cd atoms by atoms of Zn or Hg in the cadmium sublattice at room temperature. Figure 4 shows the modulation of band-gap with respect to the lattice constant for CdTe. The properties of CdTe may be improved by the addition of Zn to prepare the ternary alloy $\text{Cd}_x\text{Zn}_{1-x}\text{Te}$. Additional Zn atoms are randomly substituted throughout the crystal lattice for Cd atoms. The addition of the Zn reduces to the dislocation density in the crystal and to raise the band-gap energy. The increased band-gap decreases the number of thermal by generated carriers at room temperature resulting in a reduction in the detector noise due to leakage current in CdTe and allows for use at either lower photon energies or higher temperatures. CdZnTe crystals can also be grown to larger sizes at a reduced cost compared to CdTe crystals.

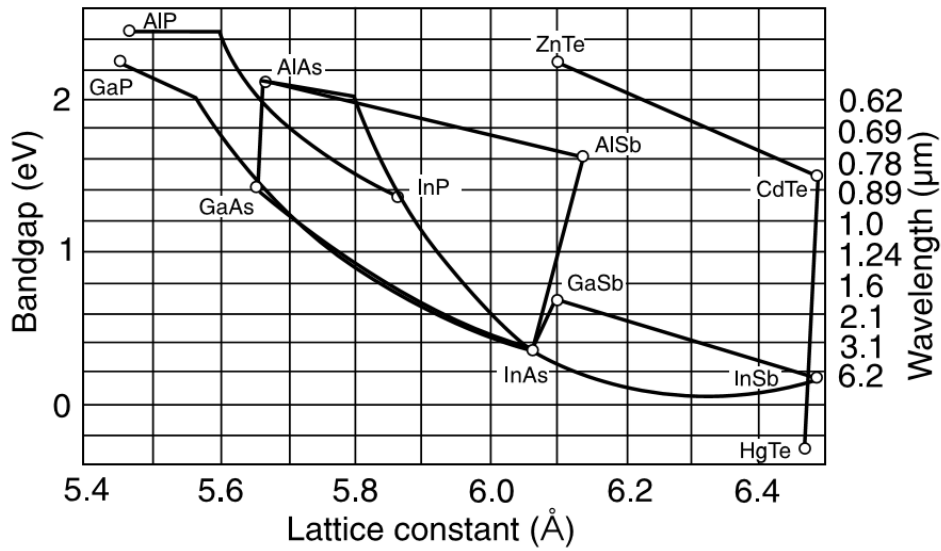


Figure 4. Modulation of band-gap and lattice constant of CdTe by incorporation of Zn or Hg instead of Cd atoms [18].

1.2.3. Phase Diagram

A pseudo phase diagram of binary CdTe-ZnTe is depicted in Figure 5 [19]. The phase temperature-composition diagram has a liquidus curve and a solidus curve. The end points correspond to the melting point of pure CdTe and ZnTe respectively. The area between the two lines corresponds to two phases which are liquid and solid solution. The concentration of Zn in CdZnTe determines the melting point of Cd-Zn-Te. The diagram indicates that the growth of CdZnTe occurs at high temperatures. From the phase diagram it can be seen that the CdZnTe forms a solid phase at all relative range of concentrations. It can also be seen from the phase diagram that there are no separate phases formed in the CdZnTe. Solidification problems, such as segregation, are encountered during the growth process at high temperature which results in non-uniformity in the stoichiometry. Moreover, the first solid to be completely melted includes more Zn atom than the value initially obtained from the average melting rate.

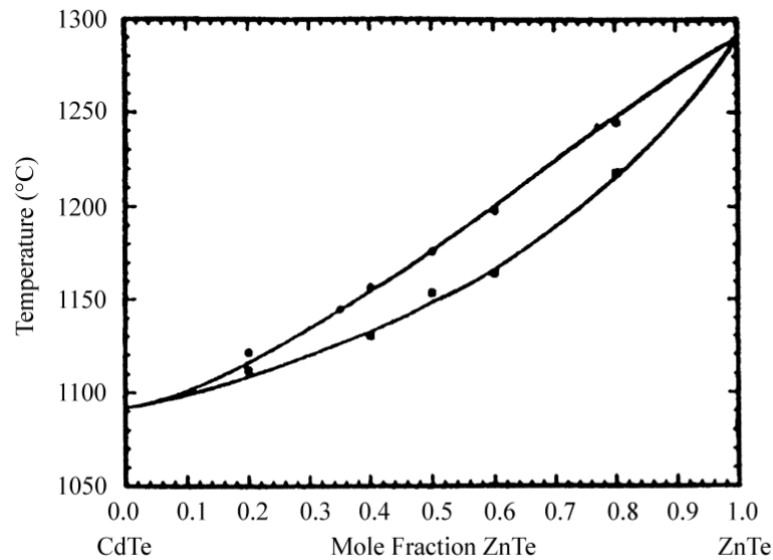


Figure 5. Temperature-mole fraction phase diagram for CdTe-ZnTe pseudo-binary [19].

1.3. Potential Applications of CdZnTe

The alloy CdZnTe which is a solid state semiconductor material that has been used in photo detectors, solar cells and light emitting diodes for a long time. In spite of that the materials has recently been used many potential scientific applications such as medical imaging, security and space science due to the desirable properties of ternary CdZnTe. Currently, there is a great demand for medical images technologies improved for cancer detection; a good example is the use of solid-state CdZnTe detectors (see Figure 6) in the detection of breast cancers by new medicine technique [20] that uses CdZnTe detectors in a mammographic configuration to ensure images with high-resolution for the breast. Another big application area, which is interest in CdZnTe technology, is security applications which are related mainly with monitoring, locating and radioactive materials such as nuclear plant monitoring and nuclear weapons surveillance to ensure environmental remediation and safety. Finally the third area where CdZnTe has been applied, is space sciences applications. By utilizing CdZnTe technology astronomers are able to study a diverse range of phenomena ranging from the study of γ -ray bursts to studying the composition of planets and asteroids.



Figure 6. The LumaGem molecular breast imaging (MBI) camera is a dedicated breast imaging system with cadmium zinc telluride (CZT) digital detectors [20].

1.4. Nanostructured Materials

At the nanoscale, the physical and chemical properties of materials are different from their bulk counterparts. In the recent decades, nanostructured materials, such as nanoparticles, quantum dots, nanowires and nanotubes, have received a great deal of caution from the commercial and scientific area because of their unique properties and potential applications [21]. There are various kinds of nanostructures with a range of dimensionality. The nanostructures are classified using dimensionality as zero-, one-, two- and three-dimensional. Figure 7 schematically shows some examples of this classification of nanostructures [22]. This section focuses on zero-, one- and two-dimensional nanostructures.

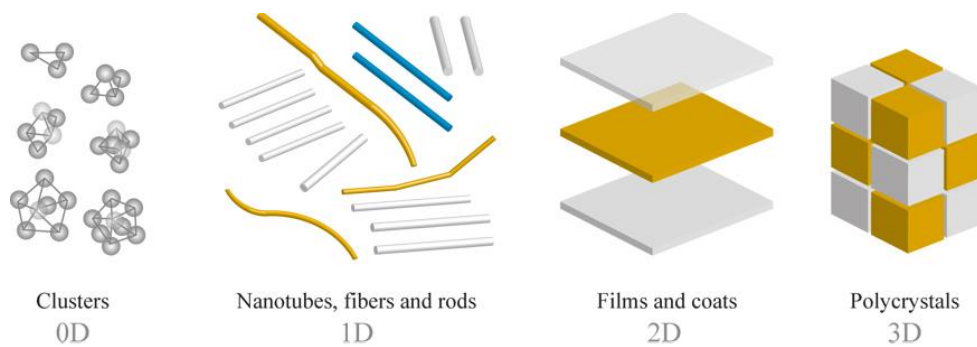


Figure 7. Types of nanocrystalline materials by the size of their structural elements: 0D clusters; 1D nanotubes, fibers and rods; 2D films and coats; 3D polycrystals [22].

1.4.1 Zero-Dimensional (0D) Nanostructure

Zero-dimensional nanostructures or quantum dots are the smallest building blocks of nanoscience and nanomaterials design [23]. Quantization occurs in all three directions at the nanoscale. This means that the conducting electrons are localized. It is an important issue to segregation phenomena which means how atoms gather together to create a nanoparticle and how the physical and chemical properties of a

nanoparticle change when its structural properties changes in terms of temperature or composition of atoms in the nanoparticle. Nanoparticles, nanocrystals, nanopores, atomic clusters and fullerenes are examples of 0D nanostructures. Nanoparticles are exist on a nanometer scale which are several hundreds of nanometers in diameter. They can possess physical and chemical properties that vary dramatically with the size [24] which makes them desirable in materials science and understanding the biological processes [25]. They are also used in many commercial products ranging from catalysts [26]–[28] to cosmetics [29].

Moreover, recent developments show that the size and charge of the nanoparticles influence their biodistribution in mice [30]. Figure 8 shows some examples of nanoparticles used in chemistry and medicine.

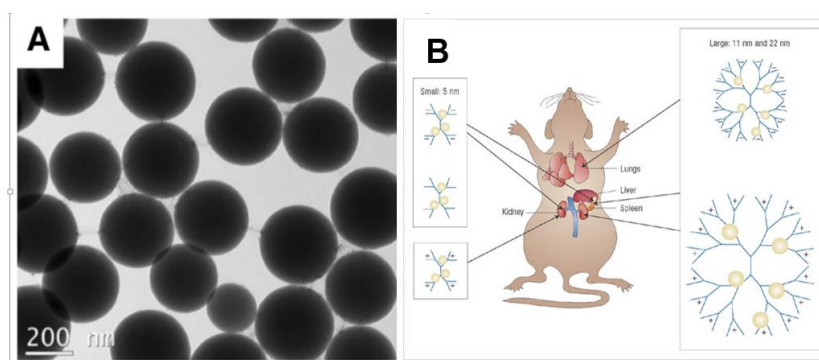


Figure 8. TEM image of Silica nanoparticles (A) [31] and Gold–dendrimer nanoparticles and their biodistribution in vivo (B) [30].

Nanoparticles including II-VI compound semiconductors, such as binary CdTe, ZnO, ZnSe, ZnS and ternary CdZnTe, HgCdTe and HgZnTe are used in many scientific applications including biological labelling [32], light-emitting devices [33], and solar cells [4]. For example, the ZnO nanoparticles are used as a sunscreen ingredient because of their transparency, which increases the usage of the sunscreen [34] for a given concentration and its effectiveness of blocking against harmful

ultraviolet-A (UVA) [35] to be harnessed to fight cancer or to help deliver drugs in a controlled manner. In addition, binary CdTe nanoparticles give rise to a better signal-to-noise ratio in confocal laser scanning microscopy (CLSM) measurements as shown in Figure 9 [36]. However, accurate physical and chemical properties of binary nanocrystals are not possible due to changes in particle size which causes problems in many applications [37], [38]. But $\text{Zn}_x\text{Cd}_{1-x}\text{Te}$ nanocrystals, which are ternary composition-tunable semiconductor nanocrystals, have been found to be synthesized successfully and their shape can be controlled by changing the stabilizer system and synthesis temperature [32]. It has also been observed that ternary ZnCdTe nanoparticles can be shape-controllable when synthesized in aqueous media by a simple route [39].

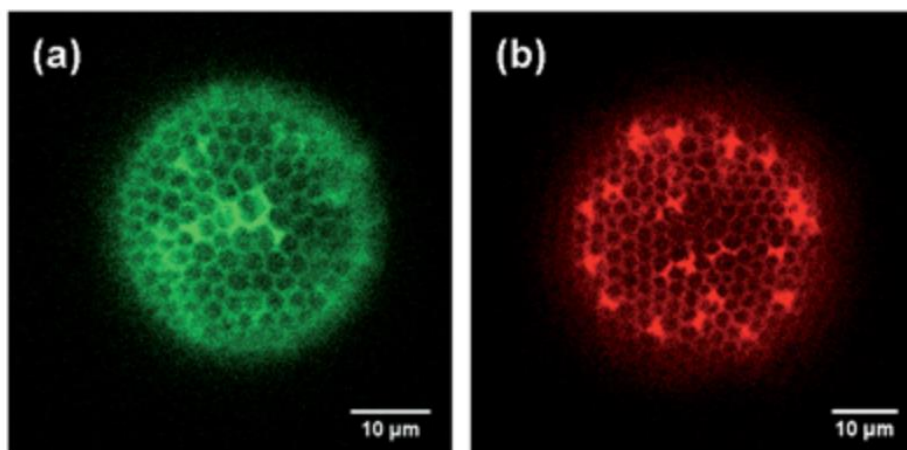


Figure 9. CLSM images of CdTe NPs using covalent coupling (a) and (b) the layer-by-layer approach [36].

1.4.2 One-Dimensional (1D) Nanostructure

1D nanostructures arise as a result of confinement of the other two dimensions perpendicular to the longitudinal direction. The width of 1D nanostructures are generally less than a hundred nanometers and their length to diameter ratio can reach up to one thousand. In the reduced dimensions and bulk properties in the other dimension the nanostructures are also called quantum wires at this nano-level. 1D nanostructures such as nanowires, nanorods, nanotubes, nanoribbons and nanobelts have been fabricated and studied in the last decade due to their importance in a large number of potential applications. They have extensively been used in nanoelectronics, nanodevices, alternative energy sources and security [40]. Figure 10 shows some examples of nanorods used in recent applications.

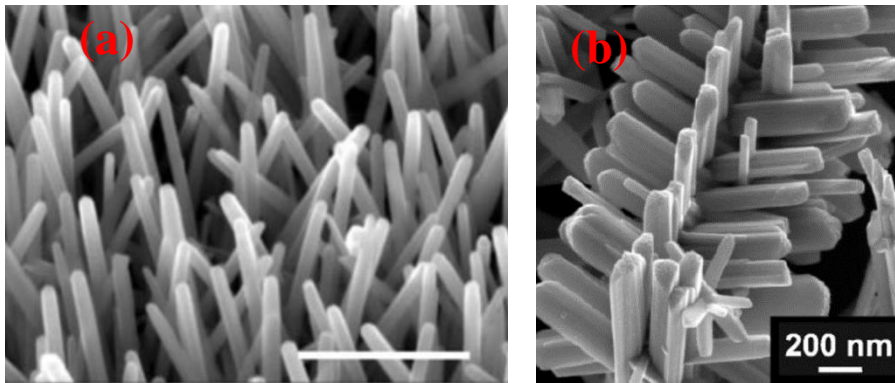


Figure 10. (a) The ZnO nanorods [41] and (b) SEM image from nanorods dispersed on a Si (001) substrate with a native oxide [42].

Numerous methods have been developed for preparing 1D nanostructures. For example, it has been shown that solar efficiency can be boosted by up to 50% by harnessing acoustic vibrations in the environment by incorporating ZnO nanorods, which can convert rock music into electrical energy, substantially improving the

efficiency of the solar cell [41]. Moreover, a new technique has been developed to create “branched” nanorods and control their shape using biomolecules which enable more powerful heat pumps and devices at the nanoscale that harvest electricity from heat in nanoelectronics devices [42]. Besides these important developments and applications, achieving 1D growth of semiconductor nanostructures is also one of the focuses of intensive research. However, 1D nanostructures based on the ternary CdZnTe are difficult to synthesize due to their higher vapour pressure [43], [44], so it remains a large challenge. The p-type $\text{Zn}_{0.3}\text{Cd}_{0.7}\text{Te}$ nanoribbons were synthesized to analyze the properties of crystal nanorod structures [6] and the X-ray detectors depending on the single-crystalline $\text{Zn}_{0.75}\text{Cd}_{0.25}\text{Te}$ nanoribbon are analyzed at the nanoscale [45]. The experiment shows that the nanoribbon offers a considerable role in accordance with lower energy consumption at the nanoscale and high efficiency for improving its applications in the X-ray detection. Recently, ZnCdTe nanorods have been produced experimentally by adding certain stabilizers thioglycolic acid (TGA) and L-cysteine (L-Cys) in the lower growth temperature with increasing the refluxing time from 30 min to 60 min. It is found that the nucleation occurs at lower growth temperature [39]. In addition, a uniform stoichiometry of $\text{Cd}_{1-x}\text{Zn}_x\text{Te}$ nanowires have been grown using an electrodeposition technique including a template process used as a gamma ray detector by stacking the nanowire array templates [46]. Figure 11 shows the CdZnTe nanowires after 45 minutes of pulse deposition. The diameter of the wires was 70 to 100 nm and the length was approximately $2\mu\text{m}$. As may be observed from the figure, the wire growth was initially straight from the nanoporous template and as the deposition time increased they started to get tangled. The tangling of nanowires can be attributed to overgrowth and to the insufficient length of the nanowires.

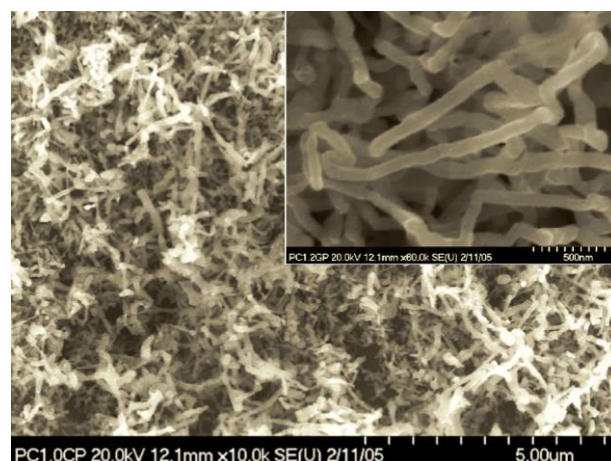


Figure 11. SEM micrograph of the CdZnTe Nanowires after 45 minutes of pulsed electrodeposition. (inset shows magnified image of the nanowires) [46]

The preparation of ternary CdZnTe nanowires could be great potential for making large area detectors. For instance, $\text{Cd}_x\text{Zn}_{1-x}\text{Te}$ nanowires have recently been synthesized via a vapor-liquid method [47] to enhancement the detection sensitivity and potential and obtained highly crystalline nanowires without any crystal defects [47].

1.4.3 Two-Dimensional (2D) Nanostructures

2D nanostructures, such as nanoplates, nanosheets, nanowalls, have two dimensions outside of the nanometric size range. The nanostructures are especially curious both for a better insight on the mechanism of nanostructure growth and for investigating and improving new applications such as sensors, photocatalysts, nanocontainers, etc. for the structures of other materials [48].

Recently, CdZnTe thin films have been taken attention at the nanoscale applications like solar cell and photovoltaic applications [49]–[51]. The reason is because the materials have appealing optical properties including optical absorption, refractive index and band-gap.

CdZnTe have been used in thin film synthesis via some techniques. For example, air-stable thin films of $\text{Cd}_{0.23}\text{Zn}_{0.77}\text{Te}$ have been used to investigate the effect of particle size on controlling the physical and optical properties [52] by the inert gas condensation (IGC) technique which provides superior thin films at the nanoscale. Moreover, the nano-crystalline CdZnTe films were grown on glass and silicon substrates at room temperature by vacuum evaporation [53].

In this thesis Chapters are organized as follows: Chapter 2 will give information on the theoretical methods which were used to simulate nanostructures. Results and discussion will be presented in Chapter 3. Chapter 4 lists the conclusions of the present work.

CHAPTER 2

METHODS OF CALCULATION

Structural, electronic, mechanical and thermal properties of nanomaterials are theoretically investigated by performing classical methods such as molecular dynamics (MD), Monte-Carlo, and quantum mechanical methods such as density functional theory (DFT). In this thesis, both MD simulations and DFT calculations have been performed.

2.1 Molecular Dynamics

Molecular dynamics (MD) is a computer simulation method that permits one to explore the macroscopic properties of a system through microscopic trajectories and thus predict the time evolution of a system of interacting particles such as atoms and molecules. The MD simulations consist of the numerical solution of Newton's equations of motion to determine the new positions of atoms or molecules in the system and to obtain forces, energies and trajectories. The equation of motion governing the behavior of the N-particle system

$$m_i \frac{d^2 \vec{r}_i}{dt^2} = \vec{F}_i(\vec{r}_1, \vec{r}_2, \dots, \vec{r}_N) = -\vec{\nabla}_i V(\vec{r}_1, \vec{r}_2, \dots, \vec{r}_N). \quad (2.1)$$

In Eq. (2.1), V represents the potential energy. r and \vec{F}_i are the position and force acting on the i 'th particle, respectively. The first one is to describe the interaction potential and initial conditions and then this equation can be solved numerically for all particles in the system until the system is equilibrated and thus determined the evolution of the system in time.

In many cases, MD is concerned with macroscopic properties of the material which is composed of configuration sets distributed in terms of statistical distribution functions, but it is not related to trajectories of individual atoms. In statistical mechanics, the physical properties of a system are calculated by an ensemble which means a collection of systems [54]. There are various thermodynamical ensembles. These ensembles are the microcanonical (NVE), canonical (NVT), grand canonical (NPT) and isobaric-isothermal (μVT).

In this study, MD has been considered in a canonical ensemble to investigate some properties of CdZnTe ternary nanostructures. The number of atoms N , the system volume V , and the temperature T of the system and the total energy remain constant throughout this ensemble. Maxwell-Boltzmann velocity distribution is used to generate particle velocities at the corresponding temperature. The temperature of the system was kept constant by a thermostat during MD simulation. There are some ways to control the temperature such as simple velocity scaling and the Berendsen thermostat, the Langevin, Andersen and Dissipative Particle Dynamics thermostats and the Nosé-Hoover thermostat in a MD simulation. Among them, the Nosé-Hoover is used as the most common thermostat [55], [56]. However, it is difficult to implement Nosé-Hoover equations of motion into MD program directly. It is necessary to integrate the Newton's equation indicated in Eq. (2.1) in small incremental times. There are some numerical techniques such as Verlet algorithm, Velocity Verlet, Leap-frog algorithm, Beeman's algorithm, Predictor-Corrector Algorithms, Nordsieck-Gear Predictor-Corrector Algorithm and Lanczos recursion algorithm to integrate the equation of motion indicated in Eq. (2.1) in MD simulation.

2.1.1 Algorithms to Integrate the Equations of Motion

2.1.1.1 Verlet Algorithm

Verlet algorithm [57], [58] is an integrator which expands the positions and velocities using Taylor series expansion to compute the new positions at the next time step using previous time step. Taylor expansion for the position

$$r(t + \delta t) = r(t) + \delta t v(t) + \frac{1}{2} \delta t^2 a(t) + \frac{1}{3!} \delta t^3 \dot{a}(t) + \dots \quad (2.2)$$

$$r(t - \delta t) = r(t) - \delta t v(t) + \frac{1}{2} \delta t^2 a(t) - \frac{1}{3!} \delta t^3 \dot{a}(t) + \dots \quad (2.3)$$

It is obvious that the linear and third order terms are cancelled when these two equations are added, so the following result yields:

$$r(t + \delta t) = 2r(t) - r(t - \delta t) + \delta t^2 a(t) + O(\delta t^4) \quad (2.4)$$

In Eq. (2.4), the error in this algorithm is in the order of the 4^{th} power. A drawback of the simple Verlet algorithm is that there is no velocity information in the evolution of position, but accelerations at time t is required. However, the kinetic energy term is known for adjusting the temperature of the heat path. The velocities can be calculated by

$$v(t) = \frac{r(t + \delta t) - r(t - \delta t)}{2\delta t} \quad (2.5)$$

It is apparent that this algorithm estimates $r(t + \delta t)$ from the current position $r(t)$ and the previous position $r(t - \delta t)$. This means that the Verlet algorithm is carried out in a two steps and thus the initial positions $r(0)$.

2.1.1.2 Predictor-Corrector Algorithms

Predictor-corrector algorithm [59] uses a neighborhood of a central path and estimates positions and velocities for next steps. It is composed of three numerical steps. In the first step, the position $r(t + \delta t)$ and velocity $v(t + \delta t)$ are estimated. In the second one is the forces at $t + \delta t$ using are evaluated the predicted position. This process is predicted by means of Taylor expansion

$$\begin{aligned} r(t + \delta t) &= r(t) + \delta t v(t) + \frac{1}{2} \delta t^2 a(t) + \frac{1}{3!} \delta t^3 b(t) + \dots \\ v(t + \delta t) &= v(t) + \delta t a(t) + \frac{1}{2} \delta t^2 b(t) + \dots \\ a(t + \delta t) &= a(t) + \delta t b(t) + \dots \\ b(t + \delta t) &= b(t) + \dots \end{aligned} \tag{2.6}$$

where b is the time derivative of the acceleration a at time t . Performing some modifications and eliminations in the Taylor expansion, the values r^p, v^p, a^p and b^p are obtained. The gradient of the potential at the predicted positions gives the force and the new predicted acceleration. The difference between the force and acceleration gives an error signal. Final step is related to correction of the positions and their derivatives.

2.1.1.3 Nordsieck-Gear Predictor-Corrector Algorithm

Nordsieck-Gear predictor corrector algorithm [60], [61] is a numerical integration technique on the basis of the Taylor expansions of the positions, velocities and some derivatives as shown in Eq. (2.7)

$$\begin{aligned} r(t + \delta t) &= r(t) + \delta t v(t) + \frac{1}{2} \delta t^2 a(t) + \frac{1}{3!} \delta t^3 q_3(t) + \dots + \frac{1}{k!} \delta t^k q_k(t) + \dots \\ v(t + \delta t) &= v(t) + \delta t a(t) + \frac{1}{2} \delta t^2 q_3(t) + \frac{1}{3!} \delta t^3 q_4(t) + \dots + \frac{1}{(k-1)!} \delta t^{k-1} q_k(t) + \dots \end{aligned}$$

$$\begin{aligned}
a(t + \delta t) &= a(t) + \delta t q_3(t) + \frac{1}{2} \delta t^2 q_4(t) + \frac{1}{3!} \delta t^3 q_5(t) + \dots + \frac{1}{(k-2)!} \Delta t^{k-2} q_k(t) + \dots \\
q_i(t + \delta t) &= q_i(t) + \delta t q_{i+1}(t) + \frac{1}{2} \delta t^2 q_{i+2}(t) + \frac{1}{3!} \delta t^3 q_{i+3}(t) + \dots + \frac{1}{(k-i)!} \Delta t^{k-i} q_k(t) + \dots
\end{aligned}
\tag{2.7}$$

where $r^{(0)}$ is the position at time $t + \delta t$, $r^{(k)}$ is its derivatives with $r^{(0)} = r, r^{(1)} = \Delta t v(t), r^{(2)} = \Delta t^2 a(t), \dots, r^{(k)} = \frac{q}{k!} \Delta t^k(t)$ at time t , $q_k(t) = \frac{\partial^k}{\partial t^k} r(t)$ and $i = 3, 4, \dots$. The derivatives $r^{(0)}, r^{(1)}, r^{(2)}, \dots$ are predicted at time $t + \delta t$ using Taylor expansion at time t . Then, the predicted positions and their derivatives are corrected to calculate correct accelerations. The difference between the predicted and evaluated accelerations yields a measurement for the predictor step error utilized to develop the predicted values in the corrector step.

In this study, the seventh order predictor–corrector method is used to solve the equations of motion for many-body potential energy function (PEF).

2.1.1.4 Lanczos Recursion Algorithm

The Lanczos algorithm technique is related to transformation of a large full matrix H_{ij} into a tridiagonal complex symmetric matrix of smaller dimension [62], [63]. Firstly, the algorithm specifies a beginning vector $v_i^{(0)}$ and defines $v_i^{(-1)}$ as zero. It is taken into consideration the recursion relation

$$b_{n+1} v_i^{(n+1)} = \sum_j H_{ij} v_j^{(n)} - a_n v_i^{(n)} - b_n v_i^{(n-1)}. \tag{2.8}$$

Using the orthonormality of the Lanczos vectors,

$$\sum_i v_i^{(n)*} v_i^{(m)} = \delta_{nm}, \tag{2.9}$$

and getting the inner product of Eq. (2.8) with $v_i^{(n+1)}$, $v_i^{(n)}$ and $v_i^{(m)}$, separately, leads to

$$b_n = \sum_{ij} v_i^{(n-1)*} H_{ij} v_j^{(n)} \quad (2.10)$$

$$a_n = \sum_{ij} v_i^{(n)*} H_{ij} v_j^{(n)} \quad (2.11)$$

$$0 = \sum_{ij} v_i^{(m)*} H_{ij} v_j^{(n)} \text{ for } |m - n| > 1 \quad (2.12)$$

If matrix H_{ij} is taken a real and symmetric, then the Lanczos basis is to be real and also

$$b_n = \sum_{ij} v_i^{(n)} H_{ij} v_j^{(n-1)} \quad (2.13)$$

Thus the matrix in the Eq. (2.13) has two inputs including diagonal (a_n) and first sub- and super- diagonal (b_n). The other inputs are zero. This tridiagonal complex symmetric matrix representation \tilde{H}_{ij} is used for many useful purposes.

In addition, Lanczos recursion algorithm has been basic of the mathematical fragments of the Bond Order Potentials (BOPs). It is used to calculate Green functions which give the electronic structures for a tight-binding model [64], [65]. Therefore, it presents an important step toward quantum-based interatomic potentials in molecular dynamics to get the eigenvalues of very large matrices and to calculate other molecular properties.

In this study, Lanczos recursion algorithm is used to solve the equations of motion for Bond Order Potential (BOP).

2.1.2 Potential Energy Functions

The interactions among the particles, atoms or molecules are described by potential energy function (PEF) which is a parametric function. There are many potential functions which describe interparticle interactions. Empirical potentials (Bond Order Potential [66], Brenner potential [67]), pair and many-body potentials (Lennard-Jones potential [68], Tersoff potential [69]), semi-empirical potentials are among the examples.

In this thesis, many-body PEF which is defined by Lennard-Jones and Axilrod-Teller and bond order potential (BOP) have been used in the MD simulations.

2.1.2.1 Lennard-Jones and Axilrod-Teller PEF

In MD calculations, the total energy of a system is expressed by means of a many-body PEF which is a linear combination of two- and three-body interactions. The explicit form of the total interaction energy function for N particles is given by

$$\Phi = \phi_1 + \phi_2 \quad (2.14)$$

where

$$\phi_1 = \sum_{i < j}^N U_2(r_{ij}) \quad (2.15)$$

and

$$\phi_2 = \sum_{i < j < k}^N U_3(r_{ij}, r_{ik}, r_{jk}) \quad (2.16)$$

In Eq. (2.15) U_2 expresses the two-body pair interaction

$$U_2(r_{ij}) = U_{ij} = \varepsilon_0 \left[\left(\frac{r_0}{r_{ij}} \right)^{12} - 2 \left(\frac{r_0}{r_{ij}} \right)^6 \right] \quad (2.17)$$

and the energies U_3 express three-body interaction

$$U_3(r_{ij}, r_{ik}, r_{jk}) = W_{ijk} = Z \frac{(1 + 3 \cos \theta_i \cos \theta_j \cos \theta_k)}{(r_{ij}, r_{ik}, r_{jk})^3} \quad (2.18)$$

In Eq. (2.18) U_2 and U_3 represent the two-body interactions defined by the Lennard–Jones function [70] and the three-body interactions defined by the Axilrod-Teller triple-dipole function [71], respectively. These parameters required for the calculations of two-body interactions, ε_0 and r_0 , are binding energy (dissociation energy) and the equilibrium interatomic distance for dimer molecules, respectively. Z in U_3 is three-body (intensity) parameter. $\theta_i, \theta_j, \theta_k$ and r_{ij}, r_{ik}, r_{jk} are the angles and interatomic distance, respectively (see Figure 12). In the literature, a analogue PEF with different parameters has been utilized to study the properties of AlTiNi clusters [72], [73] and the structural properties of silicene nanoribbons and Si nanorods [74], [75].

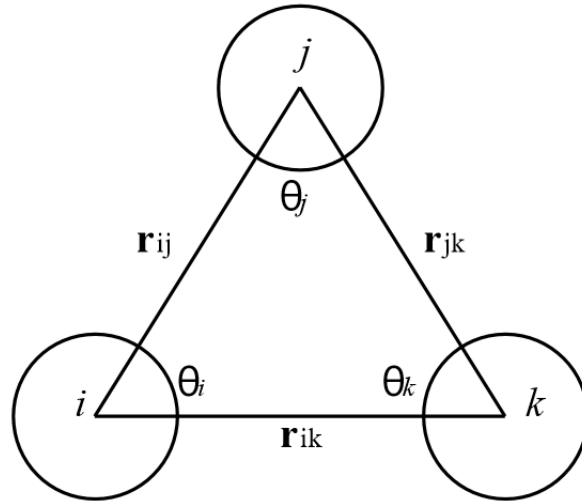


Figure 12. Triplet configuration of atoms i , j and k in Eq. (2.18) [76].

Making use of the available quantum mechanical calculation results and experimental data involving bulk cohesive energies, dimer dissociation energy, atomic distances for dimers and trimers of Zn, Cd, and Te (see Table 2), we have obtained highly accurate values for the needed parameters, (ϵ_0, r_0, Z) of the PEF for Cd-Zn-Te system. The parametrization procedure is only a numerical search to obtain the predetermined geometry and energy of the system considered. First one is to fix two- and three-body parameters by utilizing the experimental and theoretical results and then acquire a structure having a good geometry and energy representing predetermined ones. This processing returned for the parameters up to obtaining the possible ideal outcome. The parametrization procedure of the PEF is presented in Ref. [77] for Zn, Cd and Zn-Cd which took into account only the two-body term. In addition to this, we have determined the potential parameters for Te, Zn-Te, Cd-Te and $\text{Zn}_x\text{Cd}_{1-x}\text{Te}$ systems to research some properties including structural and energetics of ZnCdTe ternary system. Thus, the new ZnCdTe atomistic potential effectively captures property of multiple Cd, Zn, Te, CdZn, CdTe, ZnTe, and $\text{Zn}_x\text{Cd}_{1-x}\text{Te}$.

Table 2. Potential parameters used in the calculations.

Interaction	$\epsilon_0(eV)$	$r_0(\text{\AA})$	Interaction	$Z(eV \text{\AA}^9)$	Interaction	$Z(eV \text{\AA}^9)$
Zn-Zn	0.070 ^a	3.000 ^a	ZnZnZn	-490.0 ^a	CdCdCd	-1750.0 ^a
Zn-Cd	0.015 ^a	3.350 ^a	ZnZnCd	-400.0 ^a	CdCdTe	2870.0
Zn-Te	0.900 ^c	2.366 ^c	ZnCdCd	-500.0 ^a	CdTeTe	2925.0
Cd-Cd	0.050 ^a	3.500 ^a	ZnCdTe	2850.0	TeTeTe	3275.0
Cd-Te	1.150	2.570 ^b	ZnZnTe	2970.0		
Te-Te	1.200	2.557 ^d	ZnZnTe	2950.0		

^a[77], ^b[78], ^c[79], ^d[80].

2.1.2.1 Analytical Bond Order Potential (BOP)

Bond order potential (BOP) is analytically derived from quantum mechanical theories including the tight-binding model to describe atomic bonding [81]–[84]. For this purpose, a general analytic expression has been reproduced using tight-binding theory for the BOP by Pettifor and his collaborators [82], [83], [85], [86]. In the construction of the BOP [66], the total energy of a system including N atoms $i = (1, 2, \dots, N)$ is defined as

$$E = \frac{1}{2} \sum_{i=1}^N \sum_{j=i_1}^{i_N} \phi_{ij}(r_{ij}) - \sum_{i=1}^N \sum_{j=i_1}^{i_N} \beta_{\sigma,ij}(r_{ij}) \cdot \Theta_{\sigma,ij} - \sum_{i=1}^N \sum_{j=i_1}^{i_N} \beta_{\pi,ij}(r_{ij}) \cdot \Theta_{\pi,ij}, \quad (2.19)$$

where $\phi_{ij}(r_{ij})$ (repulsive energy), $\beta_{\sigma,ij}(r_{ij})$, and $\beta_{\pi,ij}(r_{ij})$ (bond integrals) are pair functions, and $\Theta_{\sigma,ij}$ and $\Theta_{\pi,ij}$ are many-body functions which represent σ and π bond orders which are functions of the local environment of atoms i and j , respectively. Neighbors of atom i is represented as the list $j = i_1, i_2, \dots, i_N$. The details of the BOP are given in Ref. [87].

In this study, MD simulations of spherical and cubic nanoparticles and nanowires have also been studied via LAMMPS (large-scale atomic/molecular massively parallel simulator) [88] using a recently developed CdZnTe analytical BOP [87]. The CdZnTe BOP represents the cluster and bulk properties of multiple Zn, CdZn, ZnTe, CdTe and Cd-Zn-Te structures compared with experiments and DFT data so far. The BOP with present parameters generate results consistent with experimental data for such properties as atomic energies and volumes, elastic constants, and melting temperature containing clusters, bulk lattices, point defects, and surfaces. Total of 82 parameters such as one point-dependent, two and three body are determined for BOP of the CdZnTe by D. K. Ward and his collaboration [87]. The parameterization and physics of the BOP is given in detail in Refs. [66], [87].

2.1.3 Periodic Boundary Conditions

Periodic boundary conditions (PBC) are used in MD simulations to approximate a large system by using a small part. The system with PBC is constructed by copy a particle and its position from one cell to next as indicated in Figure 13. This copy creates a lattice in 1D, or 2D or 3D of space. When applying PBC, the number of particles is also conserved in the system. Consequently, the particles leave the cell from one side and then an identical copy reenters the cell through the opposite side. Particles lying within a r_{cut} radius (the radius is usually implemented when the force between two atoms is calculated.) distance (see Figure 13) of a boundary interact with particles in a neighboring cell. The neighboring cell represents a copy of one of the particles in the simulation cell inasmuch as it is within the radius which is always chosen so that an atom can interact with only one image of any given particle in the simulation cell.

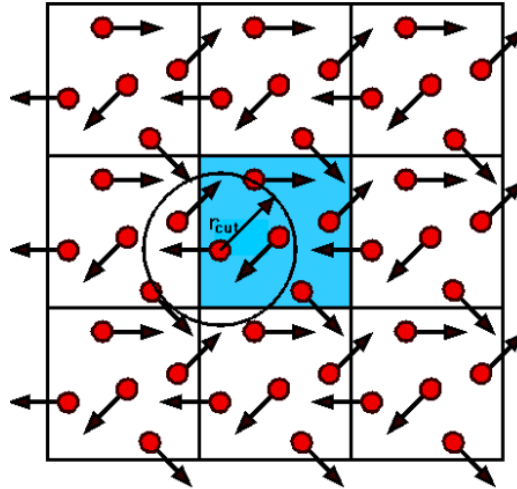


Figure 13. Periodic boundary conditions in two dimensions [89].

2.2 Density Functional Theory

The density functional theory (DFT) is presently the most successful approach to solve exactly the electronic Schrödinger equation for the electronic wave function of a many-body system. Feasibility of DFT is varied from atoms, molecules and solids to nuclei. DFT estimates a variety of electronic, optical and magnetic properties such as the vibrational frequencies, lowest total energies, density of state, UV-spectra etc. of atoms, molecules or larger systems. The main aim is to solve time independent Schrödinger equation for the electron density and obtain the molecular properties of any molecular system. For this purpose, several approximations are used to make DFT practically possible.

2.2.1 Born-Oppenheimer Approximation

The time-independent Schrödinger equation (non-relativistic) is defined as

$$\hat{H}\Psi_i(\vec{x}_1, \vec{x}_2, \dots, \vec{x}_N, \vec{R}_1, \vec{R}_2, \dots, \vec{R}_M) = E_i \Psi_i(\vec{x}_1, \vec{x}_2, \dots, \vec{x}_N, \vec{R}_1, \vec{R}_2, \dots, \vec{R}_M), \quad (2.20)$$

In Eq. (2.20), \hat{H} represents the Hamiltonian related to a system with M nuclei and N electrons:

$$\hat{H} = -\frac{1}{2} \sum_{i=1}^N \nabla_i^2 - \frac{1}{2} \sum_{A=1}^M \frac{1}{M_A} \nabla_A^2 - \sum_{i=1}^N \sum_{A=1}^M \frac{Z_A}{r_{iA}} + \sum_{i=1}^N \sum_{j>1}^N \frac{1}{r_{ij}} + \sum_{A=1}^M \sum_{B>A}^M \frac{Z_A Z_B}{R_{AB}} \quad (2.21)$$

In Eq. (2.21), r_{iA} refers to the distance between electron and the nucleus. R_{AB} and r_{ij} the distance between nuclei and between electrons, respectively. The terms appearing in Eq. (2.21) represent the kinetic energy of the electron and nucleus, attractive potential energy of the electron-nucleus and repulsive potential energy of electron-electron and nucleus-nucleus interactions [90], [91]. Furthermore, atomic units have been used.

Due to their masses, the nuclei move much more slowly than the electrons. Born and Oppenheimer [92] considered the electrons as moving in the field of the fixed nuclei, in which a molecule has zero kinetic energy and constant potential energy. The nuclei upon each electron can be written as an external potential:

$$V_{ext}(\vec{r}) = - \sum_{A=1}^M \frac{Z_A}{r_{iA}}. \quad (2.22)$$

Therefore, the Hamiltonian diminishes to

$$\hat{H}_e = -\frac{1}{2} \sum_{i=1}^N \nabla_i^2 - \sum_{i=1}^N V_{ext}(\vec{r}_i) + \sum_{i=1}^N \sum_{j>1}^N \frac{1}{r_{ij}} \quad (2.23)$$

electronic time-independent Schrödinger equation reads

$$\hat{H}_e \Psi_e(\vec{r}_1, \vec{r}_2, \dots, \vec{r}_N) = E_e \Psi_e(\vec{r}_1, \vec{r}_2, \dots, \vec{r}_N) \quad (2.24)$$

While significantly simplified, this is still a very complicated equation due to the electron-electron interaction. This problem becomes intractable even for small systems with a few atoms.

2.2.2 Hartree -Fock Approximation

This method employs N electrons as occupying N different orbitals each of which can accommodate one electron. The Hartree product of the individual orbitals which is the simplest application to a many-body wave function of an N -electron system can be defined as,

$$\Phi(\vec{r}_1, \vec{r}_2, \dots, \vec{r}_N) = \phi_1(\vec{r}_1) \phi_2(\vec{r}_2) \dots \phi_N(\vec{r}_N) \quad (2.25)$$

However, the Hartree product does not satisfy the Pauli-exclusion principle on the antisymmetry property. The antisymmetry conditions are satisfied by using the Hartree-Fock method approximation [93], [94]. This approximation says that the best set of an atom with only one-electron wave functions in the form of Slater determinant represent the ground state.

$$\Phi(\vec{r}_1, \vec{r}_2, \dots, \vec{r}_N) = \frac{1}{\sqrt{N!}} \begin{vmatrix} \phi_1(\vec{r}_1) & \phi_2(\vec{r}_1) & \dots & \phi_N(\vec{r}_1) \\ \phi_1(\vec{r}_2) & \phi_2(\vec{r}_2) & \dots & \phi_N(\vec{r}_2) \\ \vdots & \vdots & \ddots & \vdots \\ \phi_1(\vec{r}_N) & \phi_2(\vec{r}_N) & \dots & \phi_N(\vec{r}_N) \end{vmatrix}. \quad (2.26)$$

It is the Slater determinant which satisfies antisymmetry condition. It disappears if the set $\{\phi_i\}$ is linearly dependent. Especially, this condition occurs when it is concerned with two (or more) spin orbitals which are the same. Namely, two electrons cannot occupy the same quantum state. On the other hand, the Slater determinant which is an antisymmetric tensor is appraised by means of the Laplace expansion.

The Slater determinant includes exchange term, however, Hartree-Fock method neglects correlations in the motion between two electrons with anti-parallel spins. Therefore, an exact solution of the Schrödinger equation is impossible using Hartree-Fock equations, but the solution is possible by resorting to a self-consistent method.

2.2.3 The Electron Density

The electron density is used that the ground-state total energy is the functional of the ground-state electron density in DFT calculations. It is described as the integral over the spin coordinates of all electrons and whole but one of the spatial variables ($\vec{x} = \vec{r}, s$)

$$\rho(\vec{r}) = N \int \dots \int |\psi(\vec{x}_1, \vec{x}_2, \dots, \vec{x}_N)|^2 ds_1 d\vec{x}_2 \dots d\vec{x}_N \quad (2.27)$$

$\rho(\vec{r})$ determines the probability of existing any of the N electrons inside of a differential volume element $d\vec{r}$. The advantages of the density are obvious. The many-body wave function is dependent on 3 spatial variables, but $\rho(\vec{r})$ is a positive function integrating to the total number of electrons, in which it is just the three spatial variables, which disappears at infinity for localized systems.

$$\rho(\vec{r} \rightarrow \infty) \rightarrow 0, \quad \int \rho(\vec{r}) d\vec{r} = N. \quad (2.28)$$

2.2.4 The Hohenberg–Kohn Theorem

In 1960s, a method for obtaining the properties of any-electron systems was formulated by Hohenberg and Kohn [95]. In this method the electron density is directly used the basic quantity. In 1964, Hohenberg and Kohn indicated that the external potential could be written as an explicit functional of the density. The first Hohenberg-Kohn theorem indicates that the density distinctively define all the properties of any system by the Hamiltonian operator. As a result, the ground-state total energy as a functional of the electron density is defined as

$$E[\rho] = T[\rho] + V_{ne}[\rho] + V_{ee}[\rho] = \int \rho(\vec{r}) v(\vec{r}) d\vec{r} + F_{HK}[\rho], \quad (2.29)$$

with the Hohenberg-Kohn functional,

$$F_{HK}[\rho] = T[\rho] + V_{ee}[\rho], \quad (2.30)$$

which includes the of the kinetic energy $T[\rho]$ and the potential energy $V_{ee}[\rho]$ of the electron-electron interaction. The functional for the interaction is written as

$$V_{ee}[\rho] = \frac{1}{2} \iint \frac{\rho(\vec{r})\rho(\vec{r}')}{|\vec{r} - \vec{r}'|} d\vec{r} d\vec{r}' + E_{ncl} = J[\rho] + E_{ncl}. \quad (2.31)$$

$$V_{ee}[\rho] = \frac{1}{2} \iint \frac{\rho(\vec{r})\rho(\vec{r}')}{|\vec{r} - \vec{r}'|} d\vec{r} d\vec{r}' + E_{ncl} = J[\rho] + E_{ncl}. \quad (2.32)$$

In Eq. (2.32), E_{ncl} presents the non-classical contribution to the electron-electron interaction which includes self-interaction, exchange and Coulomb corrections. The obvious formalism of the functional $T[\rho]$ and E_{ncl} is the main difficulty in DFT due to the unknown the functional.

The second theorem of Hohenberg–Kohn states that the functional $F_{HK}[\rho]$ provides an electron density which can be obtained from the total energy $E[\rho]$ of the ground state. This theorem is based on the variational principle,

$$E_0 \leq E[\tilde{\rho}] = T[\tilde{\rho}] + V_{ne}[\tilde{\rho}] + V_{ee}[\tilde{\rho}] \quad (2.33)$$

which supplies the necessary boundary conditions for any trial density $\tilde{\rho}(\vec{r})$ such as $\tilde{\rho}(\vec{r}) \geq 0$ and $\int \rho(\vec{r}) d\vec{r} = N$.

2.2.5 The Kohn-Sham Theorem

In 1965, Kohn and Sham [96] introduced a method based on a functional of the electron density in terms of the Hohenberg-Kohn theorem. In this method, the density of a system of interacting particles can be defined as the density under the impact of the effective external potential in which the non-interacting particles move, which is called the Kohn-Sham potential. This potential is composed of the external potential and the Hartree potential and the exchange-correlation (XC) potential is given as:

$$E_{XC}[\rho] \equiv (T[\rho] - T_S[\rho]) + (E_{ee}[\rho] - J[\rho]) \quad (2.34)$$

which contains all the remaining contributions. The XC energy E_{XC} is the functional including everything that is unknown.

In practice approximations for the XC energy and its potential must be developed so that the electron-electron term is defined in accordance with the single-particle density. The correction to this term is named the correlation energy because the electron-electron term is expressed as the two-particle density and not according to the single-particle density. Exchange energy arises from the Pauli Exclusion Principle and the correlation energy comes from the repulsion between electrons. The explicit form of the ground- state total energy in terms of functional of density is:

$$\begin{aligned}
E[\rho] &= T_s[\rho] + \frac{1}{2} \iint \frac{\rho(\vec{r}_1)\rho(\vec{r}_2)}{r_{12}} d\vec{r}_1 d\vec{r}_2 + E_{xc}[\rho] + \int V_{Ne}\rho(\vec{r})d\vec{r} \\
&= -\frac{1}{2} \sum_i^N \langle \psi_i | \nabla^2 | \psi_i \rangle + \frac{1}{2} \sum_i^N \sum_j^N \iint |\psi_i(\vec{r}_1)|^2 \frac{1}{r_{12}} |\psi_j(\vec{r}_2)|^2 d\vec{r}_1 d\vec{r}_2 + E_{xc}[\rho] \\
&\quad - \sum_i^N \int \sum_A^M \frac{Z_A}{r_{1A}} |\psi_i(\vec{r}_1)|^2 d\vec{r}_1.
\end{aligned} \tag{2.35}$$

2.2.6 Exchange-Correlation Functionals

It is important to know the exchange-correlation (XC) energy functional for a practical way to actually use the Kohn-Sham equations. On the other hand, the exact expression of the XC is not known in a closed mathematical form so that there are many approximating functionals which is developed and used with varying levels of complexity. The functionals have been categorized by “Jacob’s ladder” (see Figure 14) [97] and assigned to different rungs of ladder in terms of the complexity of their ingredients. The accuracy and cost of computation increase as one goes up the ladder.

In addition, functionals including non-empirical or semi-empirical can be classified from density functional approximations to the XC energy in this ladder.

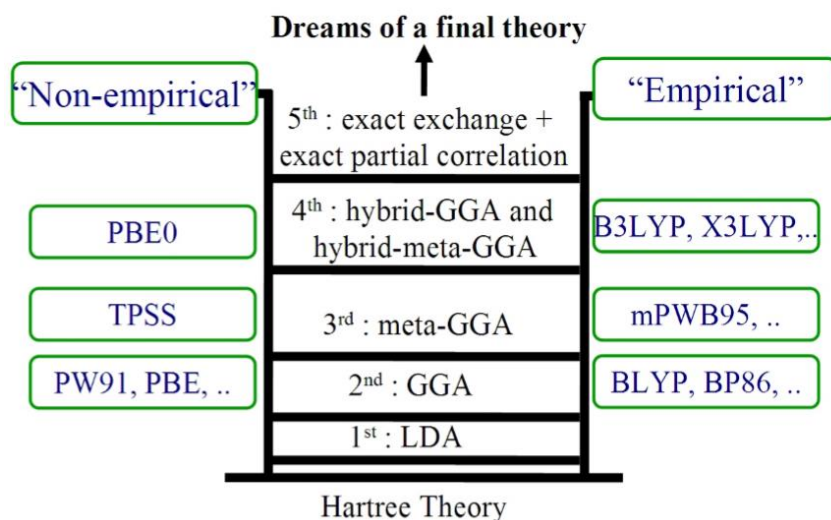


Figure 14: Schematic diagram of exchange-correlation functionals [97].

It is important to know the appropriate correlation functional for system studied to obtain good performance from DFT calculations. In this section, the XC functionals of this ladder shown in the diagram are given as a brief introduction to the most common types the functionals in extensive use.

In the ladder, each rung represents a different level from lower to higher rungs. The lowest rung is local density approximation (LDA) [98], in which the XC energy is only dependent on the density at a point and that of the uniform electron gas of that density. Some of selected popular XC functionals of LDA are the Perdew-Zunger (PZ) [99], Perdew-Wang (PW) [100] and Vosko-Wilk-Nusair (VWN) [101]. In generalized gradient approximations (GGAs), on the next rung, the XC energy is taken to be both the density and its gradient at each point. GGAs are more accurate than LDA, but LDA is better for van der Waals (vdW) interaction. Moreover, GGAs decrease the bond dissociation energy error and improve transition-state barriers in general.

The most popular GGAs include Perdew-Burke-Ernzerhof (PBE) [102], Perdew-Wang 91 (PW91) [103] Lee-Yang-Parr (LYP) [104], and Perdew86 (P86) [105]. GGAs are necessary to reasonably describe hydrogen bonds (HBs) [106]–[108] at all times.

In meta-GGAs, the XC energy depends on the density, its gradient and the KS kinetic energy density. Meta-GGAs are especially used for calculations on surfaces since they give better properties like surface energies than GGAs. Besides, the TPSS [109] functional belonging to meta- GGAs has been found to be more reasonable than LDAs and GGAs [110]–[112] in gas phase.

The Hybrid-GGA functional is a mixture some XC functional with a GGA. It also gives better results for band gaps and reaction barrier heights than LDA and GGAs.

Description of metals with LDA are worse than that of GGAs. The aim of meta-GGAs is to produce a highly accurate functional, without cost. Some of the hybrid methods are the B3LYP, [113], B3P86 [105], [113], B3PW91 [103], [114], B1LYP [115], etc. In this thesis, the B3LYP has been used as the functional. The exchange term of the functional uses components of the first- and second-order density matrices [116]. The correlation term is denoted by the Vosko, Wilk, and Nusair (VWN3) local correlation functional [101] together with the correlation term of Lee, Yang, and Parr [104].

The fourth functional is the hybrid meta-GGA. This functional is composed of meta-GGA and hybrid functionals with appropriate parameters fitted to some molecular databases such as PW6B95 [117] which includes 6-parameter functional based on PerdewWang’91 exchange and Becke’95 correlation and MPWB1K [118].

2.2.7 Basis Sets

Basis functions are employed in all DFT implementations as a means of converting the integro-differential Kohn-Sham (KS) equations to a linear algebra formalism. This is achieved by means of expanding the KS orbitals in a suitable set of basis functions like exponential, polynomial Gaussian, Slater type orbitals, and so on. Among these functions, Slater and Gaussian functions are commonly used as the basis functions in molecular calculations. A Slater type orbital (STO) for an s-type atomic orbital (AO) has the form

$$R(r)_{STO} = Ne^{-\alpha r}, \quad (2.36)$$

where r is the radial distance from the nucleus, N is the normalization constant, and α is the orbital exponent. A Gaussian type orbital (GTO) for an s-type AO with the same orbital exponent has the form

$$R(r)_{GTO} = Ne^{-\alpha r^2}. \quad (2.37)$$

STOs are very suitable for expanding molecular orbitals because they have the correct shape, however, GTOs are preferred in practice because they allow for efficient computation of molecular integrals. Therefore, in practice STOs are used as a linear combination of enough GTOs.

In this thesis, CEP-121G is used as atomic orbitals to calculate the electron orbitals. In this basis set the dependence of spin-orbit effects was averaged out and reproduced from an optimizing procedure based on an energy-overlap functional and from a numerical Dirac-Fock atomic wave functions using shape-consistent valence pseudo-orbitals. CEP basis sets have been used especially in quantum chemistry to investigate the structure with heavy elements [119], [120] and also the equilibrium geometry and the spectroscopic properties of some small molecules [119]–[121].

CHAPTER 3

RESULTS AND DISCUSSION

3.1 Structural Properties of $\text{Zn}_x\text{Cd}_{1-x}\text{Te}$ ($x=0.25, 0.50$ and 0.75) Ternary Nanorods: Molecular Dynamics Simulations

3.1.1 Introduction

The structural properties of $\text{Zn}_x\text{Cd}_{1-x}\text{Te}$ ternary nanorods for ($x= 0.25, 0.50$ and 0.75) have been investigated by carrying out MD simulations at various temperatures. An atomistic many-body PEF has been used to represent the interparticle interactions. It has been found that the structural properties of $\text{Zn}_x\text{Cd}_{1-x}\text{Te}$ ternary nanorods show a dependence on stoichiometry and temperature.

3.1.2 Modelling and Calculation Procedure

In this study, a Lennard-Jones and Axilrod-Teller PEF is used. Maxwell-Boltzmann velocity distribution is used to generate particle velocities. Nordsieck-Gear algorithm was utilized to solve the equation of motion. The cut-off radius of 7.0 \AA was used for maximum interaction range. Thermal equilibrium was controlled by choosing a simple velocity scaling thermostat and the canonical ensemble (NVT, constant number of particles, volume, and temperature). Periodic boundary conditions were imposed along the rod axis (z-axis in our case). The temperature ranges are as the follows: 1 K and 1500 K for $\text{Zn}_{0.25}\text{Cd}_{0.75}\text{Te}$, 1 K and 1800 K for $\text{Zn}_{0.50}\text{Cd}_{0.50}\text{Te}$, and 1 K and 2100 K for $\text{Zn}_{0.75}\text{Cd}_{0.25}\text{Te}$. The reason for the different temperature ranges for each model is due to different composition (stoichiometry) of each model. The systems were relaxed until they reach equilibrium energetically. A sample graph showing the energetic relaxation

for the model $\text{Zn}_{0.50}\text{Cd}_{0.50}\text{Te}$ at 600 K is given in Figure 15. Depending on the composition and temperature the range of relaxation time varies as follows: Initially, $\text{Zn}_{0.25}\text{Cd}_{0.75}\text{Te}$, $\text{Zn}_{0.50}\text{Cd}_{0.50}\text{Te}$ and $\text{Zn}_{0.75}\text{Cd}_{0.25}\text{Te}$ nanorods were equilibrated in 45000, 30000 and 40000 time steps at 1K respectively. After that, time steps for $\text{Zn}_{0.25}\text{Cd}_{0.75}\text{Te}$, $\text{Zn}_{0.50}\text{Cd}_{0.50}\text{Te}$ and $\text{Zn}_{0.75}\text{Cd}_{0.25}\text{Te}$ are obtained by time averaging 300.000, 160.000 and 250.000 between 300K and 2100K separately. $\text{Zn}_x\text{Cd}_{1-x}\text{Te}$ ternary nanorods with a lattice constant of 5.708 Å have a cubic crystal structure. The initial cell sizes (x, y, z) of three ZnCdTe nanorod models considered in the present study are 10.6, 10.6 and 33.5 Å respectively. Cross section and side views of the initial structures of the three ZnCdTe nanorod models are shown in Figure 16.

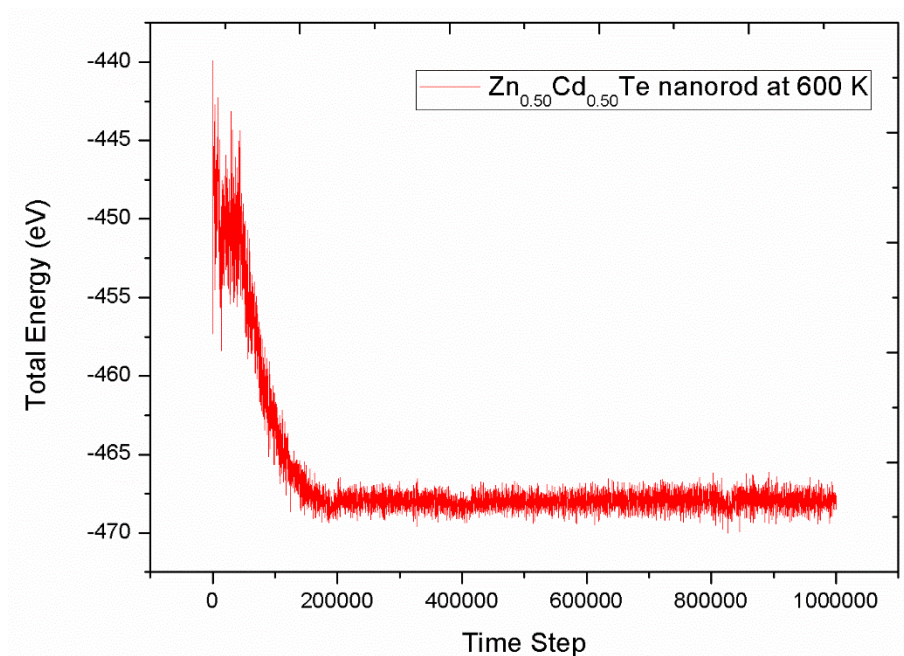


Figure 15. The energetic relaxation plot for $\text{Zn}_{0.50}\text{Cd}_{0.50}\text{Te}$ nanorod at 600 K.

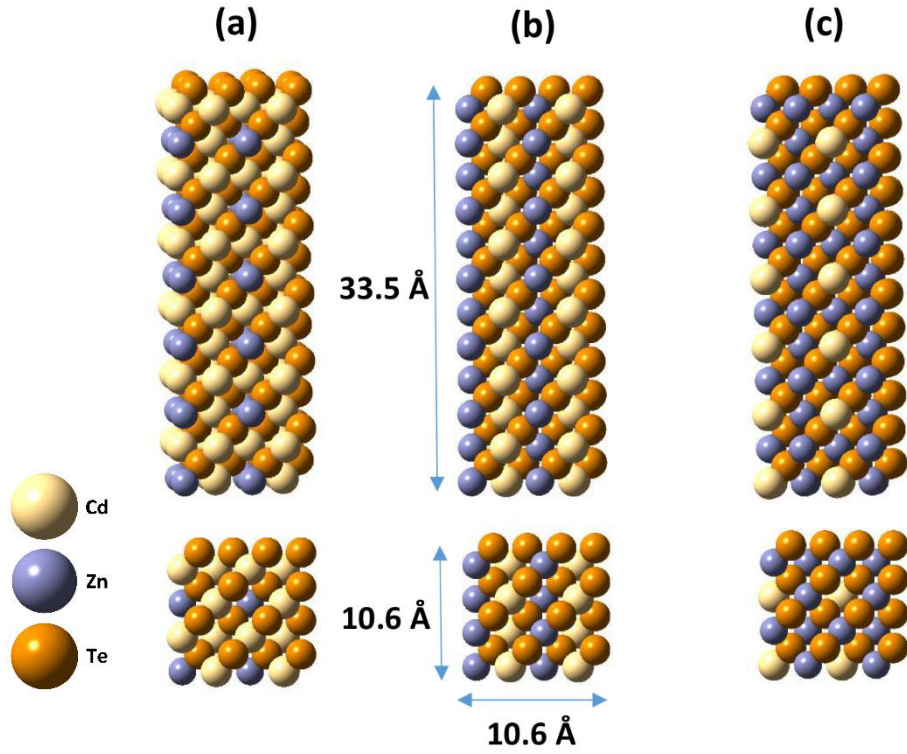


Figure 16. Side and cross section views of the generated structures of (a) $\text{Zn}_{0.25}\text{Cd}_{0.75}\text{Te}$ (b) $\text{Zn}_{0.50}\text{Cd}_{0.50}\text{Te}$ (c) $\text{Zn}_{0.75}\text{Cd}_{0.25}\text{Te}$ nanorod models.

3.1.3 Results and Discussions

The method of calculation described above has been applied to compute structural properties of $\text{Zn}_x\text{Cd}_{1-x}\text{Te}$ ternary alloys nanorods with Zn concentrations for $x=0.25$, 0.50 and 0.75.

Figure 17 shows the number of Zn atoms variation with temperature for ZnCdTe nanorod models. As it can be seen from Figure 17, Zn atoms start to break up after about 300 K and disappear completely all the Zn atoms from the nanorods after certain temperature depending on the Zn concentration in the nanorod. In addition, the number of Zn, Cd and Te atoms remaining in terms of different temperatures for the three

ZnCdTe nanorod models is given in Table 3. It is apparent that there is no missing atom in all the models at 1K.

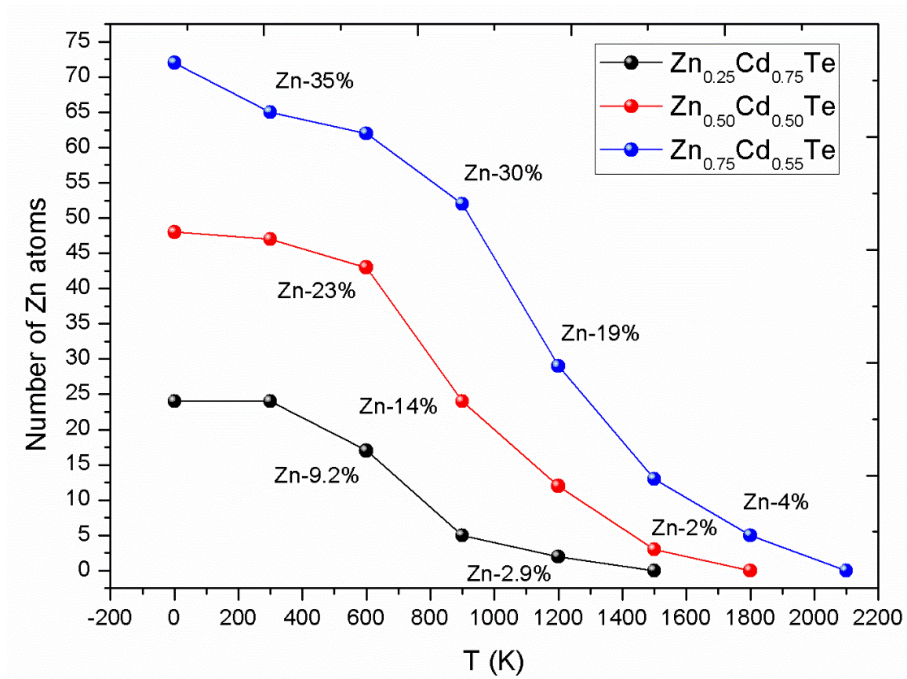


Figure 17. The number of Zn atoms variation with temperature for $\text{Zn}_x\text{Cd}_{1-x}\text{Te}$ nanorod models.

Table 3. Number of atoms in the ZnCdTe nanorod models at different temperatures.

T(K)	$\text{Zn}_{0.25}\text{Cd}_{0.75}\text{Te}$			$\text{Zn}_{0.50}\text{Cd}_{0.50}\text{Te}$			$\text{Zn}_{0.75}\text{Cd}_{0.25}\text{Te}$		
	Zn	Cd	Te	Zn	Cd	Te	Zn	Cd	Te
1	24	72	96	48	48	96	72	24	96
300	24	72	96	47	48	96	65	24	96
600	17	72	96	43	48	96	62	24	96
900	5	72	96	24	48	96	52	24	96
1200	2	72	96	12	48	96	29	24	96
1500		71	96	3	48	96	13	24	96
1800					48	96	5	24	96
2100								24	96

Figure 18 shows (a) the total interaction energies with respect to temperature and (b) the snapshots of $\text{Zn}_{0.25}\text{Cd}_{0.75}\text{Te}$ nanorod at different temperatures. As can be seen from Figure 18, the structure of the $\text{Zn}_{0.25}\text{Cd}_{0.75}\text{Te}$ nanorod changes depending on temperature. When the temperature reaches 900 K, the energy of the system begins to rise and after reaching 300 K, Zn atoms start to separate from the composition up until 1500 K, where they then disappear completely. As temperature increases, a uniformly distributed $\text{Zn}_{0.25}\text{Cd}_{0.75}\text{Te}$ nanorod becomes a more random distribution. The cross sections as well as the top view of the nanorods simulated are displayed in Figure 18 (b). As seen in the Figure 18 (b) the change from the nanorod structure to the tubular structure takes place as a result of increasing temperature.

Figure 19 shows (a) the total interaction energies with respect to temperature and (b) the snapshots of $\text{Zn}_{0.50}\text{Cd}_{0.50}\text{Te}$ nanorod at different temperatures. As can be seen from the figure the structure of the $\text{Zn}_{0.50}\text{Cd}_{0.50}\text{Te}$ nanorod shows a dependence on temperature increase and stoichiometry. When the temperature reaches 900 K, the energy of the system begins to rise. Zn atoms evaporate completely at a temperature of 1800 K and CdTe atoms remain and display a uniform structure. After reaching a temperature of 300 K, the nanorod starts to form a tubular structure as clearly seen

from the cross section of the side view. In addition to this, Zn atoms show a tendency to separate from the nanorod with temperature increase like the other composition ($\text{Zn}_{0.25}\text{Cd}_{0.75}\text{Te}$). However, $\text{Zn}_{0.25}\text{Cd}_{0.75}\text{Te}$ and $\text{Zn}_{0.50}\text{Cd}_{0.50}\text{Te}$ nanorods have different structural characteristics from each other.

The total interaction energies with respect to temperature (a) and the snapshots of $\text{Zn}_{0.75}\text{Cd}_{0.25}\text{Te}$ nanorod at different temperatures (b) are displayed in Figure 20 for $x=0.75$. Zn atoms in this model decrease significantly from 72 atoms to 0 atoms when the temperature increases from 1 to 2100 K. After reaching a temperature of 1800 K, only Cd and Te atoms remain in the nanorod. Unlike the other compounds, a three-dimensional $\text{Zn}_{0.75}\text{Cd}_{0.25}\text{Te}$ nanorod becomes a two-dimensional structure between 1200 K and 1800 K. Figure 20 clearly shows both sides and cross section views. It is interesting to note that after reaching 1800 K a 2D structure changes to become 3D in some sort of capsule like structure connected with an atom chain.

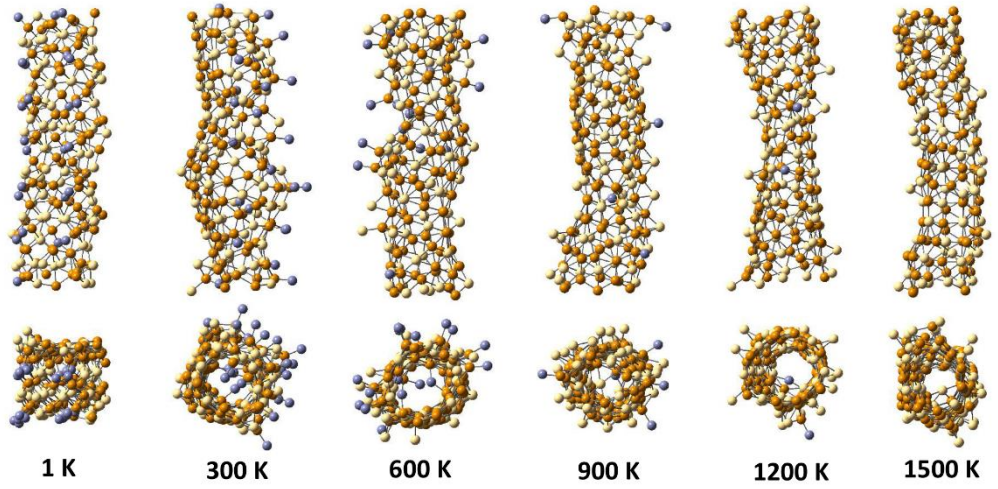
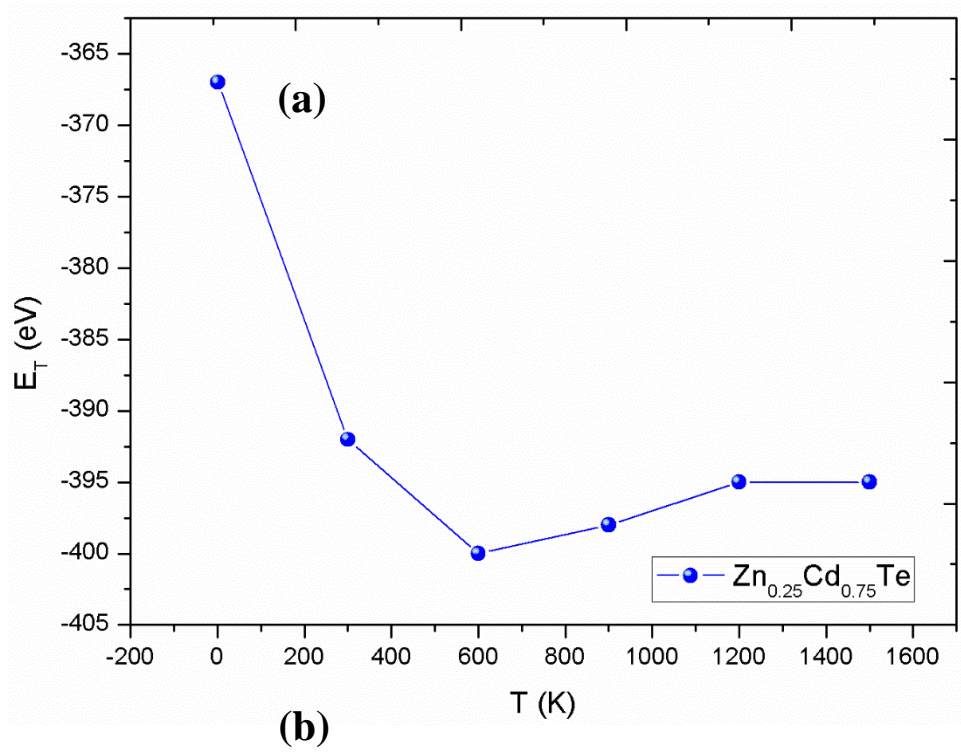


Figure 18. (a) The total interaction energies with respect to temperature and (b) the snapshots of $\text{Zn}_{0.25}\text{Cd}_{0.75}\text{Te}$ nanorod at different temperatures.

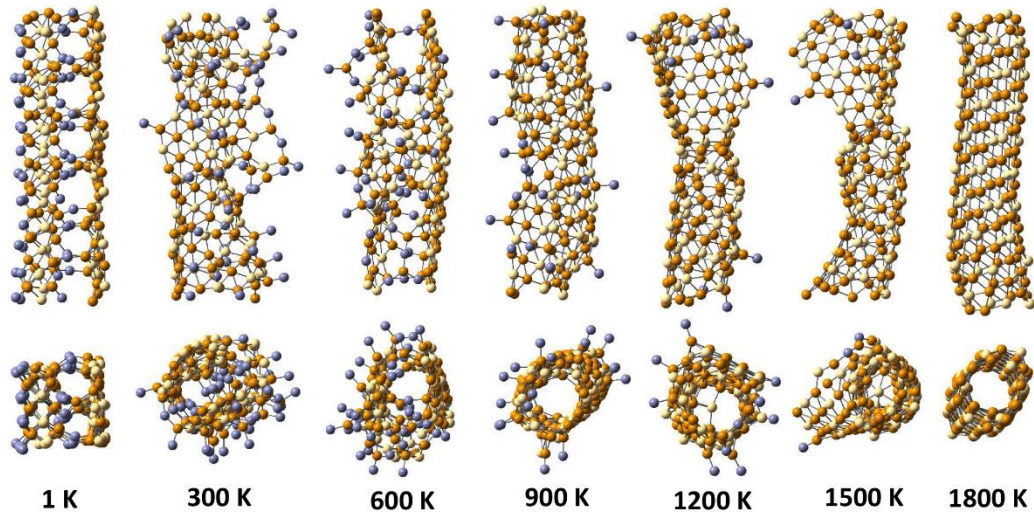
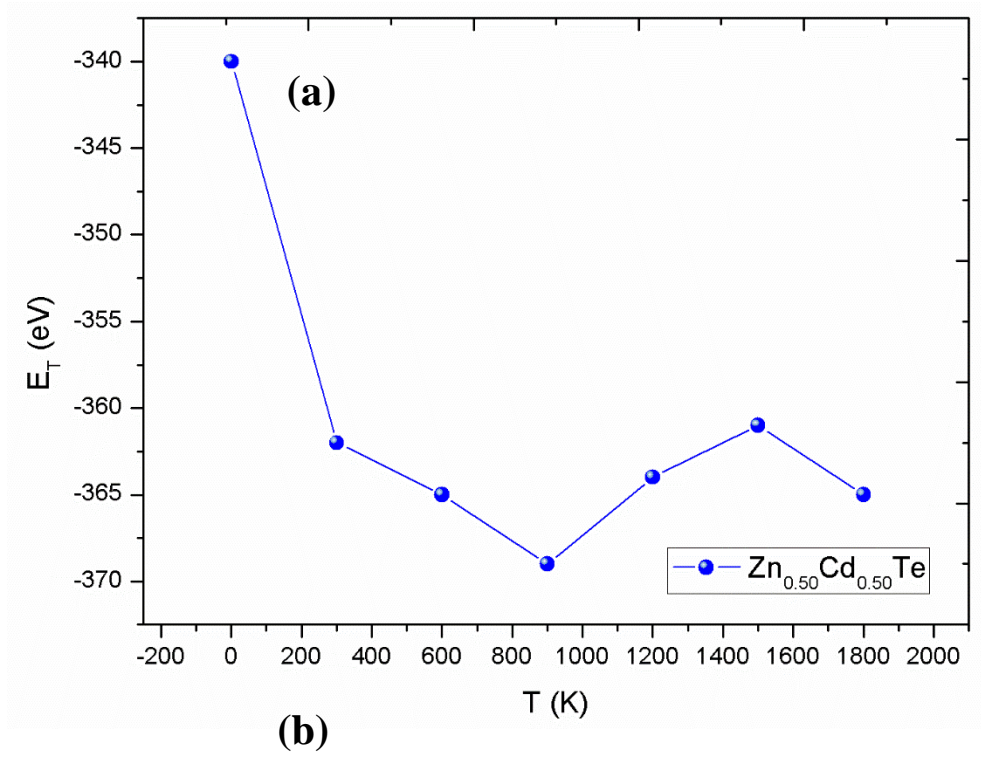


Figure 19. (a) The total interaction energies with respect to temperature and (b) the snapshots of $\text{Zn}_{0.50}\text{Cd}_{0.50}\text{Te}$ nanorod at different temperatures.

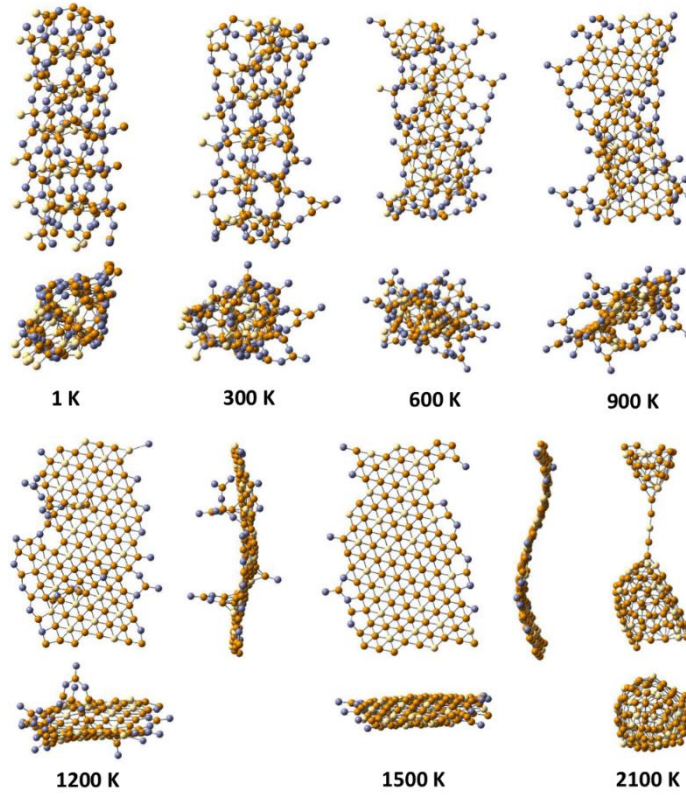
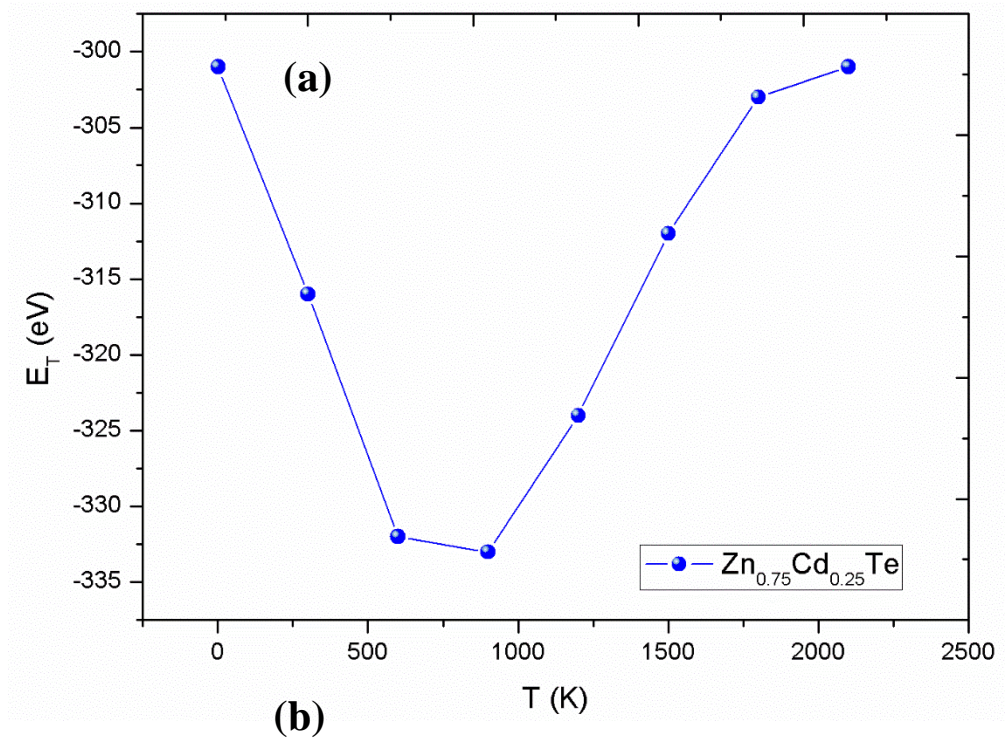


Figure 20. (a) The total interaction energies with respect to temperature and (b) the snapshots of $\text{Zn}_{0.75}\text{Cd}_{0.25}\text{Te}$ nanorod at different temperatures.

3.2 Investigation of the Structural Properties of CdTe and ZnTe Nanorods Under Heat Treatment: Molecular Dynamics Simulations

3.2.1 Introduction

A classical MD simulation using a recently developed CdZnTe atomistic many-body PEF is carried out to study the structural properties of CdTe and ZnTe binary nanorods at various temperatures. It has been explored that the structural properties of CdTe and ZnTe binary nanorods show a considerable dependence on temperature. In the case of the ZnTe binary alloy, Zn atoms separate first and pure Te system remains, however, in the case of CdTe binary, both atoms remain even at high temperatures.

3.2.2 Modelling and Calculation Procedure

In this study, a many-body PEF is used depending Lennard-Jones and Axilrod-Teller functions. Thermal equilibrium was controlled by choosing a simple velocity scaling thermostat. The statistical averages were controlled in every 500 steps. The simulations are carried out by starting at 1 K, and then temperature is increased up to 2400 K and 3300 K for ZnTe and CdTe binary nanorods, respectively. Initially, ZnTe and CdTe nanorods were equilibrated in 55000 time steps at 1 K. After relaxing the nanorods at 1 K, temperature increments with 300 K steps were applied. At each temperature increment, the systems are relaxed for about 0.21 ns [210000 time steps (each time step is 1.0 fs)] depending on the temperature of the nanorod studied. The systems are relaxed until they reach equilibrium energetically. Maxwell-Boltzmann velocity distribution is utilized to generate particle velocities at the corresponding temperature. The cut-off radius of 7.0 Å was used for maximum interaction range. Canonical ensemble (NVT) was utilized for thermal equilibrium. In order to build nanorod from the CdTe and ZnTe unit cells, a periodic boundary condition was

imposed along the rod axis (z-axis in our case). The initial cell size (x, y, and z) of both ZnTe and CdTe nanorod models considered in the present study are 10.6, 10.6 and 33.5 Å, respectively. In these nanorod structures, there are 96 Te atoms and 96 Zn or Cd atoms in each model. The models presented and investigated in this study by MD simulations are the first in the literature. ZnTe and CdTe binary nanorods considered in this study are in cubic ZB structure with lattice constants 6.089 [122] and 6.481 [123] Å, respectively. Cross section and side views of the initial structures of the ZnTe and CdTe nanorod models are shown in Figure 21.

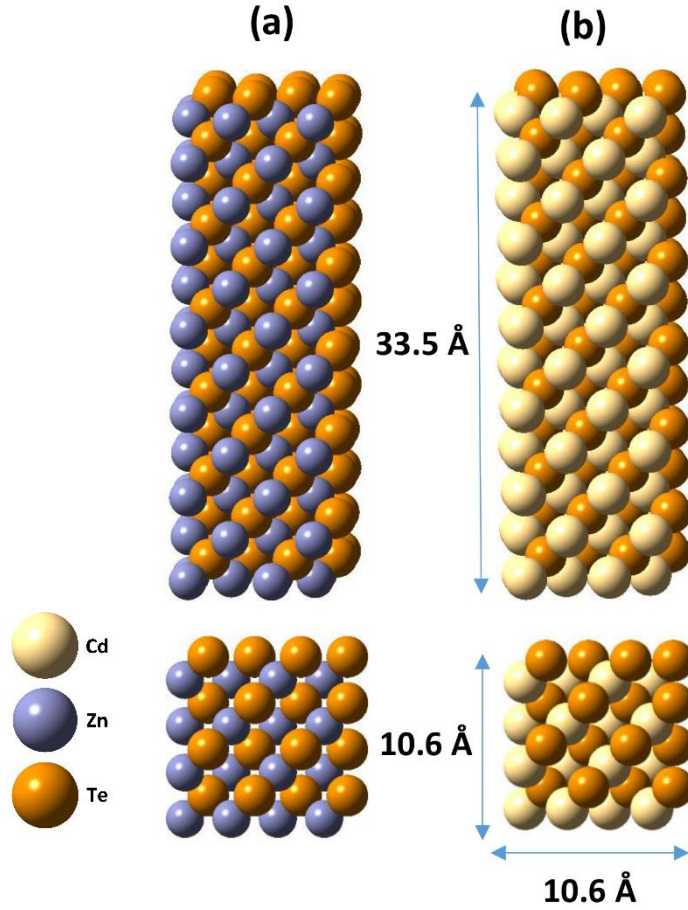


Figure 21. Side and cross section views of the generated structures of (a) ZnTe and (b) CdTe nanorod models.

3.2.3 Results and Discussions

Having fixed the atomistic potential parameters, we have used the ZnCdTe PEF in the simulations of nanorods of CdTe and ZnTe, by MD technique. The structures and energetics of the simulation results are displayed in the Figures 22-25.

Figure 22 shows total energy variation with temperature for ZnTe and CdTe nanorods. As seen in figure, the total energy of the system begins to rise when the temperature reaches 900 K and after reaching 600 K.

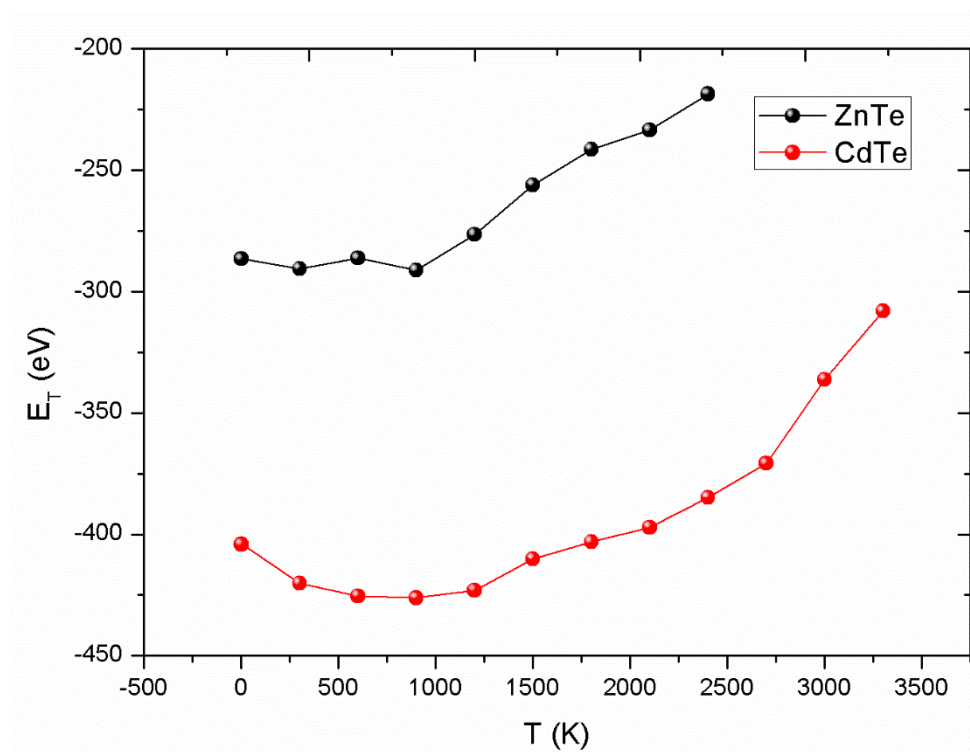


Figure 22. Total energy variation in terms of temperature for ZnTe and CdTe nanorods.

Figure 23 shows side and cross-section views of the ZnTe at different temperatures. From Figure 23, we can see that the structure of the ZnTe nanorod changes significantly depending on temperature. As temperature increases, a uniformly distributed ZnTe nanorod becomes a more random distribution. The change from the nanorod structure to a 2D structure takes place until 1500K. After that, the 2D structure changes to become 3D in some sort of capsule between 1800 and 2100K. The 3D capsule structure starts to form a tubular structure at 2400 K as clearly seen from Figure 23.

Figure 24 displays side and cross-section views of CdTe nanorod at different temperatures. As can be seen from the figure the structure of CdTe nanorod shows a dependence on temperature increase. When the temperature reaches 900 K, the energy of the system begins to rise (see Figure 24). After reaching a temperature of 2100 K, the nanorod starts to form a capsule like structure as clearly seen in Figure 24. The structure forms a tubular structure at 3000K. Interestingly increasing temperature more causes the tubular structure to form a capsule like structure again.

Figure 25 shows the number of atoms remaining in terms of different temperatures for ZnTe and CdTe nanorod models. Zn atoms in this model decrease significantly from 96 atoms to 0 atoms when the temperature increases from 1 to 2400 K and pure Te system remains in the ZnTe nanorod model. Cd atoms separate at a temperature of 3300 K; however, in this case; both atoms remain even at high temperatures in the CdTe nanorod model. It is interesting to note that the structures at low temperatures (even at 1 K) show a slight distortion, which is not expected at normal conditions. This is due to the weak pair interaction (ϵ_0) between the atoms (in the order of 0.015 – 1.20 eV) of the materials studied. Cd atom release from CdTe nanowires was also observed experimentally [47]. The present results showing atom release consistent with experimental findings. Figure 26 shows the experimental result of Cd atom release with respect to temperature.

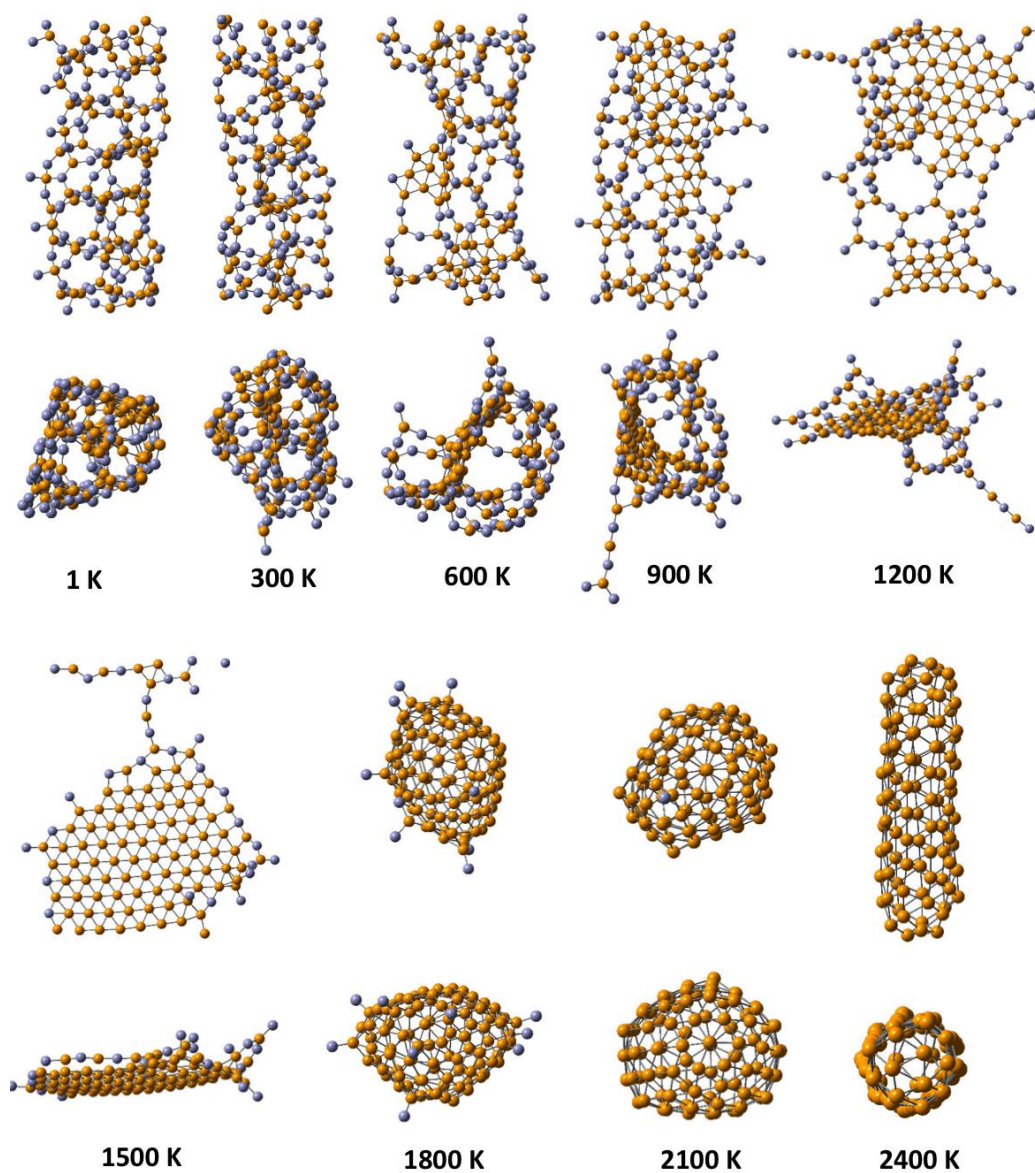


Figure 23. The structures of ZnTe nanorod at different temperatures. Pictures show side and cross-section views.

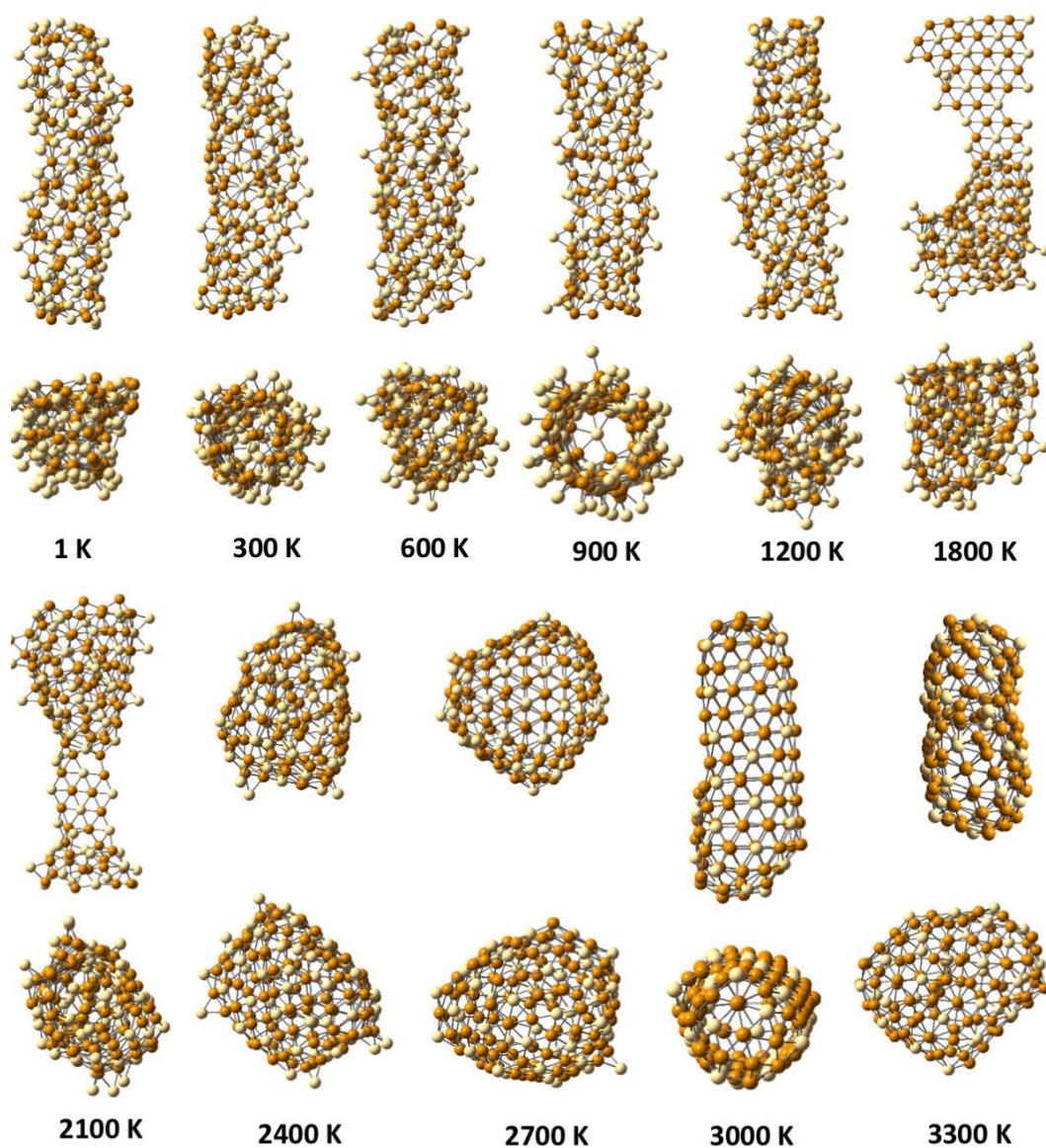


Figure 24. The structures of CdTe nanorod at different temperatures. Pictures show side and cross-section views.

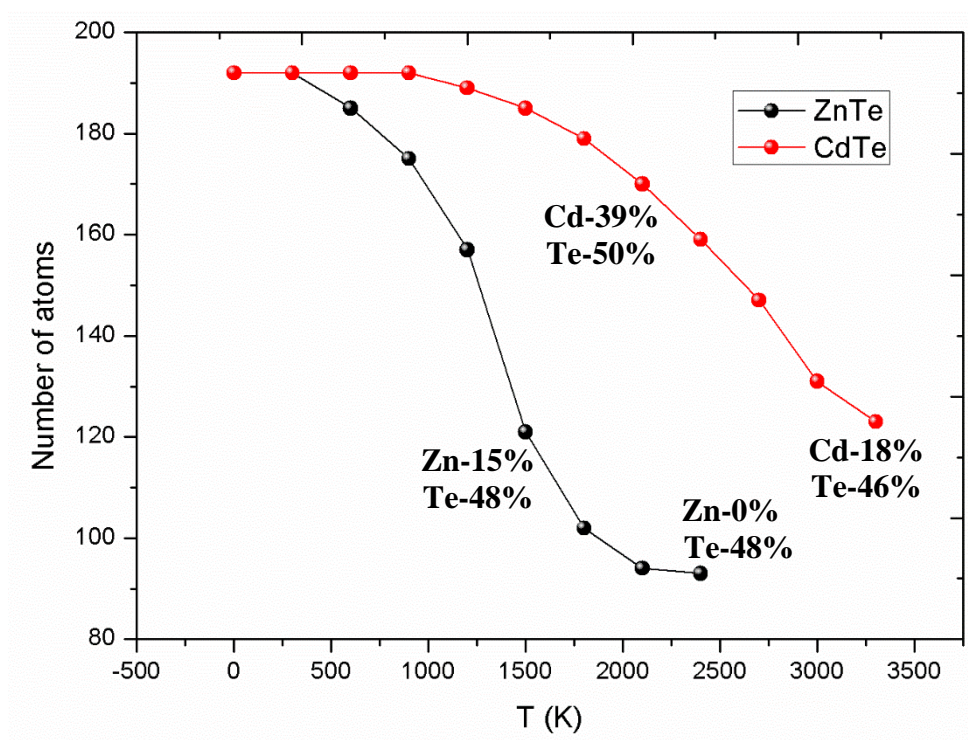


Figure 25. The number of atoms variation with temperature for ZnTe and CdTe nanorods.

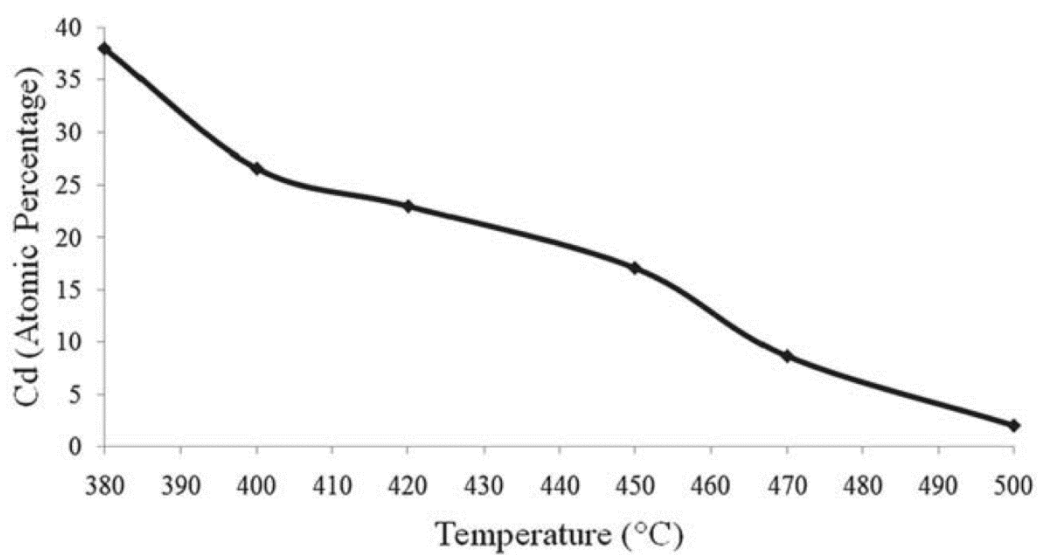


Figure 26. Cd atom release with respect to temperature in CdTe nanorod [47].

3.3 Mechanical Properties of CdZnTe Nanowires Under Uniaxial Stretching and Compression: A Molecular Dynamics Simulation Study

3.3.1 Introduction

Structural and mechanical properties of ternary CdZnTe nanowires have been studied via MD simulations using BOP. The simulation procedures are carried out as uniaxial stretching and compression at 1 K and 300 K. The results demonstrate that the mechanical properties of CdZnTe ternary nanowires show significant dependence on size and temperature under uniaxial stretching and compression.

3.3.2 Modelling and Calculation Procedure

CdZnTe compound crystallizes in the zinc-blende structure as shown Figure 1. The CdZnTe NWs considered have 263 and 641 atoms with the wire length of 70 Å in the y direction and a square cross section with lengths of 10 Å and 17 Å in the x- and z- directions, respectively. The generated view of the modeled NWs is shown in Figure 27.

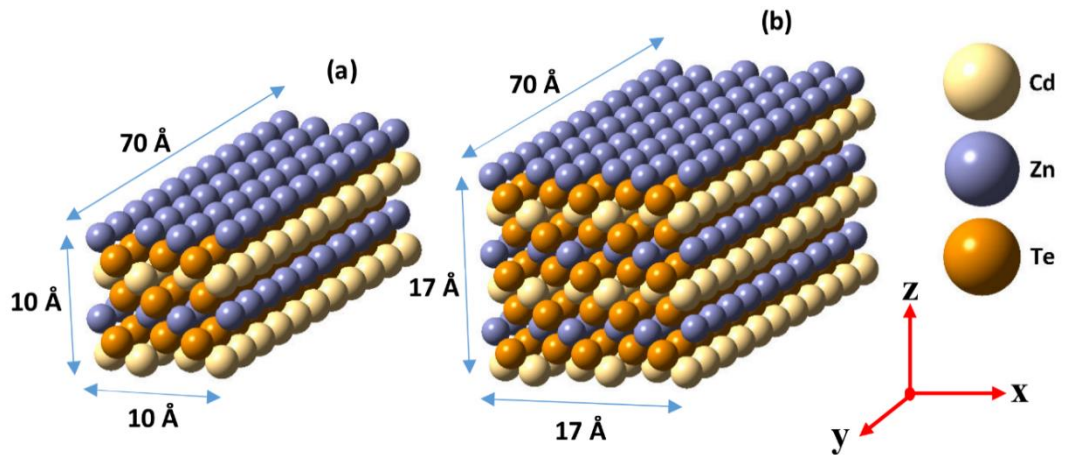


Figure 27. The generated view of the modeled nanowires with (a) 263 atoms (model-1, M1) and (b) 641 atoms (model-2, M2).

Simulations were carried out with strain rate of 5% and at two different temperatures; the temperatures selected are 1 and 300 K. Nosé-Hoover thermostat and the canonical ensemble (NVT) are used to control thermal equilibrium during the whole simulations. In the computations, the heating procedure is applied, where the temperature of the system was equilibrated at 1 and 300 K for the CdZnTe NWs with different sizes and then applied uniaxial stretching and compression at the equilibrated temperatures. For both NW models in each stretching and/or compression step 50000 MD time steps (50 ps) were found to be sufficient to achieve thermal stability at 1 K. Similarly at 300 K about 120000 MD steps (120 ps) were found to be sufficient to achieve the stability. Boltzmann velocity distribution was used to generate initial particle velocities at the corresponding temperature. The cut-off radius of 14.70 Å was used for maximum interaction range.

The CdZnTe NWs were subjected to uniaxial stretching and compression by moving all the atoms in the y-direction (Figure 28).

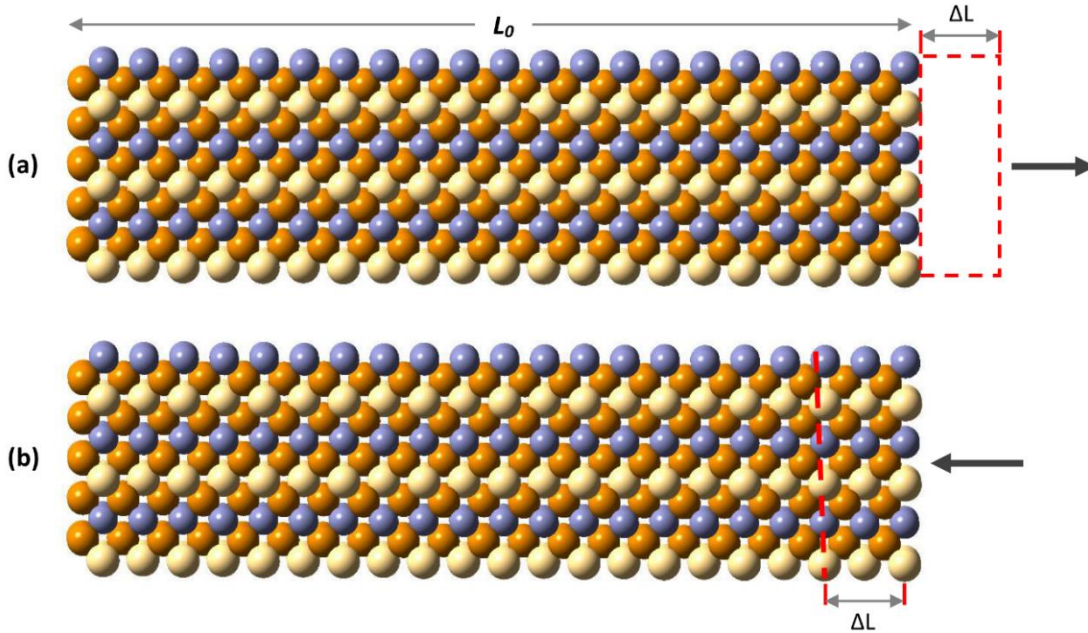


Figure 28. (a) Stretching model: The NW is stretched a length ΔL along its length. (b) Compression model: The same NW is compressed a length ΔL along its length.

A periodic boundary condition was adopted along the wire axis. In the stretching process the y-coordinate of all the atoms are changed as $y_i = y_i * 1.05$, whereas in the compression process the y-coordinate of all the atoms are changed as $y_i = y_i * 0.95$. The percentage of change in the length of the NW is calculated as:

$$\Delta L_i = \frac{L_i - L_0}{L_0} * 100 \quad (3.1)$$

In Eq. (3.1), L_i is the length at stretching step i and L_0 is the initial length of the NW. Strain energy is defined as $\Delta E_i = E_i - E_0$ where E_0 and E_i are the total energy of the initial and stretching step i .

3.3.3 Results and Discussions

The mechanical properties of the simulated CdZnTe ternary nanowires are presented under the constant strain rate and at different temperatures. Strain energy with respect to strain and the snapshots of the corresponding stretched structures are shown for the NW M1 at 1K and 300 K in Figure 29. From Figure 29 (a), at 1 K the NW appears to preserve its overall structure under stretching and seems still undeformed until step 5 (about 17.0% overall stretching with respect to the initial length). After stretching step 5, the NW structure starts to be deformed, particularly from the end regions. The snapshot in step 6 (20.43%) indicates that the nanowire is broken. The simulation of the same structure at 300 K exhibits somewhat different consequences as seen from Figure 29 (b). In contrary with the low temperature (1 K) case, in which the break-up occurs at higher strain step, as the temperature goes up, the required strain for this phenomenon decreases, namely the NW is broken earlier at 300K. In addition, we can also see from the total energy changes and strain, the energy of the nanowire suddenly drops due to the break-up.

In the second part of the simulation, the effect of the size (the cross-section area), which is an important parameter in the ductility of NWs, is investigated on the CdZnTe NWs at different temperatures, 1 and 300 K, and constant strain rate. The strain energy with respect to strain and the snapshots of the corresponding stretched structures for

CdZnTe NW M2 at 1 and 300 K are shown in Figure 30. From (a), the NW M2 has the most tendency to stretch at 1 K without completely the break-up until step 11 (60.12%), which fragments into two pieces. Similar to M1 case, M2 also deforms earlier at 300 K and breaks at stretching step 6 (Figure 30 (b)). This characteristic of the strain energy-strain curve is shown in Figure 30 (a) and (b).

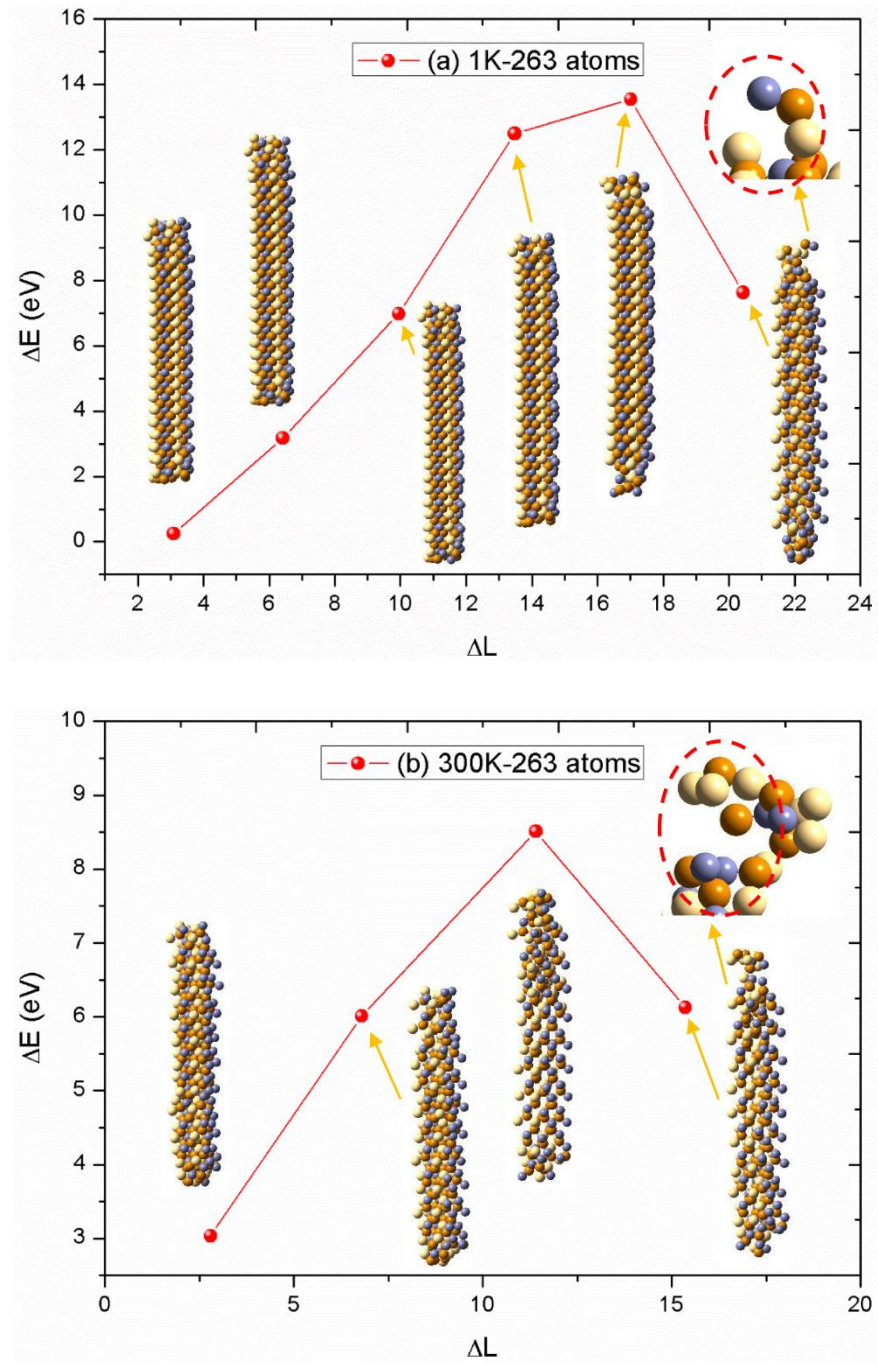


Figure 29. Strain energy (ΔE) with respect to strain (ΔL (%)) and the snapshots of stretching process for CdZnTe NW M1 at (a) 1 K and (b) 300 K.

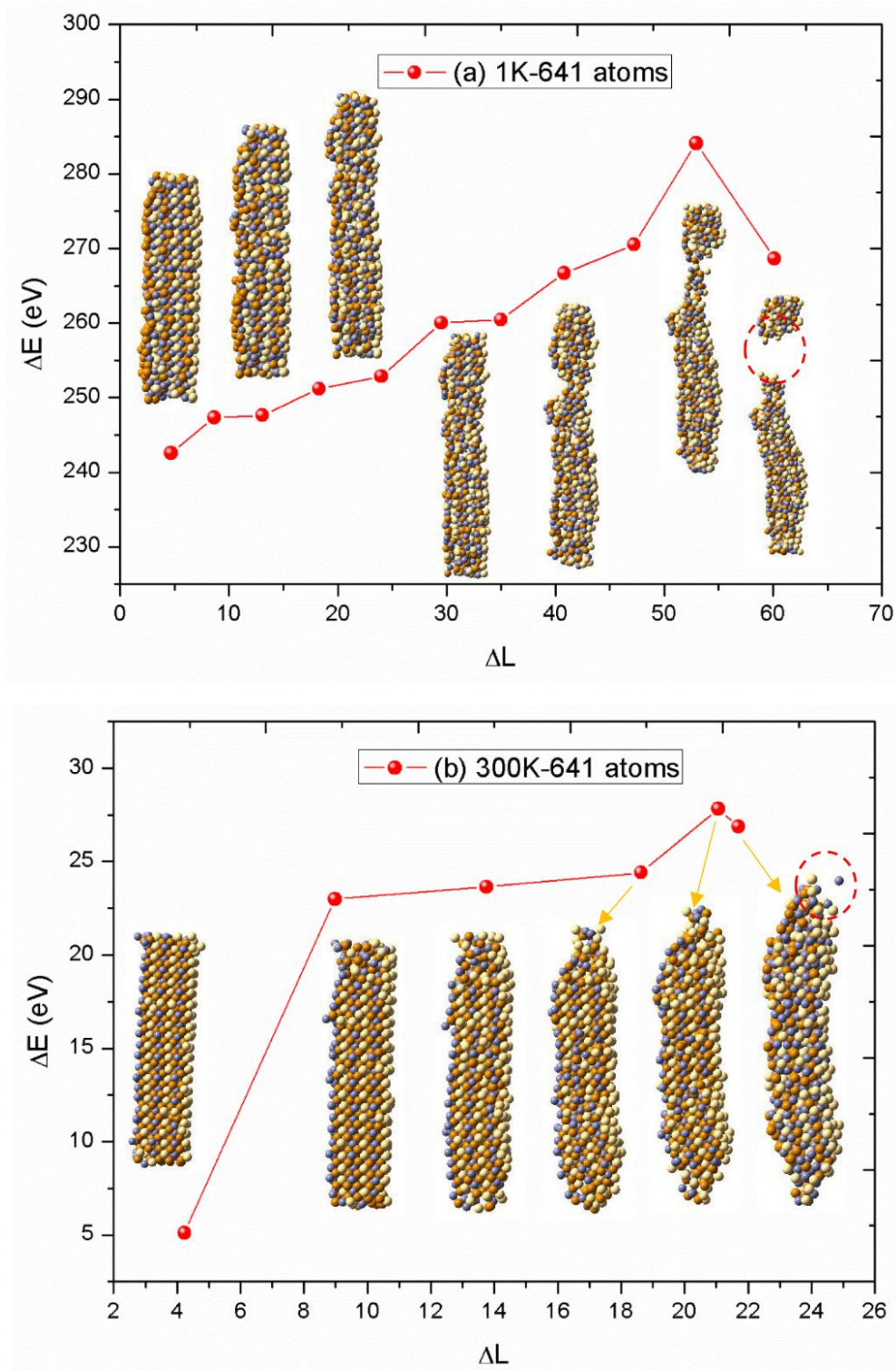


Figure 30. Strain energy (ΔE) with respect to strain (ΔL (%)) and the snapshots of the corresponding stretched structures for CdZnTe NW M2 at (a) 1 K and (b) 300 K.

In the last part of this study, the effect of the compression application is investigated on the CdZnTe NW M2 at 1 and 300 K. From Figure 31, further compression causes the atoms in the NW to undergo significant rearrangement. In the last compression step 19, the NW looks like a nanoparticle with amorphous structure. It is interesting to note that at 300 K in the second compression step Cd atoms start to eject from the NW. We stopped the compression procedure at this point. Therefore, we can infer that temperature has a significant effect on the Cd atoms. This result is consistent with recent experimental findings [47] and our theoretical calculations (see section 3.1 and 3.2). According to the experimental high resolution transmission electron microscope findings, the Cd content of the NW decreases with increasing temperature. Similar trend has also been obtained in MD simulations of CdTe and ZnCdTe nanorods with a different PEF. Comparing the binding energy of three atoms (Cd, Zn and Te), Cd atom has the smallest value, which explains why Cd leaves the system first (see Table 2).

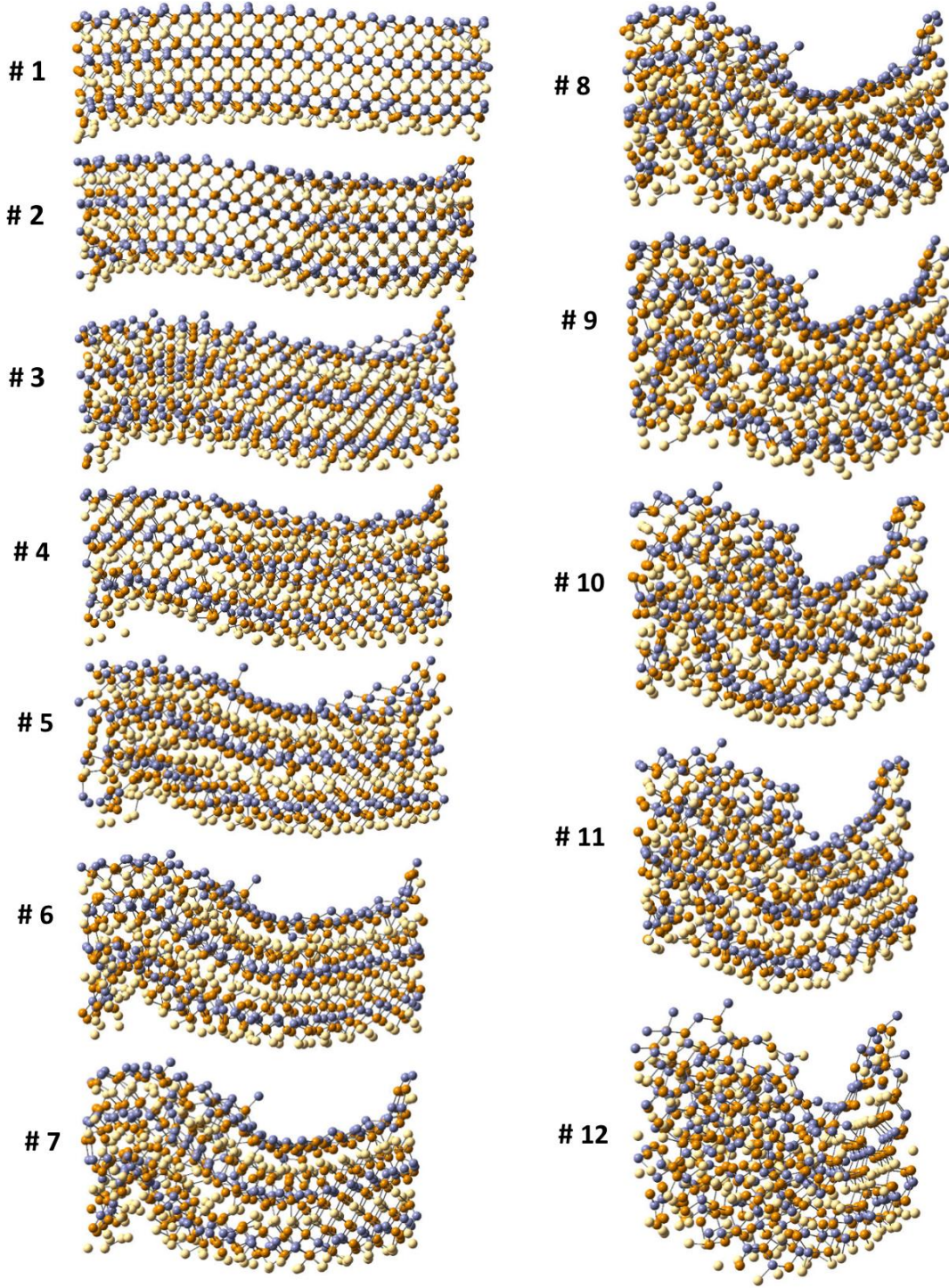


Figure 31. The snapshots of the CdZnTe NW M2 at 1 K until 19 compression steps. All the pictures show side views, except #19a is for side view, #19b is for cross view.

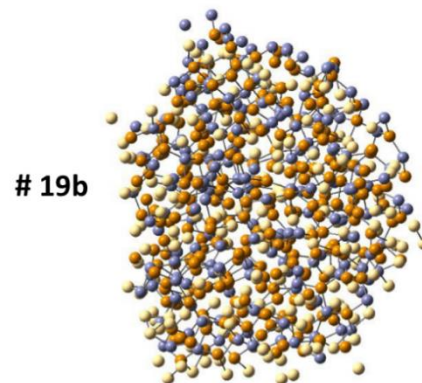
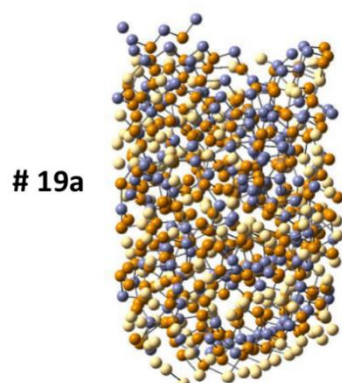
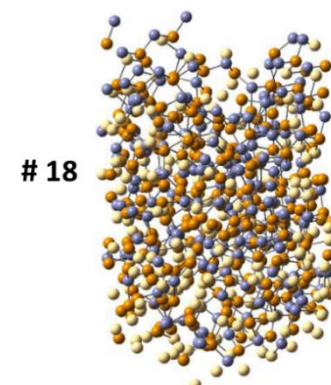
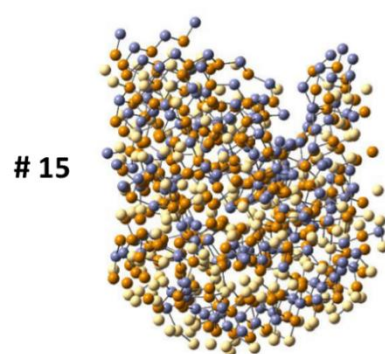
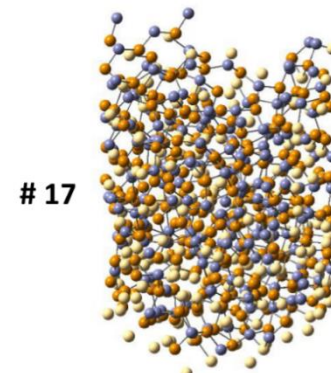
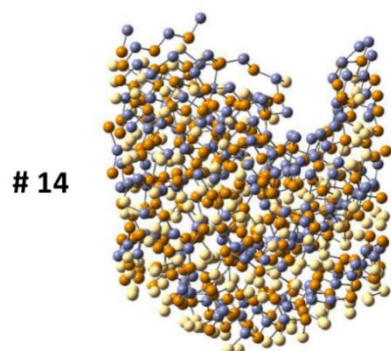
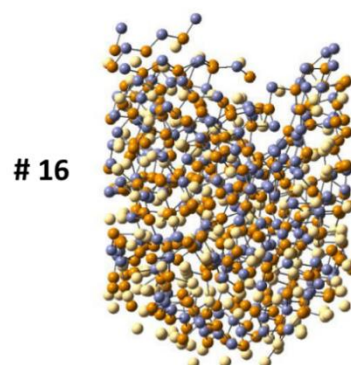
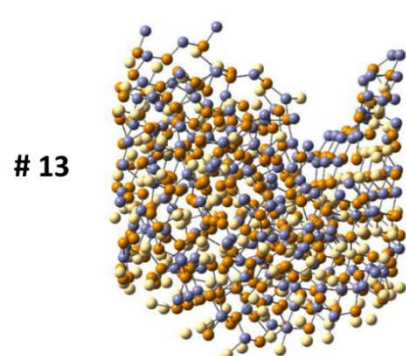


Figure 29. (Continued).

3.4 Structural and Electronic Properties of $Zn_mCd_nTe_k$ ($m+n+k = 2-4$) Clusters: DFT Calculations

3.4.1 Introduction

The structural and electronic properties of isolated neutral $Zn_mCd_nTe_k$ clusters for $m + n + k = (2 - 4)$ have been studied by DFT calculations at B3LYP/CEP-121G level. The electronic ground state has been found to be spin triplet for the clusters Te_2 , $CdTe$, $ZnTe_2$, and $CdTe_2$, the rest have been found to have a spin singlet state. The optimum geometries, charge density, spin density, electrostatic potential, excess charge on atoms, dipole moments, vibration frequencies, HOMO, LUMO, HOMO-LUMO gaps (E_g), the possible dissociation channels and energies of the cluster models considered have been obtained. The energy gap (E_g) decreases when number of atoms in the clusters increases.

3.4.2 Modelling and Calculation Procedure

The structural and electronic properties of small isolated neutral $Zn_mCd_nTe_k$ clusters for $m + n + k = 2 - 4$ have been studied via DFT at the B3LYP/CEP-121G level. Various spin multiplicities were investigated and it has been found that the majority of the models have spin singlet as the most stable (minimum total energy), and a few models have spin triplet as the most stable. All cluster geometries were optimized without imposing any symmetrical constraints and the lowest total energy configuration was assumed as the global minimum case. The structures are taken as the local minima on potential energy surface having positive vibration frequencies. GAUSSIAN09 program [124] package have been used in the calculations. Molecular structures have been visualized using GaussView [125].

3.4.3 Results and Discussions

Extensive literature survey shows that Zn_2 , Cd_2 , Te_2 , ZnCd , ZnTe , CdTe dimers of Cd, Zn and Te triple have greatly been investigated as discussed in the introduction section. However, the ternary ZnCdTe clusters have not been investigated extensively. However, there is currently only one work about ternary clusters of $\text{Zn}_m\text{Cd}_n\text{Te}_y$ for $y=6$ and 8 with TDDFT calculations considering only spin singlet cases [126]. In the present study all possible combinations of $m+n+k=2-4$ have been taken into account considering different spin multiplicities.

$\text{Zn}_m\text{Cd}_n\text{Te}_k$ Clusters for $m+n+k=2$:

We begin the study of $\text{Zn}_m\text{Cd}_n\text{Te}_k$ clusters by investigating Zn_2 , Cd_2 , Te_2 , ZnCd , ZnTe , and CdTe dimer structures with lowest energy by optimizing the system. The dimers were optimized and minimum total energies were calculated. The spectroscopic constants for the dimers are listed in Table 4. Total energies are given in a.u. (Hartree). The binding energy has been defined and calculated using the relation: $E_b = E_A + E_B + E_C - E_{ABC}$. This relation always gives a positive value for binding energy. The calculated spectroscopic constants of the ground state of Zn_2 dimer is compared in Table 4 together with the theoretical and experimental results from other studies. There are some studies on dimers Zn_2 , Cd_2 , Te_2 , ZnCd , ZnTe , and CdTe . The studies conducted on the dimers have so far not been addressed for the various possible spin multiplicities. The results of the present calculations indicated that for Te_2 and CdTe , spin multiplicity at 3 (spin triplet) is the lowest state in linear geometry. The total magnetic moment for Te_2 and CdTe clusters are found to be 6 and $13 \mu_B$ respectively. Figure 32 shows the optimized geometries, bond distances, excess charges, spin density (SD), charge density (CD) and electrostatic potential (ESP) of all the diatoms.

Table 4. Spectroscopic constants of the possible dimer combinations. Dissociation energy (D_e), equilibrium distance (r_e) the vibrational frequency (ω_e), total energy (E_T in Hartree), the multiplicities of the spin system ($2S+1$), the dipole moments (μ in Debye). $E_T(\text{Zn}) = -226.126$, $E_T(\text{Cd}) = -166.937$ and $E_T(\text{Te}) = -7.974$. The corresponding total energies for the triplet states are given in the parenthesis.

Dimers	$D_e(\text{eV})$	$r_e(\text{\AA})$	$\omega_e(\text{cm}^{-1})$	E_T	$2S+1$	μ
Zn ₂	0.012	3.559	32.97	-452.253	1	0.00
	0.022 ^a	4.11 ^a , 2.51 ^g	21.0 ^a			
	0.272 ^g	4.19 ^b , 4.51 ^k	25.9 ^b			
				-452.152	3	
Cd ₂	0.007	4.013	18.17	-333.875	1	0.00
	0.029 ^a	4.013 ^a , 2.74 ^h	18.0 ^a			
	1.415 ^h					
				-333.769	3	
Te ₂	4.902	2.700	222.37	-16.128	3	0.00
	4.108	2.700	220.63	-16.099	1	0.00
	1.415 ^g	2.557 ^d , 2.74 ^g	246.0 ^d			
ZnCd	0.010	3.703	24.79	-393.064	1	0.02
				-392.962	3	
ZnTe	1.834	2.417	241.90	-234.168	1	4.19
	0.721 ^g	2.540 ^g , 2.641 ^c	186.0 ^c			
CdTe	1.738	2.619	110.90	-234.166	3	
	1.632	2.619	188.72	-174.975	3	1.91
	1.57 ^f	2.80 ^c , 2.92 ^h	188.75 ^f , 152 ^c	-174.971	1	4.88

^a[127] PP, CPP; CCSD(T), ^b[128] Exp., ^c[129] Exp., ^d[130] Exp., ^f[131] FPMD, ^g[66] BOP, ^h[87] BOP, ^k[132] Ab-initio

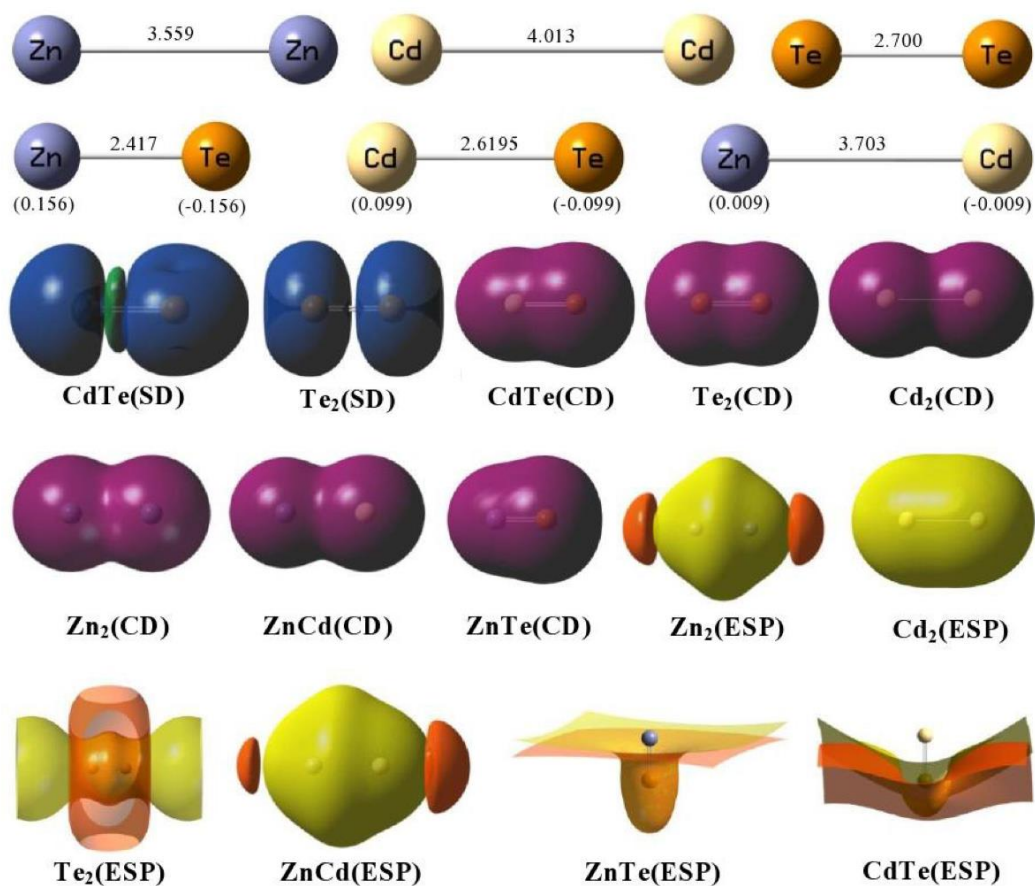


Figure 32. Dimer geometries (Zn is purple, Cd is grey and Te is orange), spin density (SD), charge density (CD) and electrostatic potential (ESP) pictures of dimers. Green (alpha spin) and blue (beta spin) colors represent the positive and negative spin density, respectively. Electrostatic potential picture: yellow represents positive potential and orange negative potential. The corresponding charge densities for dimer geometries are given in the parenthesis. The color is the same in the following figures.

Figure 32 displays that the spin density distribution is not symmetric over CdTe dimer and both positive and negative parts apparent, whereas it is symmetric on Te₂ and only the negative part is apparent. Charge density is uniformly distributed for homonuclear dimers and heteronuclear ZnCd clusters, however, in dimers containing Te atom charge density is not symmetrically distributed over the atoms; charge on Te looks broader. This is due to the electronegativity property of the Te atom. ESP is a measure of electronegativity and partial charges of a molecule. As it can be seen from Figure 32, negative ESP is mainly localized over the Te atom and it looks like a yellowish blob while the positive regions are mainly localized around Zn and Cd atoms.

Zn_mCd_nTe_k Clusters for m+n+k=3:

For Zn_mCd_nTe_k clusters $m + n + k = 3$, in order to obtain geometry with the lowest energy, several atomic arrangements were considered; for instance, it was studied ZnCdTe cluster having the linear structures with ZnCdTe, ZnTeCd, and TeZnCd. This procedure was done for all the clusters in this study. The initial geometries of the clusters for $m + n + k = 3$ were chosen with all possible geometries, linear and triangular structures. The optimum structures and corresponding bond distances are shown in Figure 33. The spin density (SD), charge density (CD) and electrostatic potential (ESP) pictures of trimer clusters considered are displayed in Figure 34. From Figure 34, the spin density distribution is symmetric over the linear cluster (TeZnTe) and the negative spin density is localized on Te atoms, whereas the positive spin density localization is on Zn atom in the center. Charge density has a uniform distribution for homonuclear trimers and Zn and Cd containing trimers. On the other hand, charge density of trimers with Te atom is not equally distributed between the atoms. Positive region of the ESP is mainly localized around Zn and Cd atoms and negative region has localization around the Te atoms.

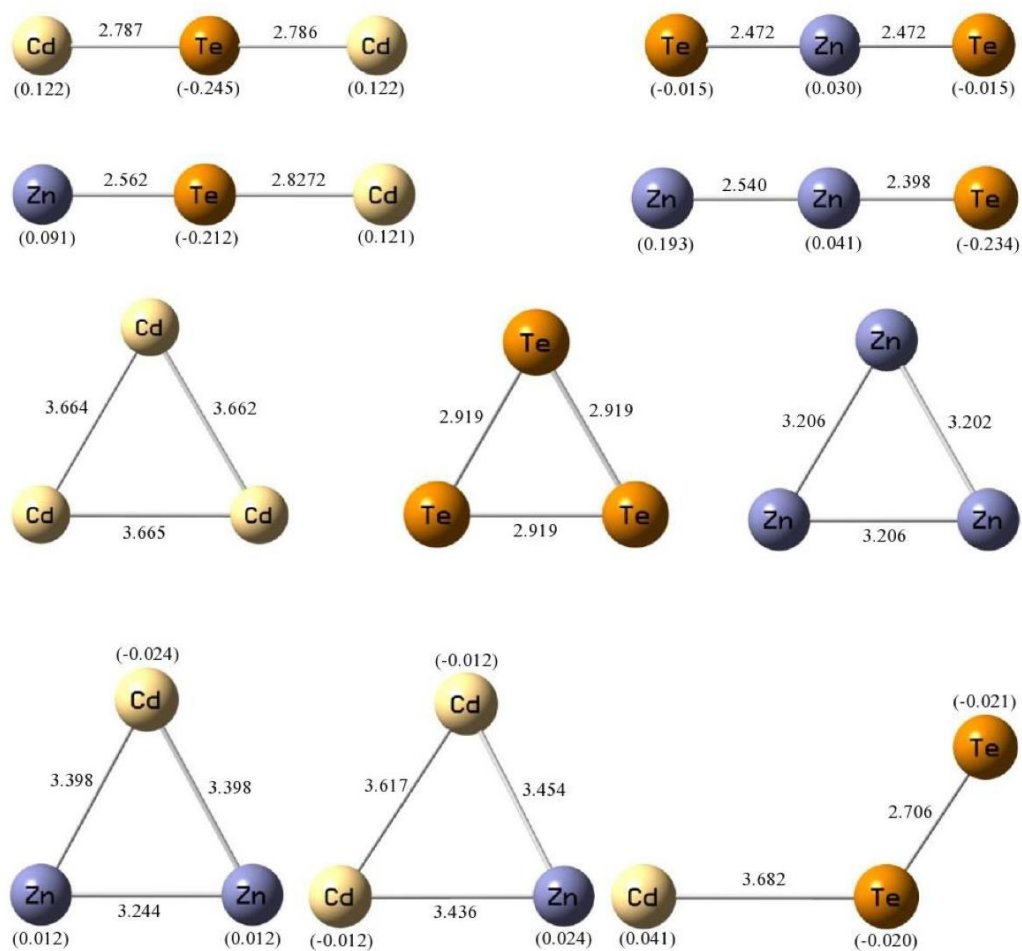


Figure 33. Trimer geometries. The corresponding charge values for trimer geometries are given in the parenthesis.

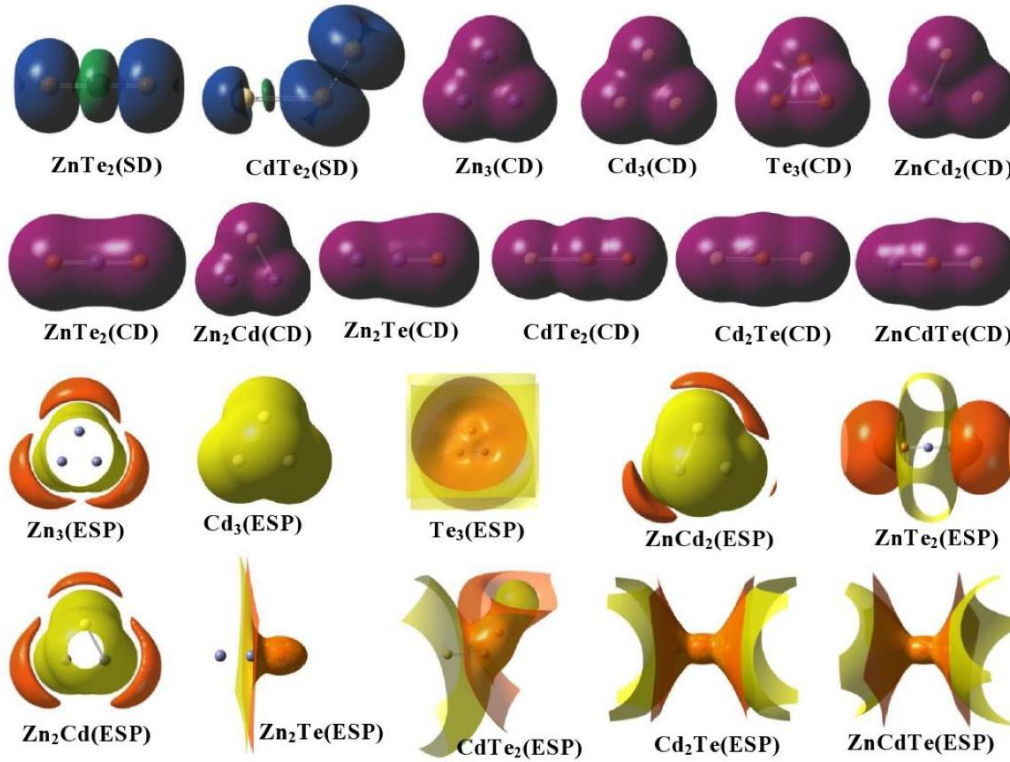


Figure 34. Spin density (SD), charge density (CD) and electrostatic potential (ESP) pictures of trimers.

The binding energies, total energy, spin multiplicity, and the dipole moments of the lowest energy structures of $\text{Zn}_m\text{Cd}_n\text{Te}_k$ clusters for $m + n + k = 3$ are given in Table 5 and the vibrational harmonic frequencies are tabulated in Table 6. Triatomic clusters for the homonuclear Zn_3 , Cd_3 and Te_3 are in equilateral triangle shape with D_{3h} symmetry. In the case of mixed (heteronuclear) clusters, the lowest-energy structures of Zn_2Cd and ZnCd_2 clusters are in isosceles triangle with D_{2v} symmetry. The isomers of these triatoms with linear geometry have local minima. The lowest total energy values of the triangular structures are slightly smaller than that of the linear shape. ZnTe_2 and Cd_2Te clusters are in linear geometry with $D_{\infty h}$ symmetry. Zn_2Te and CdTe_2 are in linear geometry with $D_{\infty v}$ and the angular C_s configuration with the Te–Te bond (see Figure 33) respectively. Zn–Te–Cd configuration among the linear ternaries has the lowest energy. The spin multiplicities considered for trimers indicate

that spin multiplicity at 3 gives the ground state for ZnTe_2 and CdTe_2 trimers (see Table 5). The total magnetic moment for ZnTe_2 and CdTe_2 clusters are found to be $10.6 \mu_B$.

Table 5. The binding energies (E_b , in eV), total energy (E_T , in Hartree), the multiplicities of the spin system ($2S+1$), and the dipole moments (μ , in Debyes) of trimer structures with lowest energy. The corresponding total energies for the triplet states are given in the parenthesis.

Dimers	Geometry	E_b	E_T	$2S + 1$	μ
Zn_3	Equilateral	0.085	-678.382(-678.279)	1(3)	0.00
Cd_3	Equilateral	0.047	-500.813(-500.726)	1(3)	0.00
Te_3	Equilateral	7.181	-24.186(-24.180)	1(3)	0.00
ZnCd_2	Isosceles	0.057	-560.003(-559.905)	1(3)	0.01
ZnTe_2	Linear	0.383	-242.270	3	0.00
	Linear	0.462	-242.242	1	0.00
Zn_2Cd	Isosceles	0.057	-619.193(-619.102)	1(3)	0.00
Zn_2Te	Linear	2.379	-460.314(-460.301)	1(3)	7.90
CdTe_2	Angular	0.016	-183.066	3	0.53
	Angular	0.027	-183.037	1	0.60
Cd_2Te	Linear	2.196	-341.929(-341.914)	1(3)	0.00
ZnCdTe	Linear	2.296	-401.122(-401.120)	1(3)	0.15

Table 6. The vibrational frequencies (ω , in cm^{-1}) of all the trimer structures with the lowest energy.

Trimers	Vibration frequencies			
	ω_1	ω_2	ω_3	ω_4
Zn ₃	49.2	50.8	53.2	
Cd ₃	26.7	28.5	32.2	
Te ₃	145.9	145.9	198.5	
ZnCd ₂	26.3	30.0	30.9	
ZnTe ₂	48.9	48.9	137.9	300.6
Zn ₂ Cd	32.7	35.6	48.9	
Zn ₂ Te	29.1	110.3	283.8	
CdTe ₂	8.8	20.0	215.7	
Cd ₂ Te	27.5	27.5	108.3	
ZnCdTe	30.2	111.5	166.2	132.5

Zn_mCd_nTe_k Clusters for m+n+k=4:

The initial trial geometries for the tetramers with all positive vibration frequencies to obtain a global minimum energy structure are linear, rhombus, tetrahedral and Y-shaped structures, in addition to square structure for homonuclear structures. The optimum structures, the bond distances, charge density (CD) and electrostatic potential (ESP) pictures of all tetramer clusters are shown in Figure 35 and Figure 36. From Figure 36, although the number of Zn, Cd and Te increases, CD and ESP distributions show the same trend like structures with two and three atoms. The binding energy, total energy, spin multiplicity, and the dipole moment of $Zn_mCd_nTe_k$ for tetramer clusters with the lowest energy are given in Table 7 and the corresponding vibration harmonic frequencies are given in Table 8. The ground state configurations of

homonuclear Zn_4 , Cd_4 and Te_4 are nearly in tetrahedral structure. A tetrahedral structure for Zn_3Cd and ZnCd_3 and Zn_2Cd_2 clusters is the most stable structure (see Figure 35). According to MD simulations [77] the structures of Zn_3Cd , ZnCd_3 and Zn_2Cd_2 clusters were in tetrahedron geometry and Zn-Cd bond distances were determined in the range 3.107-3.185 Å. In the present study the calculated values are in agreement with those bond distances in the range of 3.166-3.207 Å. A rhombus structure with D_{2h} symmetry has the lowest energy for Zn_2Te_2 tetramer while a planar (nearly rhombus) and linear structure has the lowest energy for ZnTe_3 and Zn_3Te clusters, respectively. The most stable structure of Cd_2Te_2 cluster is a tetrahedral with D_{2h} symmetry and the bond distance is 2.708 Å. Cd-Cd bond distance in Cd_2Te_2 cluster is 3.343 Å. For Cd_3Te and CdTe_3 clusters, the geometries with the lowest energy are linear and planar nearly rhombus structure, respectively.

The lowest energy geometry for Zn_2CdTe and ZnCdTe_2 is a 2D distorted rhombus and for ZnCd_2Te cluster is a linear structure. The bond distance of Zn-Te in Zn_2CdTe and ZnCd_2Te were 2.659 Å and 2.826 Å respectively. The bond distance of Zn-Te in ZnCdTe_2 was 2.403 Å. The bond distances between Zn-Te atoms in the ternary structures Zn_2CdTe and ZnCd_2Te were longer than ZnTe dimer bond length, but the bond distance between Zn-Te atoms in ternary structure ZnCdTe_2 were shorter than ZnTe dimer. On the contrary, the bond distance of CdTe dimer was shorter than Cd-Te bond lengths in the Zn_2CdTe and ZnCd_2Te clusters, however it was longer in the ZnCdTe_2 cluster (see Figure 35).

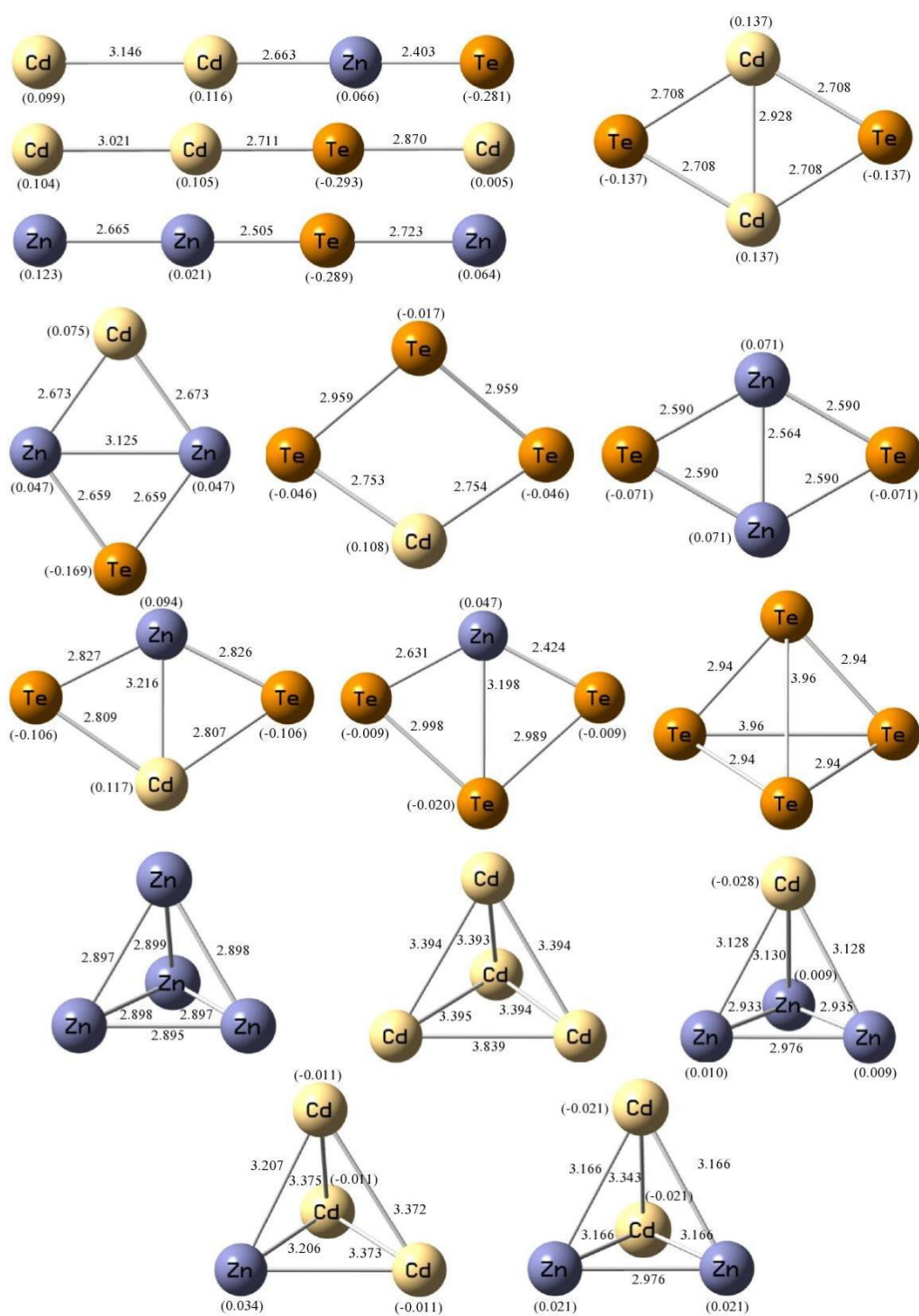


Figure 35. Tetramer geometries. The corresponding charge densities for tetramer geometries are given in the parenthesis.

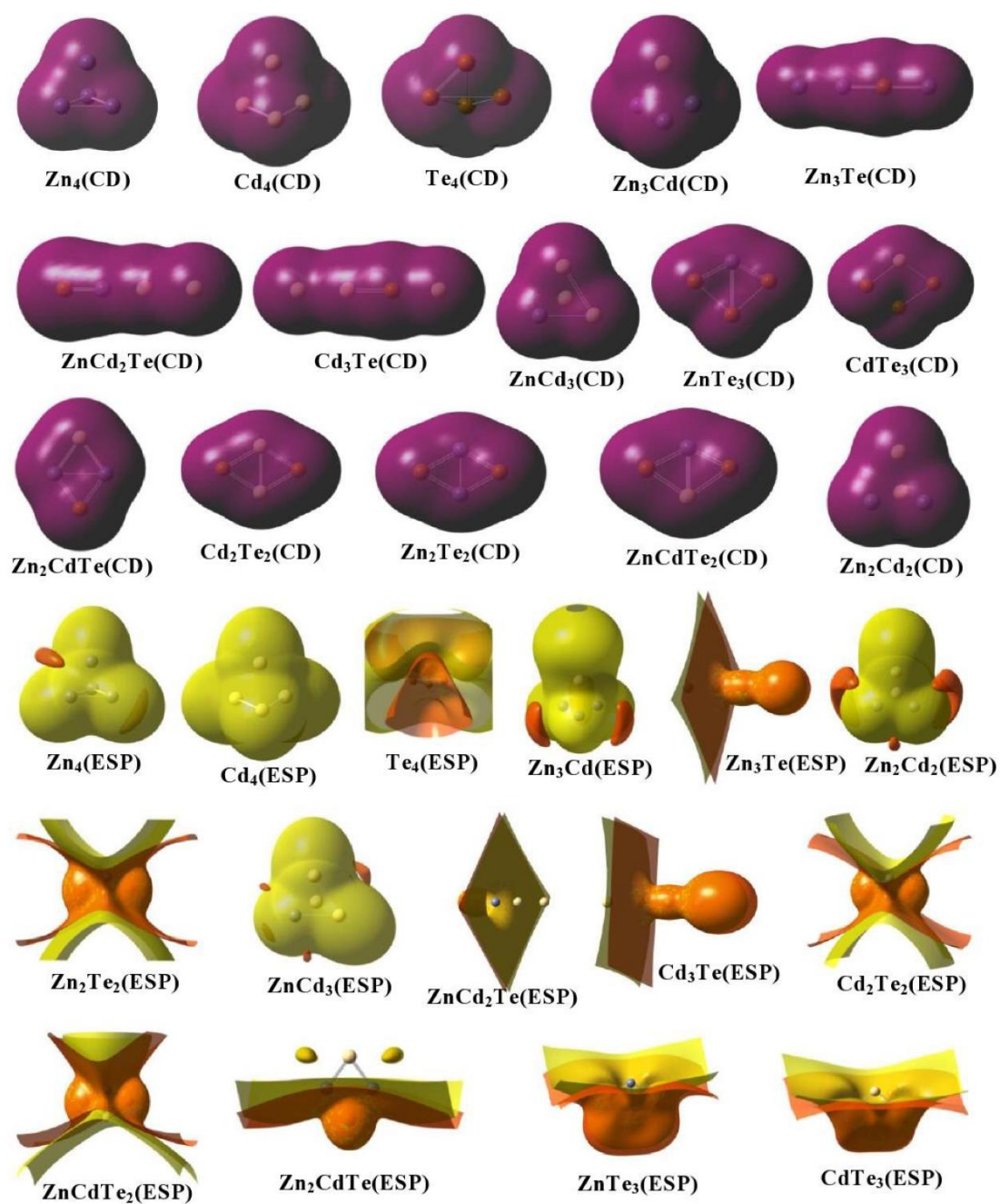


Figure 36. Charge density (CD) and electrostatic potential (ESP) pictures of trimers.

Table 7. The binding (E_b , in eV) and total (E_T , in Hartree) energies, the multiplicities of the spin system ($2S+1$), and the dipole moments (μ , in Debyes) for tetramer structures with the lowest energy. The corresponding total energies for the triplet states are given in the parenthesis.

Tetramers	Geometry	E_b	E_T	$2S + 1$	μ
Zn ₄	Tetrahedral	0.067	-904.519(-904.438)	1(3)	0.00
Cd ₄	Tetrahedral	0.069	-667.756(-667.671)	1(3)	0.00
Te ₄	Tetrahedral	9.592	-32.258(-32.184)	1(3)	0.93
Zn ₃ Cd	Tetrahedral	0.231	-845.328(-845.257)	1(3)	0.12
Zn ₃ Te	Linear	2.585	-686.451(-686.445)	1(3)	4.25
Zn ₂ Cd ₂	Tetrahedral	0.057	-786.137(-786.132)	1(3)	0.00
Zn ₂ Te ₂	Rhombus	1.999	-468.455(-468.404)	1(3)	0.00
ZnCd ₃	Tetrahedral	0.012	-726.946(-726.942)	1(3)	0.20
ZnTe ₃	Rhombus	1.379	-250.363(-250.341)	1(3)	2.09
Cd ₃ Te	Linear	2.391	-508.875(-508.856)	1(3)	4.16
Cd ₂ Te ₂	Rhombus	1.252	-350.049(-350.009)	1(3)	0.00
CdTe ₃	Rhombus	0.919	-191.157(-191.156)	1(3)	2.96
Zn ₂ CdTe	Rhombus	2.649	-627.261(-627.255)	1(3)	3.53
ZnCd ₂ Te	Linear	2.548	-568.069(-568.050)	1(3)	11.7
ZnCdTe ₂	Rhombus	1.635	-409.252 (-409.220)	1(3)	1.14

Table 8. Calculated vibration harmonic frequencies (in cm^{-1}) of all the tetramer structures with the lowest energy of $\text{Zn}_m\text{Cd}_n\text{Te}_k$ clusters for $m+n+k=4$. Zn_3Te , Cd_3Te and ZnCdTe_2 have one more frequency value 223.0, 163.5 and 285.5, respectively.

Tetramers	Vibration frequencies					
	ω_1	ω_2	ω_3	ω_4	ω_5	ω_6
Zn_4	5.3	7.7	7.8	20.0	43.7	47.7
Cd_4	0.3	8.7	9.0	13.6	15.4	28.0
Te_4	43.6	52.6	94.0	122.6	178.2	209.1
Zn_3Cd	56.3	57.3	58.5	73.5	74.2	80.8
Zn_3Te	10.5	10.5	36.7	36.7	84.4	110.0
Zn_2Cd_2	0.1	6.7	9.6	18.6	26.6	29.4
Zn_2Te_2	70.9	131.4	136.4	182.8	213.0	255.3
ZnCd_3	0.8	6.6	6.9	10.1	13.9	15.9
ZnTe_3	23.8	88.8	141.0	142.1	186.8	265.1
Cd_3Te	9.3	9.3	28.3	28.3	59.9	98.5
Cd_2Te_2	52.5	102.9	108.4	131.8	165.8	192.1
CdTe_3	29.9	73.2	131.2	141.0	165.2	181.5
Zn_2CdTe	53.0	80.2	86.0	146.9	150.7	196.4
ZnCd_2Te	10.0	10.0	35.9	35.9	46.6	110.2
ZnCdTe_2	63.9	113.7	124.0	143.5	188.8	238.9

3.2 HOMO-LUMO gap energies (E_g)

The highest occupied molecular orbital (HOMO), the lowest unoccupied molecular orbital (LUMO) and the frontier molecular orbital energy gap (HOMO–LUMO difference in energy E_g) for all the clusters considered are given in Table 9. The energy gap E_g decreases with increasing size the cluster. The E_g of the clusters with Zn and Cd atoms are relatively larger than that of clusters with Te atom. The E_g of heteronuclear ZnCd dimer (4.76 eV) is larger than that of the heteronuclear ZnTe dimer (1.46 eV) and CdTe (1.52 eV). Interestingly, the element Te shows quite different features than that of Zn and Cd elements. HOMO and LUMO pictures of the dimer clusters are shown in Figure 37. In the case of $\text{Zn}_m\text{Cd}_n\text{Te}_k$ ($m+n+k=3$) three atom clusters, E_g of homonuclear Zn_3 and Cd_3 trimers are larger than that of homonuclear Te_3 trimers, same as the dimers. Similarly, E_g of the Te containing clusters are relatively smaller than that of trimers without Te. We have found E_g of heteronuclear ZnCdTe cluster to be 1.76 eV. This value changes from 1.5 eV to 2.3 eV in terms of stoichiometry [52]. HOMO and LUMO pictures of the trimer clusters are shown in Figure 37. For tetramers, E_g has the same properties as other clusters, dimers and trimers, but E_g decreases with increasing number of atoms. HOMO and LUMO pictures of the tetramer clusters are shown in Figure 38. From Figure 37 and Figure 38, HOMO and LUMO localizations in models with Te are mainly on and near the Te, whereas localization in the other models is almost symmetric over the structures. In addition, the clusters with spin multiplicity 3 have both α and β Molecular Orbital (MO) eigenvalues. It has been found that E_g of β states are comparatively smaller than that of α states on the outside of Te_2 dimer.

Table 9. HOMO, LUMO energies (in Hartree) and HOMO–LUMO gap energies (E_g , in eV) of $\text{Zn}_m\text{Cd}_n\text{Te}_k$ clusters for $m+n+k=4$. Entries with α and β correspond to $2S+1=3$, the rest correspond to $2S+1=1$.

Cluster	HOMO	LUMO	E_g	Cluster	HOMO	LUMO	E_g
Zn_2	-0.223	-0.041	4.952	Cd_2Te	-0.199	-0.138	1.165
Cd_2	-0.216	-0.045	4.652	ZnCdTe	-0.203	-0.138	1.768
Te_2 (α)	-0.231	-0.094	3.727	Zn_4	-0.224	-0.070	3.972
Te_2 (β)	-0.668	-0.151	14.07	Cd_4	-0.216	-0.068	3.999
ZnCd	-0.218	-0.043	4.761	Te_4	-0.209	-0.145	1.687
ZnTe	-0.210	-0.156	1.469	Zn_3Cd	-0.207	-0.066	3.754
$\text{CdTe}(\alpha)$	-0.207	-0.042	4.489	Zn_3Te	-0.196	-0.128	1.850
$\text{CdTe}(\beta)$	-0.208	-0.152	1.523	Zn_2Cd_2	-0.218	-0.069	4.054
Zn_3	-0.221	-0.058	4.435	Zn_2Te_2	-0.212	-0.120	2.503
Cd_3	-0.214	-0.056	4.299	ZnCd_3	-0.216	-0.068	4.027
Te_3	-0.218	-0.138	2.176	ZnTe_3	-0.205	-0.134	1.931
ZnCd_2	-0.173	-0.081	2.503	Cd_3Te	-0.189	-0.129	1.632
$\text{ZnTe}_2(\alpha)$	-0.253	-0.057	5.333	Cd_2Te_2	-0.208	-0.129	2.149
$\text{ZnTe}_2(\beta)$	-0.220	-0.181	1.061	CdTe_3	-0.203	-0.135	1.850
Zn_2Cd	-0.169	-0.084	2.312	Zn_2CdTe	-0.181	-0.125	1.523
Zn_2Te	-0.206	-0.137	1.877	ZnCd_2Te	-0.175	-0.132	1.170
$\text{CdTe}_2(\alpha)$	-0.216	-0.094	3.319	ZnCdTe_2	-0.210	-0.131	2.149
$\text{CdTe}_2(\beta)$	-0.227	0.149	2.122				

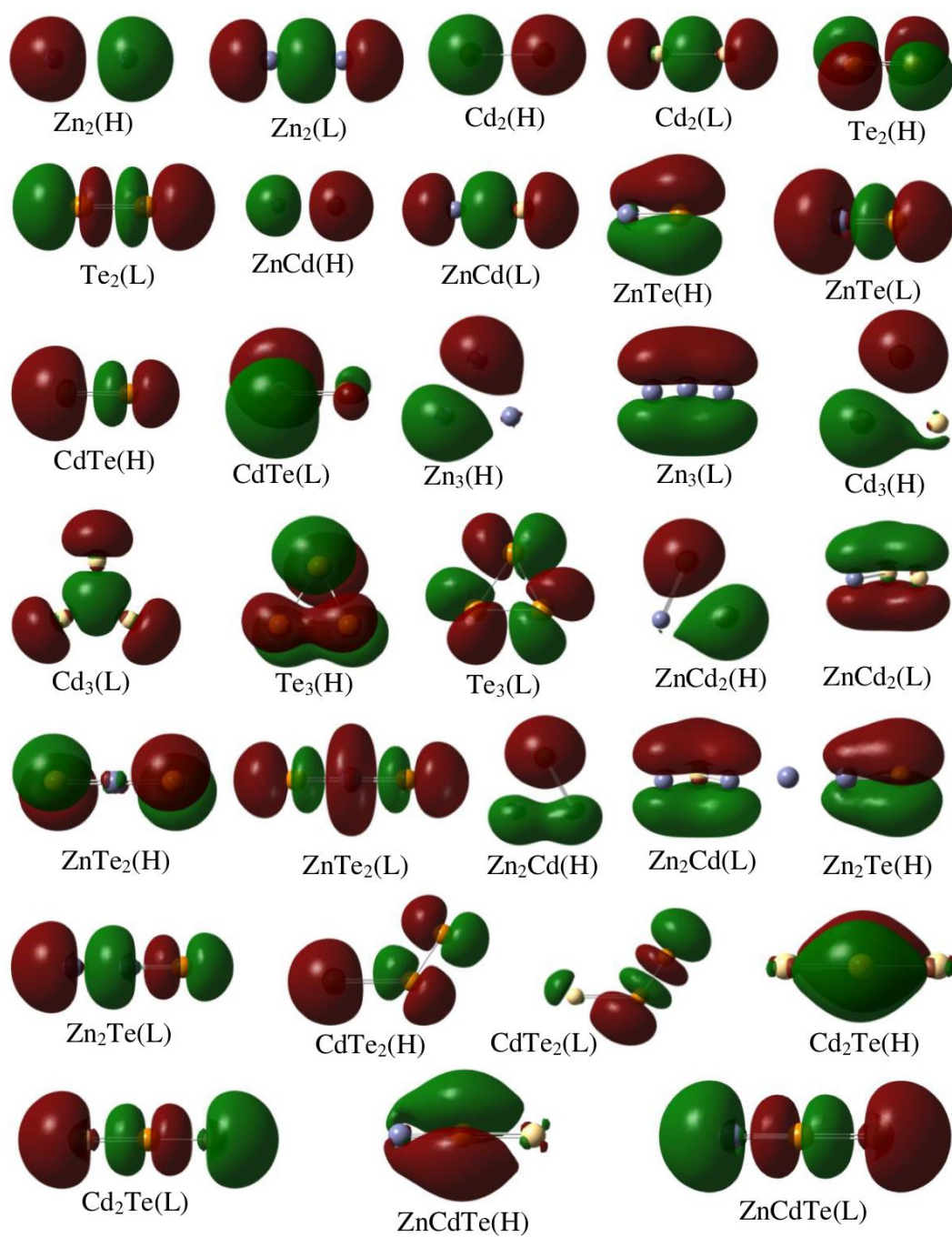


Figure 37. HOMO (H) and LUMO (L) pictures of dimers and trimers. Green and red colors represent the positive and negative isosurfaces for HOMO and LUMO, respectively.

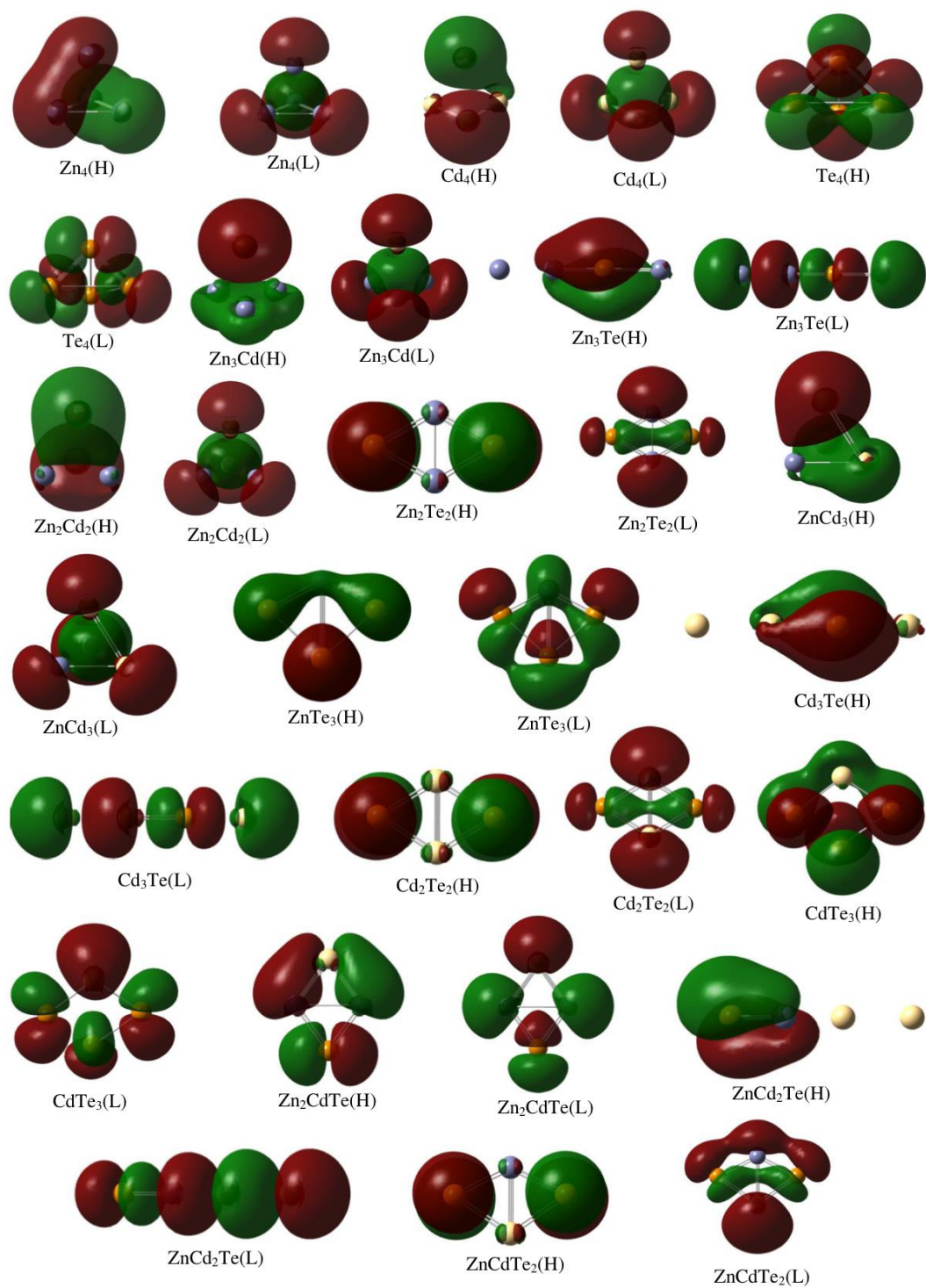


Figure 38. HOMO (H) and LUMO (L) pictures of tetramers. Green and red colors represent the positive and negative isosurfaces for HOMO and LUMO, respectively.

3.3. The dissociation channels and the corresponding dissociation energies

The results of possible dissociation channels (DCs) and the corresponding energies of the clusters considered are tabulated in Table 10. One of the dissociation channels of a trimer cluster may be defined by $ABC \rightarrow A + B + C$ and the corresponding dissociation channel energy ΔE_d for this particular case may be expressed as $\Delta E_d = E(ABC) - E(A) - E(B) - E(C)$. Similarly, it may be defined for the dissociation $ABC \rightarrow AB + C$ as $\Delta E_d = E(ABC) - E(AB) - E(C)$ or for the dissociation $ABC \rightarrow A + BC$ it is $\Delta E_d = E(ABC) - E(A) - E(BC)$. ΔE_d is known as the binding energy and it is always negative. The most probable DC represents maximum energy value, but minimum in magnitude. Homonuclear Zn, Cd and Te trimers choose the channel $A_3 \rightarrow A_2 + A$. Otherwise, Zn_2Cd , $ZnTe_2$, $CdTe_2$ and $ZnCd_2$, Cd_2Te , Zn_2Te type binary trimers prefer the dissociation channel $A_2B \rightarrow A_2 + B$ and $A_2B \rightarrow AB + A$. Moreover, homonuclear Zn_4 , Cd_4 and Te_4 tetramers dissociate as $A_4 \rightarrow A_3 + A$ and $A_4 \rightarrow 2A_2$, respectively. The binary tetramers A_3B dissociate as either $A_3B \rightarrow A_2B + A$ or $A_3B \rightarrow A_3 + B$. On the other hand, for the binary tetramer A_2B_2 the most probable dissociation is $A_2B_2 \rightarrow A_2B + B$. It is interesting to note that in Cd containing models a single Cd atom dissociation looks more probable.

Table 10. Possible dissociation channels and energies (ΔE_d , in eV) of the stable $Zn_mCd_nTe_k$ clusters.

Cluster	DCs	ΔE_d	Cluster	DCs	ΔE_d
Zn_2	$\rightarrow 2Zn$	-0.012	Te_4	$\rightarrow 2Te_2$	-0.056
Cd_2	$\rightarrow 2Cd$	-0.007		$Te_3 + Te$	-2.679
Te_2	$\rightarrow 2Te$	-4.902		$Te_2 + 2Te$	-4.958
$ZnCd$	$\rightarrow Zn + Cd$	-0.010		$4Te$	-9.861
$ZnTe$	$\rightarrow Zn + Te$	-1.834	Zn_3Cd	$\rightarrow Zn_3 + Cd$	-0.231
$CdTe$	$\rightarrow Cd + Te$	-1.738		$Zn_2Cd + Zn$	-0.246
Zn_3	$\rightarrow Zn_2 + Zn$	-0.072		$Zn_2 + ZnCd$	-0.294
	$3Zn$	-0.086		$Zn_2 + Zn + Cd$	-0.304
Cd_3	$\rightarrow Cd_2 + Cd$	-0.038		$ZnCd + 2Zn$	-0.306
	$3Cd$	-0.047		$3Zn + Cd$	-0.317
Te_3	$\rightarrow Te_2 + Te$	-2.279	Zn_3Te	$\rightarrow Zn_2Te + Zn$	-0.279
	$3Te$	-7.182		$Zn_2 + ZnTe$	-0.824
$ZnCd_2$	$\rightarrow ZnCd + Cd$	-0.047		$ZnTe + 2Zn$	-0.837
	$Zn + Cd_2$	-0.050		$Zn_3 + Te$	-2.585
	$Zn + 2Cd$	-0.058		$Zn_2 + Zn + Cd$	-2.658
$ZnTe_2$	$\rightarrow Zn + Te_2$	-0.383		$3Zn + Te$	-2.671
	$ZnTe + Te$	-3.451	Zn_2Cd_2	$\rightarrow Zn_2Cd + Cd$	-0.194
	$Zn + 2Te$	-5.285		$ZnCd_2 + Zn$	-0.207
Zn_2Cd	$\rightarrow Zn_2 + Cd$	-0.058		$Zn_2 + Cd_2$	-0.244
	$2Zn + Cd$	-0.074		$2ZnCd$	-0.244
	$ZnCd + Zn$	-0.876		$Zn_2 + 2Cd$	-0.252
Zn_2Te	$\rightarrow ZnTe + Zn$	-0.558		$ZnCd + Zn + Cd$	-0.254
	$Zn_2 + Te$	-2.379		$2Zn + Cd_2$	-0.254
	$2Zn + Te$	-2.392		$2Zn + 2Cd$	-0.264
$CdTe_2$	$\rightarrow Cd + Te_2$	-0.016	Zn_2Te_2	$\rightarrow ZnTe_2 + Zn$	-1.629
	$CdTe + Te$	-3.180		$Zn_2 + Te_2$	-1.999
	$Cd + 2Te$	-4.918		$2Zn + Te_2$	-2.012
Cd_2Te	$\rightarrow CdTe + Cd$	-0.465		$2ZnTe$	-3.246
	$Cd_2 + Te$	-2.196		$Zn_2Te + Te$	-4.522
	$2Cd + Te$	-2.204		$ZnTe + Zn + Te$	-5.080
$ZnCdTe$	$\rightarrow ZnTe + Cd$	-0.462		$Zn_2 + 2Te$	-6.901
	$Zn + CdTe$	-0.558		$2Zn + 2Te$	-6.914
	$ZnCd + Te$	-2.286	$ZnCd_3$	$\rightarrow ZnCd_2 + Cd$	-0.165
	$Zn + Cd + Te$	-2.296		$Cd_3 + Zn$	-0.175
Zn_4	$\rightarrow Zn_3 + Zn$	-0.296		$Cd_2 + ZnCd$	-0.205
	$2Zn_2$	-0.356		$ZnCd + 2Cd$	-0.212
	$Zn_2 + 2Zn$	-0.369		$Cd_2 + Zn + Cd$	-0.215
	$4Zn$	-0.381		$3Cd + Zn$	-0.223
Cd_4	$\rightarrow Cd_3 + Cd$	-0.142			
	$2Cd_2$	-0.173			
	$Cd_2 + 2Cd$	-0.181			
	$4Cd$	-0.189			

Table 10. (Continued).

Cluster	DCs	ΔE_d	Cluster	DCs	ΔE_d
ZnTe ₃	→ Te ₃ + Zn	-1.379	Zn ₂ CdTe	→ Zn ₂ Te + Cd	-0.269
	Te ₂ + ZnTe	-1.824		ZnCdTe + Zn	-0.365
	ZnTe ₂ + Te	-3.275		ZnCd + ZnTe	-0.817
	Te ₂ + Zn + Te	-3.659		ZnTe + Zn + Cd	-0.828
	ZnTe + 2Te	-6.727		Zn ₂ + CdTe	-0.902
	3Te + Zn	-8.561		CdTe + 2Zn	-0.923
Cd ₃ Te	→ Cd ₂ Te + Cd	-0.234	ZnCd ₂ Te	→ ZnCdTe + Cd	-0.259
	Cd ₂ + CdTe	-0.697		Cd ₂ Te + Zn	-0.351
	CdTe + 2Cd	-0.700		ZnTe + Cd ₂	-0.714
	Cd ₃ + Te	-2.391		ZnTe + 2Cd	-0.721
	Cd ₂ + Cd + Te	-2.431		ZnCd + CdTe	-0.807
	3Cd + Te	-2.439		CdTe + Zn + Cd	-0.817
Cd ₂ Te ₂	→ CdTe ₂ + Cd	-1.243	ZnCdTe ₂	→ ZnTe ₂ + Cd	-1.251
	Cd ₂ + Te ₂	-1.252		CdTe ₂ + Zn	-1.619
	2Cd + Te ₂	-1.260		ZnCd + Te ₂	-1.625
	2CdTe	-2.685		Te ₂ + Zn + Cd	-1.635
	Cd ₂ Te + Te	-3.958		ZnTe + CdTe	-2.965
	CdTe + Cd + Te	-4.423		ZnCdTe + Te	-4.241
	Cd ₂ + 2Te	-6.154		ZnTe + Cd + Te	-4.703
	2Cd + 2Te	-6.162		CdTe + Zn + Te	-4.798
CdTe ₃	→ Te ₃ + Cd	-0.919		ZnCd + 2Te	-6.527
	Te ₂ + CdTe	-1.460		Zn + Cd + 2Te	-6.538
	CdTe ₂ + Te	-3.182			
	Te ₂ + Cd + Te	-3.199			
	CdTe + 2Te	-6.362			
	3Te + Cd	-8.101			

3.5 Structural, Electronic and Thermal Properties of AB₆C₈ Ternary CdZnTe Cubic Nanoparticles: MD Simulations and DFT Calculations

3.5.1 Introduction

The geometrical and electronic properties of isolated CdZnTe ternary alloy nanoparticles have been studied by MD simulations and DFT calculations. The general composition of a 15-atom ternary nanoparticle is formed as AB₆C₈. The initial structure was modeled as a perfect cube with A at the center, B's at the surface centers, and C's at the corners of the cube. The heat capacity calculation is performed in the range of 100-600 K using the non-equilibrated molecular dynamics method. In addition, a parameter δ is calculated with respect to the coordinate center of the system to categorize the considered structures in point of their morphology. Besides, the segregation phenomena of Cd, Zn, and Te atoms in nanoparticles are searched by the order parameter R . Using optimized geometries obtained from molecular dynamics simulations, excess charge on atoms, dipole moments, HOMO, LUMO, HOMO-LUMO gaps (E_g), total energies, charge density, spin density, electrostatic potential have been investigated by means of DFT. The densities of states have also been calculated for all CdZnTe compounds.

3.5.2 Modelling and Calculation Procedure

In this section, we present atomistic molecular-dynamics (MD) simulations and density functional theory calculations of various CdZnTe nanoparticles. Firstly, the MD application the optimized models were obtained at 1 K, 300 K and 600 K. We then investigate the variation of the potential energy and the composition dependence of heat capacity, and the influence of the concentration of Cd, Zn and Te atoms on the heat capacity C_v with a fixed total number of atoms. Considering the optimized

structures the variation of the order parameter R during heating process is calculated to understand the character of the stable structures and analyze segregation phenomena of Zn, Cd, and Te in the CdZnTe nanostructures, and finally δ which reflect the deflection from spherical shape is calculated to categorize the considered models in terms of their morphology. In the final stage of the investigation density functional theory (DFT) has been applied to the MD-optimized structures at 1 K. In the DFT applications with B3LYP/CEP-121G, the electronic properties have been calculated for the considered models. Moreover, the details of the basis set used are given in Table 11. GAUSSIAN09 program package has been used in the calculations.

Table 11. Basis set data used in DFT calculations.

Model	# of basis function	# of primitive gaussians	# of cartesian basis functions	# of α electrons	# of β electrons
Cd ₆ Zn ₁ Te ₈	302	600	302	96	92
Cd ₈ Zn ₁ Te ₆	354	684	354	109	107
Cd ₁ Zn ₆ Te ₈	302	630	302	94	94
Cd ₈ Zn ₆ Te ₁	484	924	484	143	143
Cd ₁ Zn ₈ Te ₆	354	726	354	109	107
Cd ₆ Zn ₈ Te ₁	484	936	384	143	143

All MD simulations of the cubic nanoparticles have been studied via LAMMPS using Cd-Zn-Te ternary analytical BOP. The initial and different views of the optimized structures of the CdZnTe models are shown in Figure 39.

Nosé-Hoover thermostat and the canonical ensemble (NVT) are used to control thermal equilibrium during the whole simulations. In the computations, the heating procedure is applied, where the temperature was raised by 50K. The simulations were implemented by starting at 1K, and then temperature is increased up to 600 K for CdZnTe cubic nanoparticles. In all the simulations, each run is composed of 50000 MD steps (50 ps). During the heating process the non-equilibrated MD method was used. In this method, the system's temperature was gradually increased by 50K without waiting for the system to reach the equilibrium state. Boltzmann velocity distribution was utilized to generate particle velocities at the corresponding temperature. The cut-off radius of 14.70 Å was used for maximum interaction range.

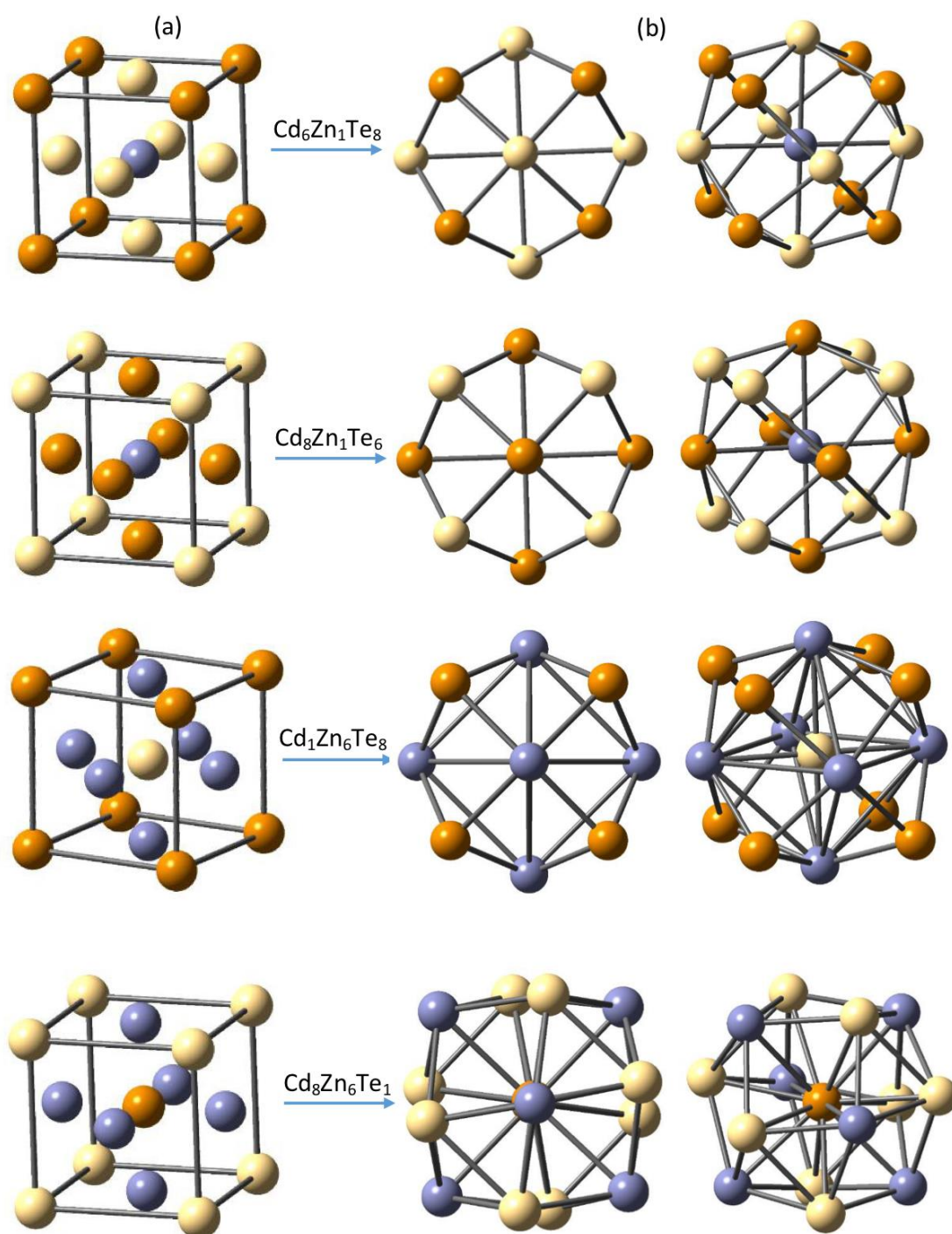


Figure 39. (a) Initial structures and (b) optimized geometries with two different views of the various CdZnTe nanostructures with 15 atoms (Zn is purple, Cd is grey and Te is orange).

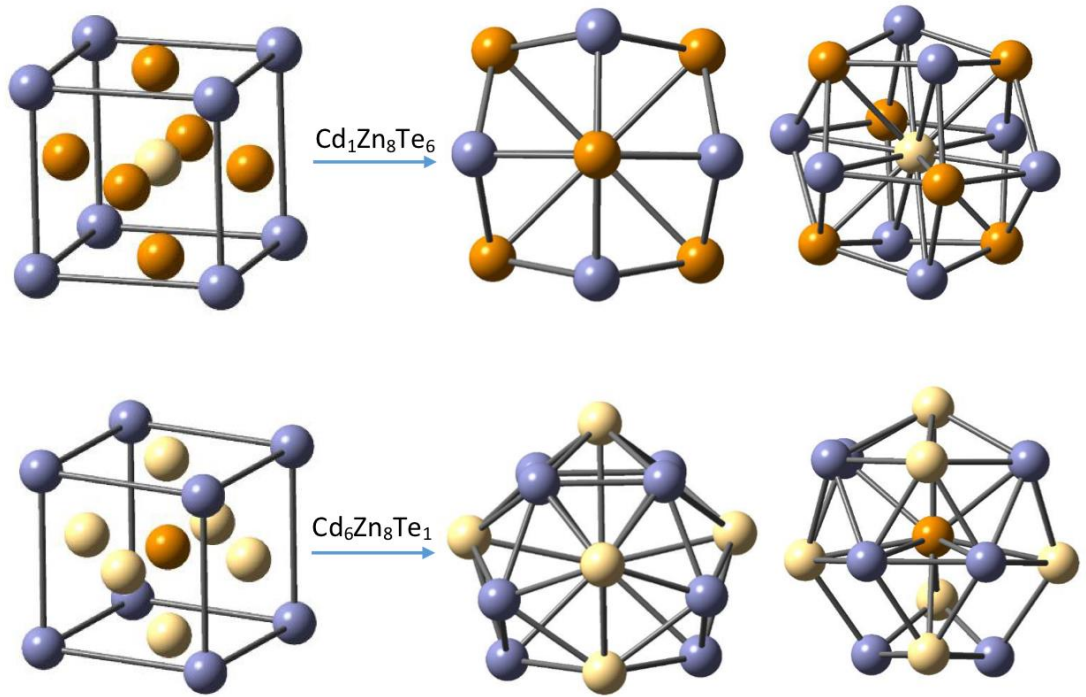


Figure 39. (Continued).

3.5.3 Results and Discussions

In the first part of this section we will discuss the MD simulation results to figure out some physical properties of the different compositions of the CdZnTe cubic nanoparticles. For this purpose, we have presented some results such as the deviation of morphology of the nanoparticles from a perfectly cubic structure, order parameter and heat capacity. Firstly, we have increased the temperature from 1 K to 600 K to see the structural variation of the CdZnTe nanoparticles from cube structure. As a sample model, Figure 40 represents the structure of the $\text{Zn}_1\text{Cd}_6\text{Te}_8$ nanoparticle at various temperatures. It is apparent from the figure that it shows the increment of the deformations in the nanoparticle structure when the temperature increases. As shown in Figure 40, the deformation in the structure of the nanoparticle increases as the temperature increases, as expected.

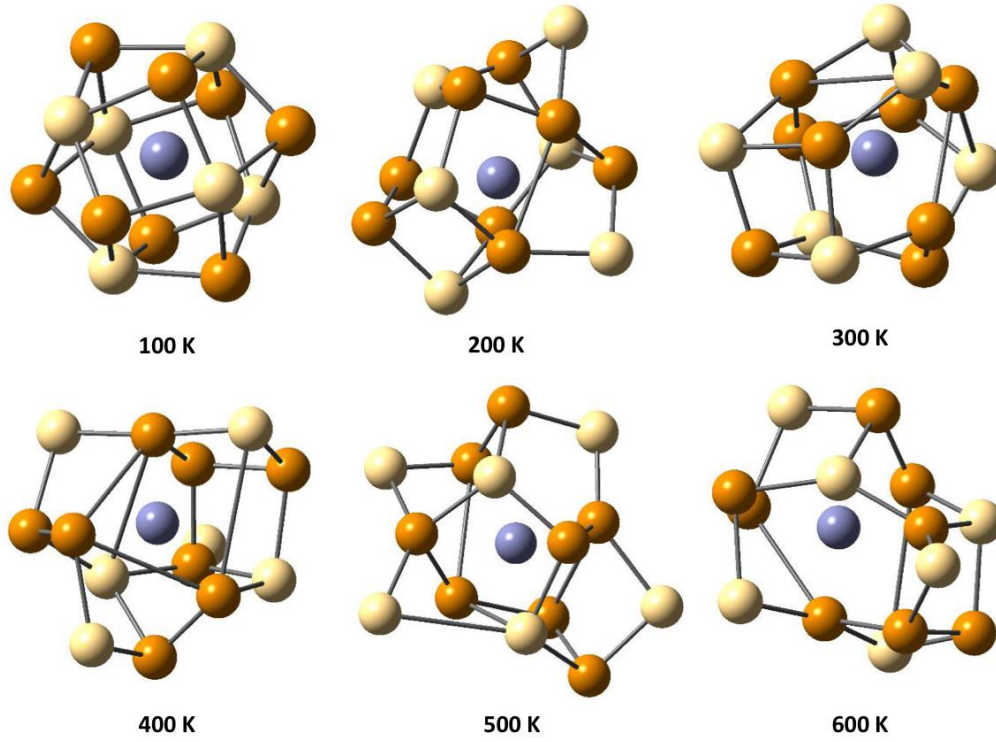


Figure 40. The change in the structures of the $\text{Zn}_1\text{Cd}_6\text{Te}_8$ nanoparticle at various temperatures.

Considering the optimized structures the variation of a parameter δ is calculated to classify the studied models in terms of their morphology. The parameter δ by definition from a perfect spherical structure, is described as follows [133]:

$$\delta = \sqrt{\frac{1}{N} \sum_{i=1}^N r_i^2} \quad (3.2)$$

where r_i are the distances of the atoms to the coordinate center of the nanoparticle. The δ values for all the structures at 1 K, 300 K and 600 K are tabulated in Table 12. The average distance of Cd, Zn and Te atoms are given in Table 13. The average distances are related with deviation δ .

Table 12. δ values (the deviation of morphology of the nanoparticles from a perfectly cubic structure)

Model	δ_i	δ_{1K}	δ_{300K}	δ_{600K}
Cd ₆ Zn ₁ Te ₈	3.19704	3.19790	4.18468	3.90431
Cd ₈ Zn ₁ Te ₆	3.21979	3.21908	3.71630	4.31204
Cd ₁ Zn ₆ Te ₈	3.00296	3.49957	4.16485	5.10851
Cd ₈ Zn ₆ Te ₁	2.94517	3.96405	3.91181	4.72308
Cd ₁ Zn ₈ Te ₆	2.97998	2.98136	5.15818	5.36536
Cd ₆ Zn ₈ Te ₁	2.89743	3.01371	3.08984	4.14786

Table 13. Average distances of Cd, Zn and Te atoms.

Model	\bar{d}_{Zn-Cd}	\bar{d}_{Zn-Te}	\bar{d}_{Cd-Te}
Cd ₆ Zn ₁ Te ₈	3.076	3.474	3.032
Cd ₈ Zn ₁ Te ₆	3.002	3.559	3.055
Cd ₁ Zn ₆ Te ₈	3.630	3.312	3.534
Cd ₈ Zn ₆ Te ₁	2.846	3.056	3.075
Cd ₁ Zn ₈ Te ₆	3.120	2.832	3.039
Cd ₆ Zn ₈ Te ₁	2.786	3.124	3.103

The distribution of atoms in crystalline systems are usually uniform and homogeneous. However, in nanoparticles this pattern may not be conserved, particularly at high temperatures. Solidification problems such as segregation are encountered during the growth of CdZnTe at high temperature which results in non-uniformity in the stoichiometry [19]. Thus, the behavior of the optimized structures in various CdZnTe

ternary nanoparticles is researched by means of the order parameter (R_A), which is analyzed by the mean distance of a type A atoms with respect to the nanoparticle center [134],

$$R_A = \frac{1}{n_A} \sum_{i=1}^{n_A} r_i \quad (3.3)$$

where n_A displays the count of type A atoms in the ternary ABC nanoparticles, and r_i are the distances of the atoms to the coordinate center of the nanoparticle. The calculated R_A values represent the atomic mixing degree in ternary nanoparticles. If the (R_A) has a large value, this means A atoms are located at the central part or at the surface region of the nanoparticle. On the other hand, if the R_A has a small value, this means the atoms are located at the center of the nanoparticle.

Figure 41 demonstrates the order parameter-the nanoparticle models at (a) 1 K and (b) 300 K. From Figure 41 (a), it is seen that the central atom of all the models, except $\text{Cd}_8\text{Zn}_6\text{Te}_1$, keep their position almost at the center, the central atom of the $\text{Cd}_8\text{Zn}_6\text{Te}_1$ deviates a little bit from the central position. Almost in all models the non-central atoms locate near the central atom forming a shell structure, a sort of cage structure. Nevertheless, at 300 K, as seen in Figure 41 (b), the central atoms cannot keep their position at the center of coordinate, they slightly move away from the center, the other atoms locate about the central atom forming a shell structure, but in this case the shell form is not as regular as at 1 K. Interestingly, in the $\text{Cd}_1\text{Zn}_8\text{Te}_6$ model the central atom Cd moves to the shell region, no atom appears at the center. The tendency of the atoms in the nanoparticle models to the surface due to lower surface and cohesive energy of Cd, Zn and Te atoms. Considering all the models, we conclude that the alteration of the R_A shows a characteristic for certain models, for instance, in the $\text{Cd}_8\text{Zn}_1\text{Te}_6$ model, Cd atoms locate with largest R value at both 1 K and 300 K.

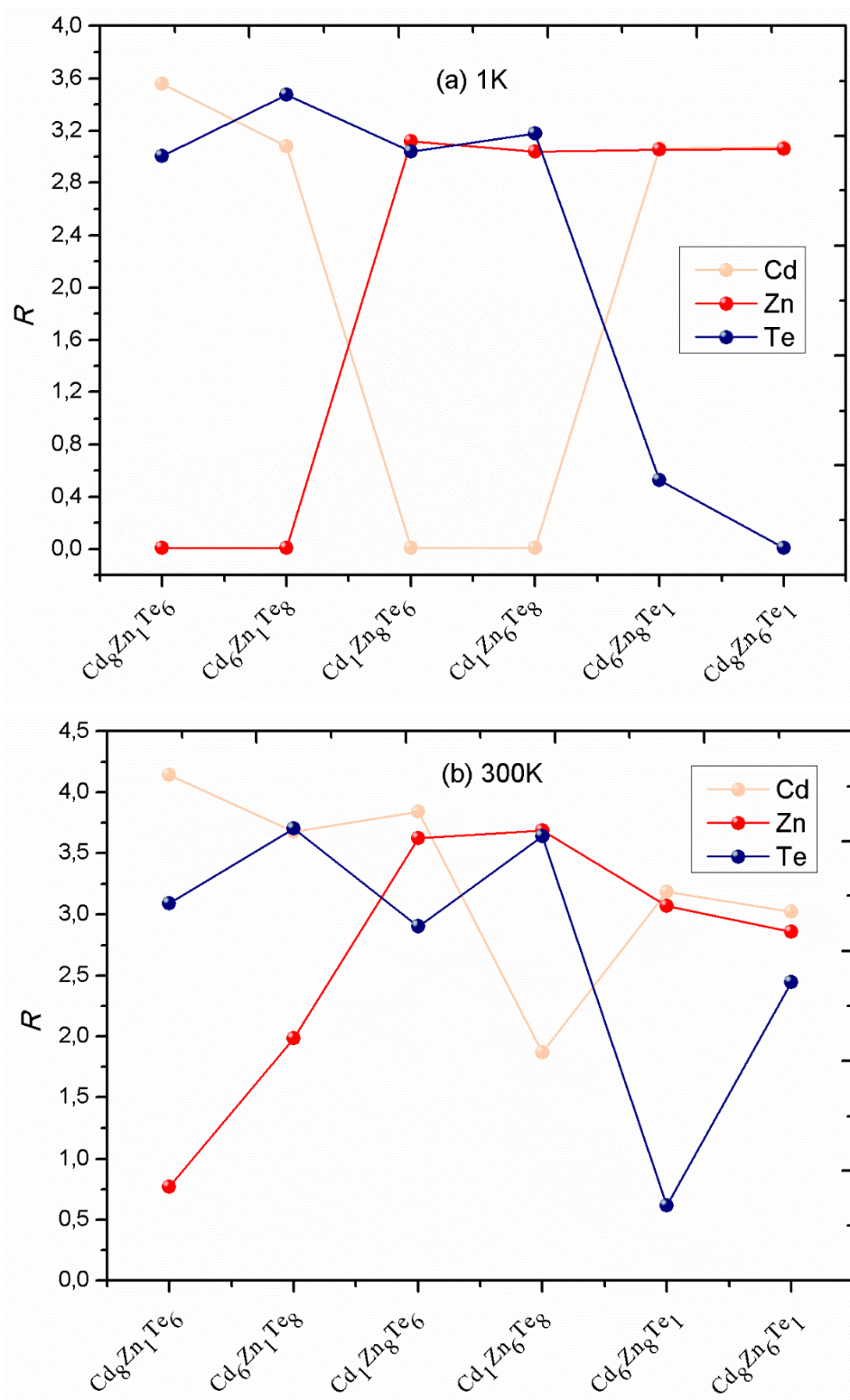


Figure 41. Variation of the order parameter R_{Cd} , R_{Zn} , and R_{Te} with various CdZnTe compounds at (a) 1 K and (b) 300 K.

Variation of potential energy as a function of temperature for various CdZnTe compounds is depicted in Figure 42. According to the data given in Figure 42 the variation of average energy per atom values show almost a smooth increase with temperature in the range 100-600 K. The least-square linear fit of the data points are also displayed in Figure 42.

The heat capacity is used for the calculation of many thermodynamic quantities, such as changes in enthalpy, internal energy and entropy. In this study, the heat capacity is related to that part of the internal energy, namely the interaction potential energy. One of the aim of this study is to research the effect of composition on behavior of the heat capacity using a molecular dynamics simulation. The specific heat capacity is formally expressed as the rate of internal energy in terms of temperature:

$$C_v = \left(\frac{\partial E}{\partial T} \right)_v \quad (3.4)$$

The heat capacity values for bulk materials of almost all types are available in the literature. However, for nanoparticles it is very limited and the available data for certain nanomaterials were obtained by simulations [135]. For the CdZnTe ternary cubic nanoparticles heat capacity values have been calculated for the first time by performing MD simulations. The heat capacity values are calculated from the slope of the best fitted lines.

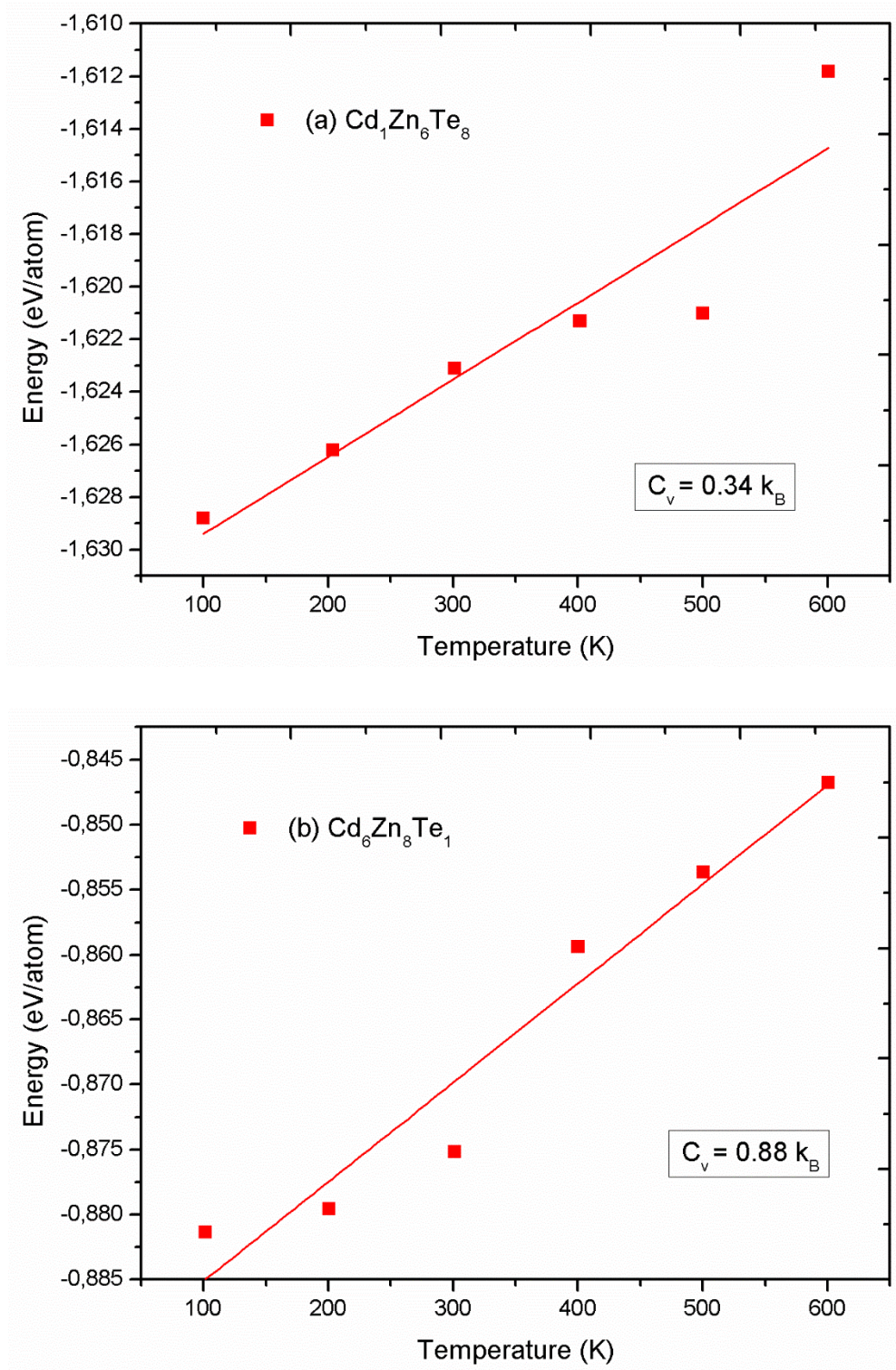


Figure 42. Energy variation with temperature in terms of the composition of nanoparticles (a)-(f) with corresponding calculated heat capacity values C_v .

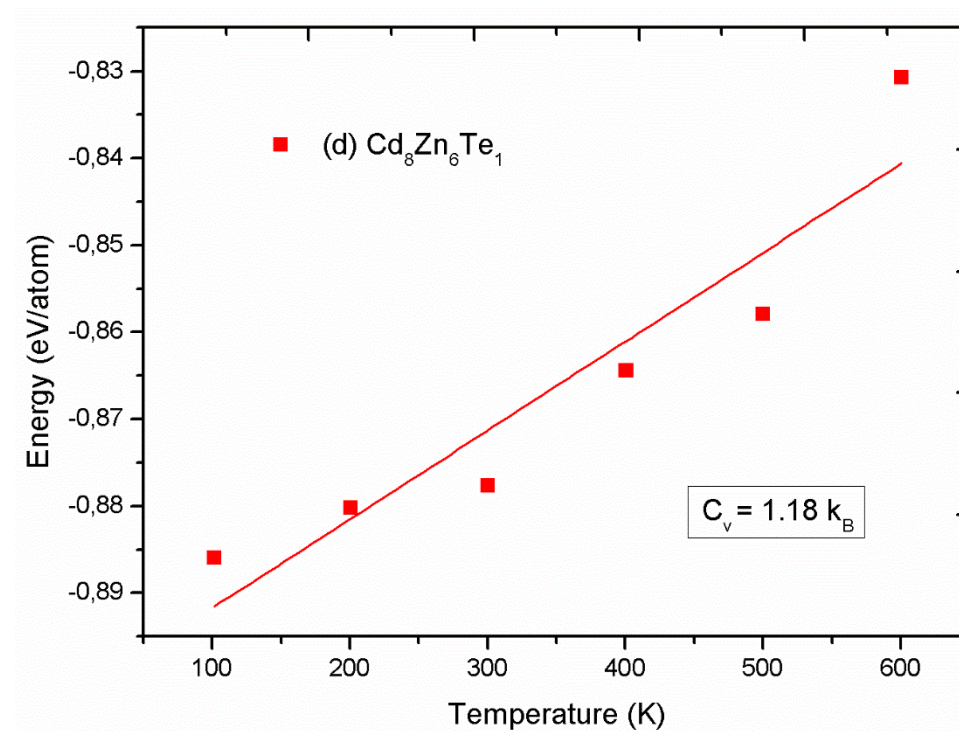
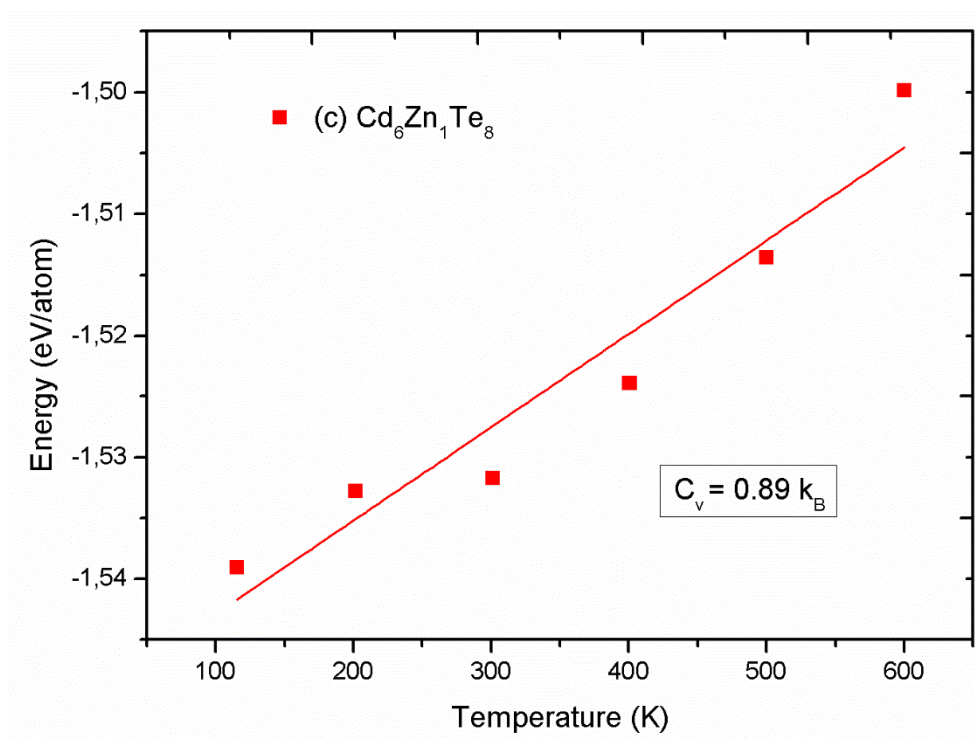


Figure 42. (Continued).

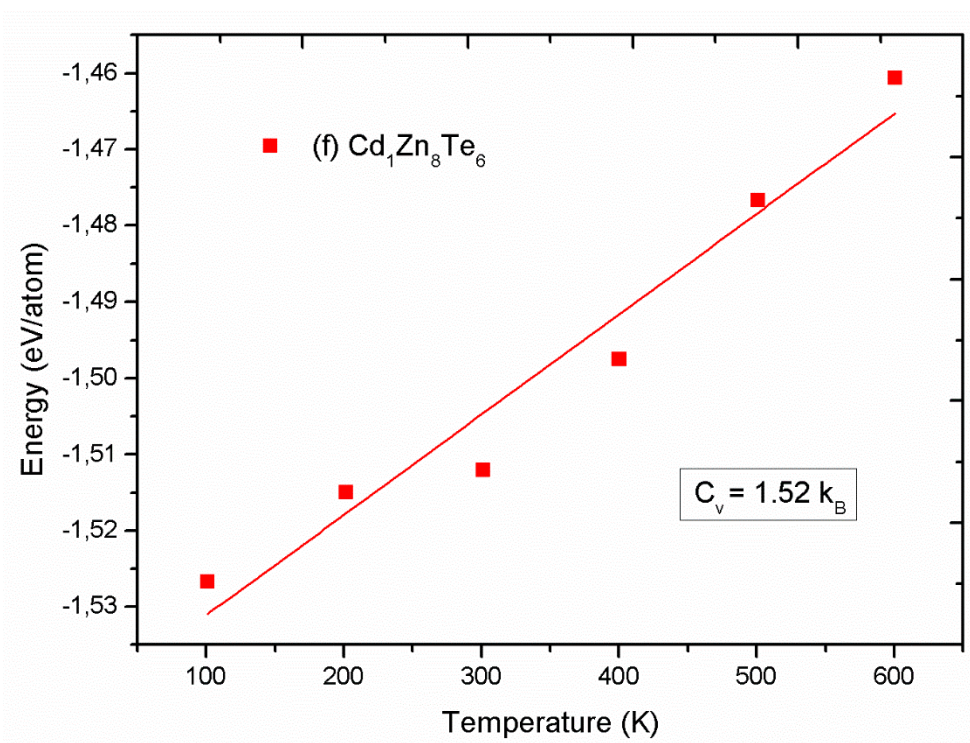
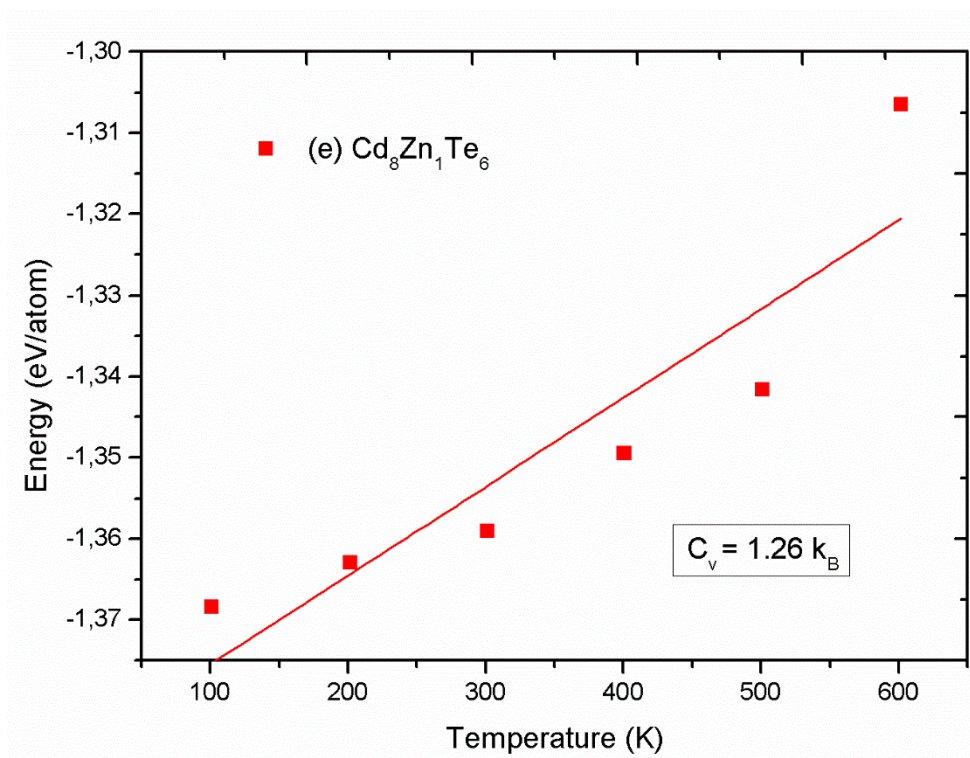


Figure 42. (Continued).

The variation of the heat capacity C_v for various cubic CdZnTe nanoparticles up to 600 K is shown in Figure 43. As it can be seen, the concentration of cadmium, zinc and tellurium has significant influence on the heat capacity behavior. $\text{Cd}_{1-x}\text{Zn}_x\text{Te}$ alloys show different values with increasing the Zn and Cd concentration for heat capacity [136]. Although there is no thermal data in the literature for the CdZnTe nanoparticles, we may compare the trend of the present results for nanoparticles with that of bulk values. In this sense the present results show similar behavior as seen in the bulk [136]. The variation of the heat capacity indicates an increase in terms of the composition. It is interesting to note that $\text{Cd}_1\text{Zn}_6\text{Te}_8$ has minimum heat capacity value, whereas $\text{Cd}_1\text{Zn}_8\text{Te}_6$ has maximum heat capacity value. Zn and Te concentrations play a significant role in the heat capacity value; more Zn increases heat capacity, more Te decreases heat capacity. These values in the nanoparticles are consistent with the behavior of energy as a function of temperature as shown in Figure 42. From these results one can infer that the details of the evolution of heat capacity are strongly correlated with composition.

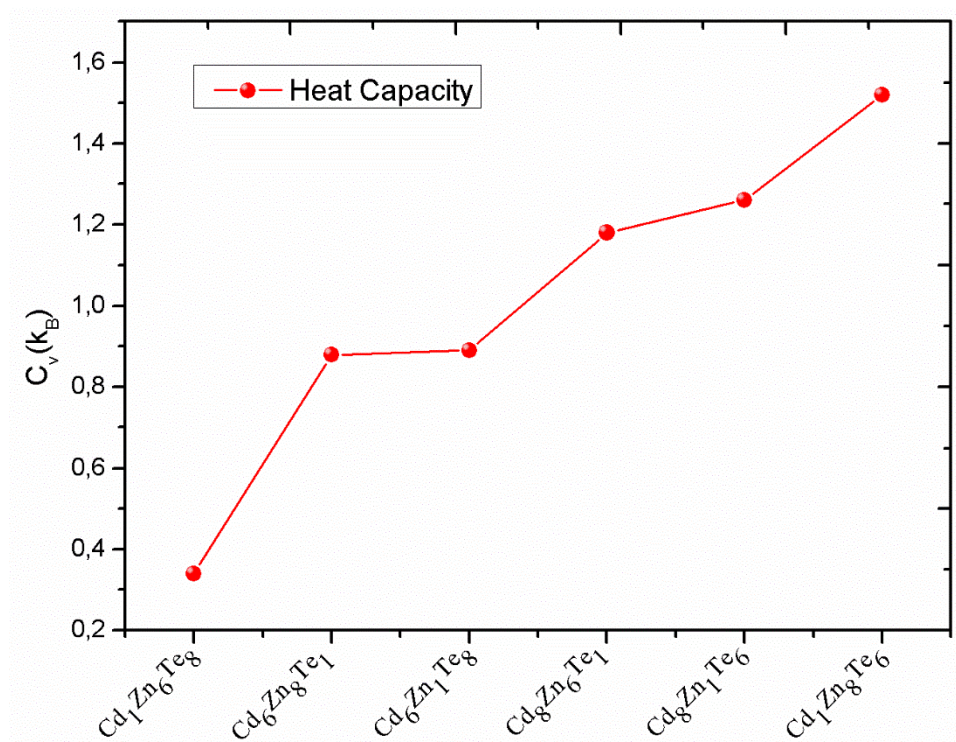


Figure 43. Composition dependence of the heat capacity values for various CdZnTe nanoparticles.

In the second part, we have used the optimized geometries obtained at 1 K from MD simulations and applied single point energy calculation by performing DFT method to understand the electronic properties such as total excess charge of each atom, dipole moments, HOMO and LUMO energies, HOMO–LUMO difference in energy, E_g , total energies, charge densities (CD), spin densities (SD), electrostatic potential (ESP) and density of states (DOS) of the different stoichiometry of the CdZnTe cubic nanoparticles.

HOMO and LUMO energies, HOMO–LUMO gap energies, total energy and the lowest energy multiplicities ($2S+1$) of the spin system for various CdZnTe compounds are given in Table 14. The electronic ground state has been found to be spin multiplicity 5 for $Cd_6Zn_1Te_6$ nanoparticle and spin multiplicity 3 for the $Cd_8Zn_1Te_6$ and $Cd_1Zn_8Te_6$ nanoparticles, and the rest have been found to have a spin singlet state with multiplicity 1. The nanoparticles with spin multiplicity 3 and 5 have both alpha

and beta Molecular Orbital (MO) eigenvalues. The energy gap between HOMO and LUMO, known as HOMO-LUMO gap, is an important parameter to determine the electrical transport properties of the nanoparticles, as well as the optical properties. It has been found that E_g of β states are comparatively larger than that of α states for spin multiplicity 3 and E_g of β states are comparatively smaller than that of α states for spin multiplicity 5. The gap energy of the $\text{Cd}_1\text{Zn}_8\text{Te}_6$ (β) ternary nanoparticle (2.340 eV) is larger than that of the other CdZnTe ternary nanoparticles. We can also see that its value has a minimum for the $\text{Cd}_8\text{Zn}_1\text{Te}_6$ (α) nanoparticle (0.598 eV). The smaller gap corresponds to high chemical reactivity and kinetic stability. As it may be seen from Table 14, the energy gap (E_g) increases as the number of Cd and Zn atoms in the nanoparticles (with spin multiplicity 1) increases when the number of Te atoms is to be constant. This increment is compatible with the conclusions of E_g of elemental Zn and Cd clusters which are relatively larger than that of the elemental Te clusters.

Table 14. HOMO, LUMO energies (in a.u.), HOMO–LUMO gap energies (E_g), total energy (E_T in Hartree) and the lowest energy multiplicities (2S+1) of the spin system for various CdZnTe compounds.

Model	HOMO	LUMO	E_g (eV)	E_T	2S+1
$\text{Cd}_6\text{Zn}_1\text{Te}_8$ (α)	-0.202	-0.134	1.850	-1292.421	5
$\text{Cd}_6\text{Zn}_1\text{Te}_8$ (β)	-0.195	-0.169	0.789		
$\text{Cd}_8\text{Zn}_1\text{Te}_6$ (α)	-0.155	-0.133	0.598	-1610.189	3
$\text{Cd}_8\text{Zn}_1\text{Te}_6$ (β)	-0.201	-0.126	2.040		
$\text{Cd}_1\text{Zn}_6\text{Te}_8$	-0.191	-0.155	0.979	-1588.421	1
$\text{Cd}_8\text{Zn}_6\text{Te}_1$	-0.180	-0.140	1.088	-2700.275	1
$\text{Cd}_1\text{Zn}_8\text{Te}_6$ (α)	-0.150	-0.125	0.680	-2024.567	3
$\text{Cd}_1\text{Zn}_8\text{Te}_6$ (β)	-0.207	-0.121	2.340		
$\text{Cd}_6\text{Zn}_8\text{Te}_1$	-0.166	-0.134	0.870	-2818.675	1

The Mulliken atomic charges show a significant role applications in quantum chemistry. The calculated excess charges of atoms in each model are shown in Figure 44. The total Mulliken charges of the CdZnTe nanoparticles were gathered in Table 15. The charges of the atoms in different models indicate dissimilar charge with each other. For instance, the total excess charge of Zn atom is negative in the Cd₆Zn₁Te₆ nanoparticle, on the other hand, the total excess charge of Zn atom is positive in the Cd₈Zn₆Te₁ nanoparticle. We can infer that the composition of the nanoparticle strongly effects the value of the Mulliken charge on the atoms. The dipole moments are other important electronic properties. The bigger the dipole moment represents the stronger intermolecular interaction. Dipole moment along the x-axis ($\mu_x=0.235$, Debye) was found to be the highest value which corresponds to large opposite charge separation in the Cd₈Zn₁Te₆ nanoparticle. The corresponding total dipole moment was found to be 0.290 Debye. Calculated dipole moment values are given in Table 15.

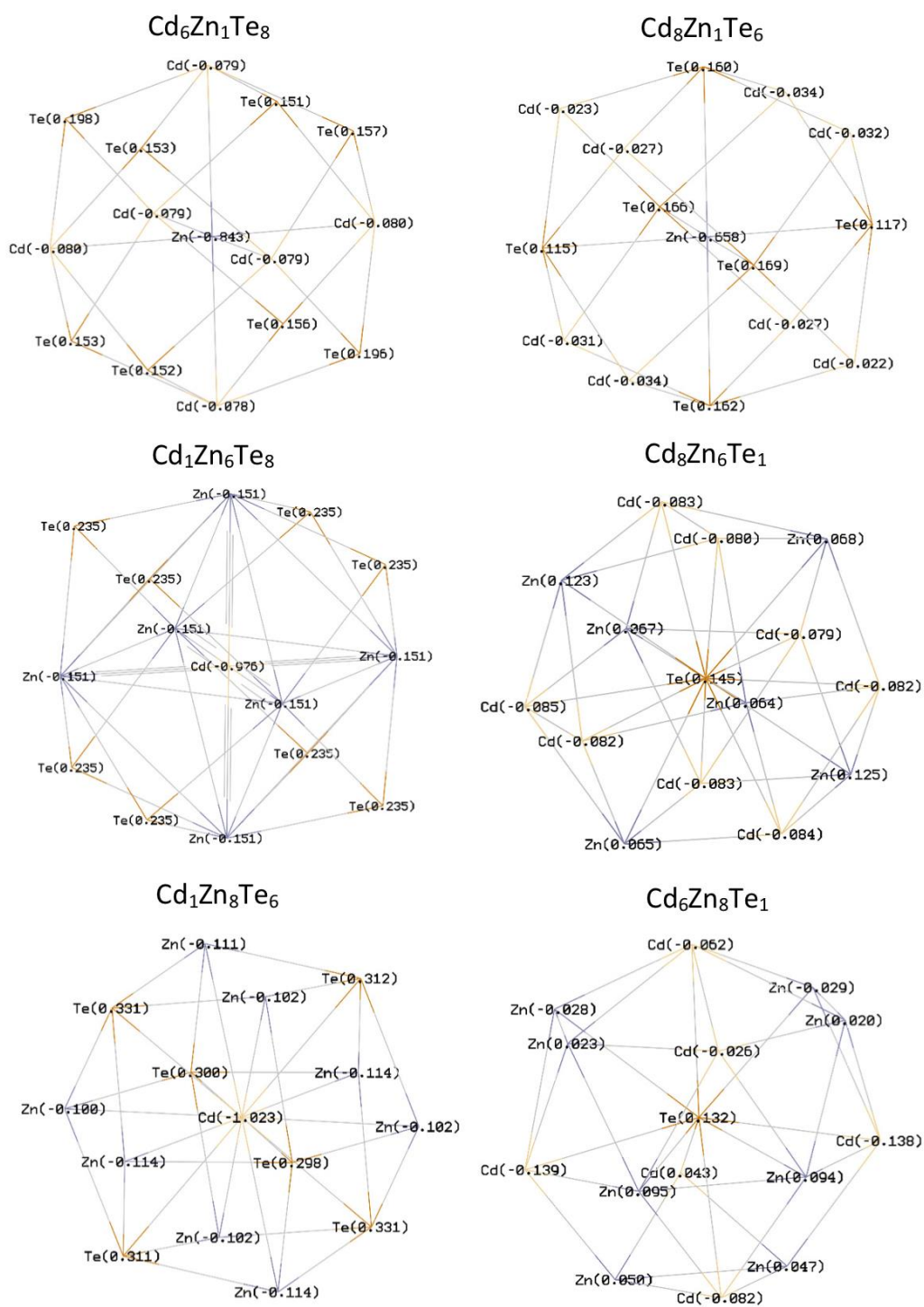


Figure 44. The calculated excess charges of atoms in each model.

Table 15. The total excess charges (q , in $|e|$) and the dipole moments (μ , in Debyes) for various CdZnTe nanoparticles.

Model	q_{Cd}	q_{Zn}	q_{Te}	μ_x	μ_y	μ_z	μ_T
Cd ₆ Zn ₁ Te ₈	-0.474	-0.842	1.316	-0.012	-0.034	0.043	0.056
Cd ₈ Zn ₁ Te ₆	-0.230	-0.658	0.888	0.064	0.017	-0.018	0.069
Cd ₁ Zn ₆ Te ₈	-0.975	-0.906	1.881	0.031	-0.034	-0.082	0.035
Cd ₈ Zn ₆ Te ₁	-0.658	0.513	0.145	0.022	0.038	-0.031	0.054
Cd ₁ Zn ₈ Te ₆	-1.022	-0.860	1.882	0.048	0.012	0.015	0.052
Cd ₆ Zn ₈ Te ₁	-0.404	0.272	0.132	0.235	-0.051	-0.166	0.290

Figure 45 shows HOMO and LUMO pictures of ternary cubic nanoparticles. HOMO and LUMO localizations are almost symmetric over the structures. Negative HOMO and LUMO localizations are mainly on and near the Te, whereas localizations on the Cd and Zn atoms are mainly in the positive regions.

Charge density (CD) and electrostatic potential (ESP) pictures of all the nanoparticles are shown in Figure 46. Charge density has a uniform distribution for all the nanoparticles considered. ESP is usually used as a measure of electronegativity and partial charges of a molecule. Negative ESP is mainly localized over the Te atom and it looks like a yellowish blob while the positive regions are mainly localized around Zn and Cd atoms.

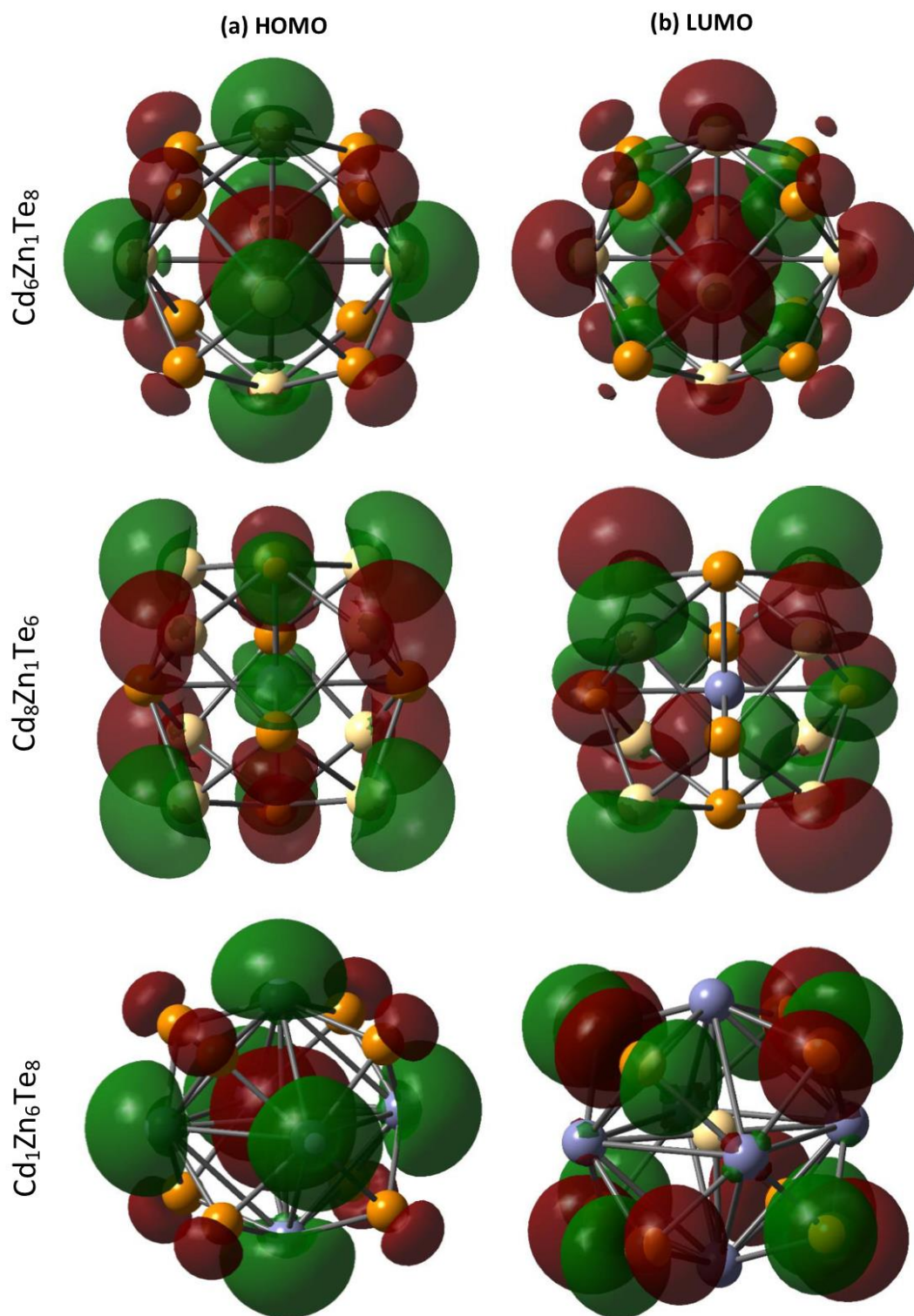


Figure 45. HOMO and LUMO pictures of the CdZnTe ternary nanoparticles. Green and red colors represent the positive and negative isosurfaces for HOMO and LUMO, respectively.

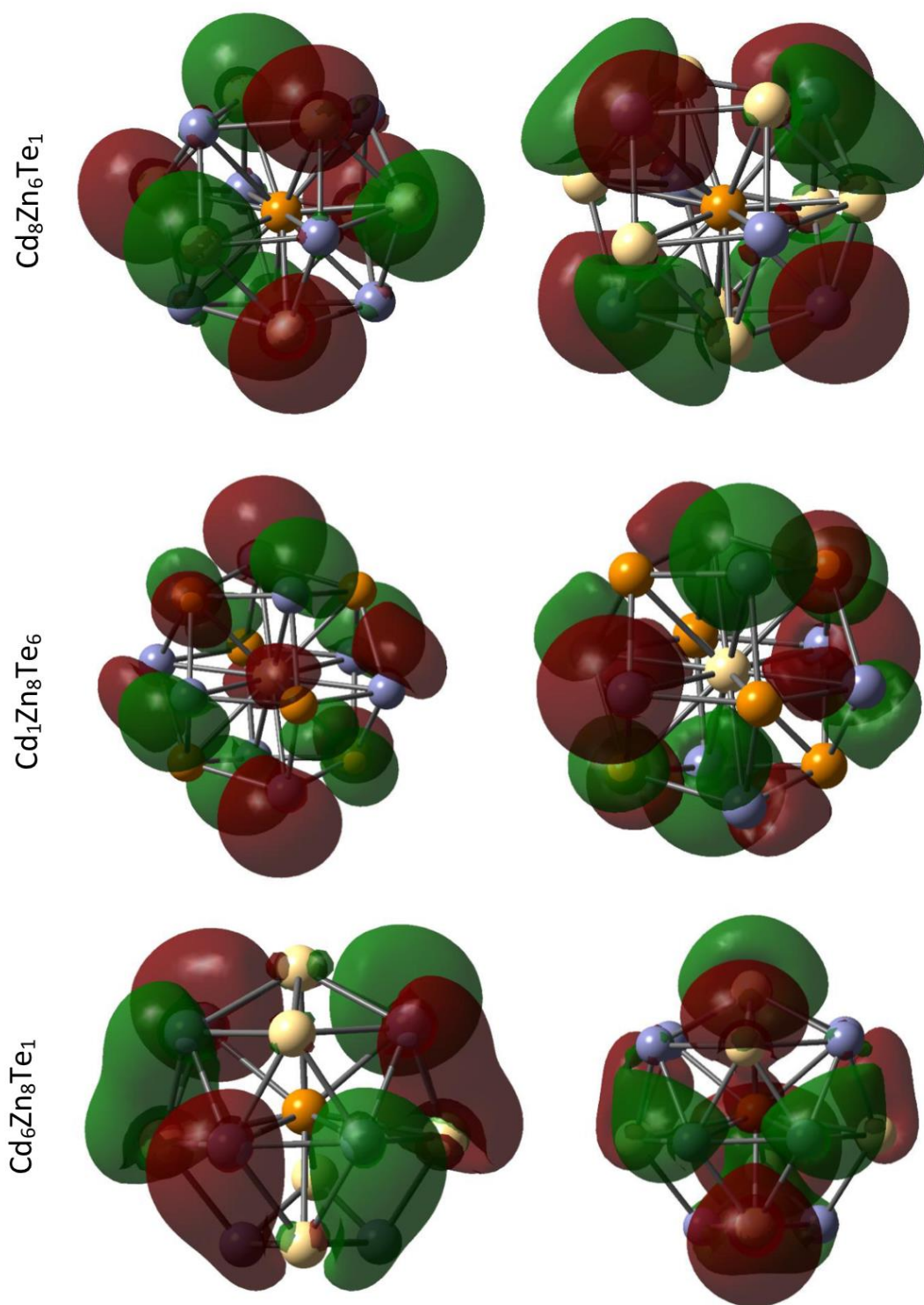


Figure 45. (Continued).

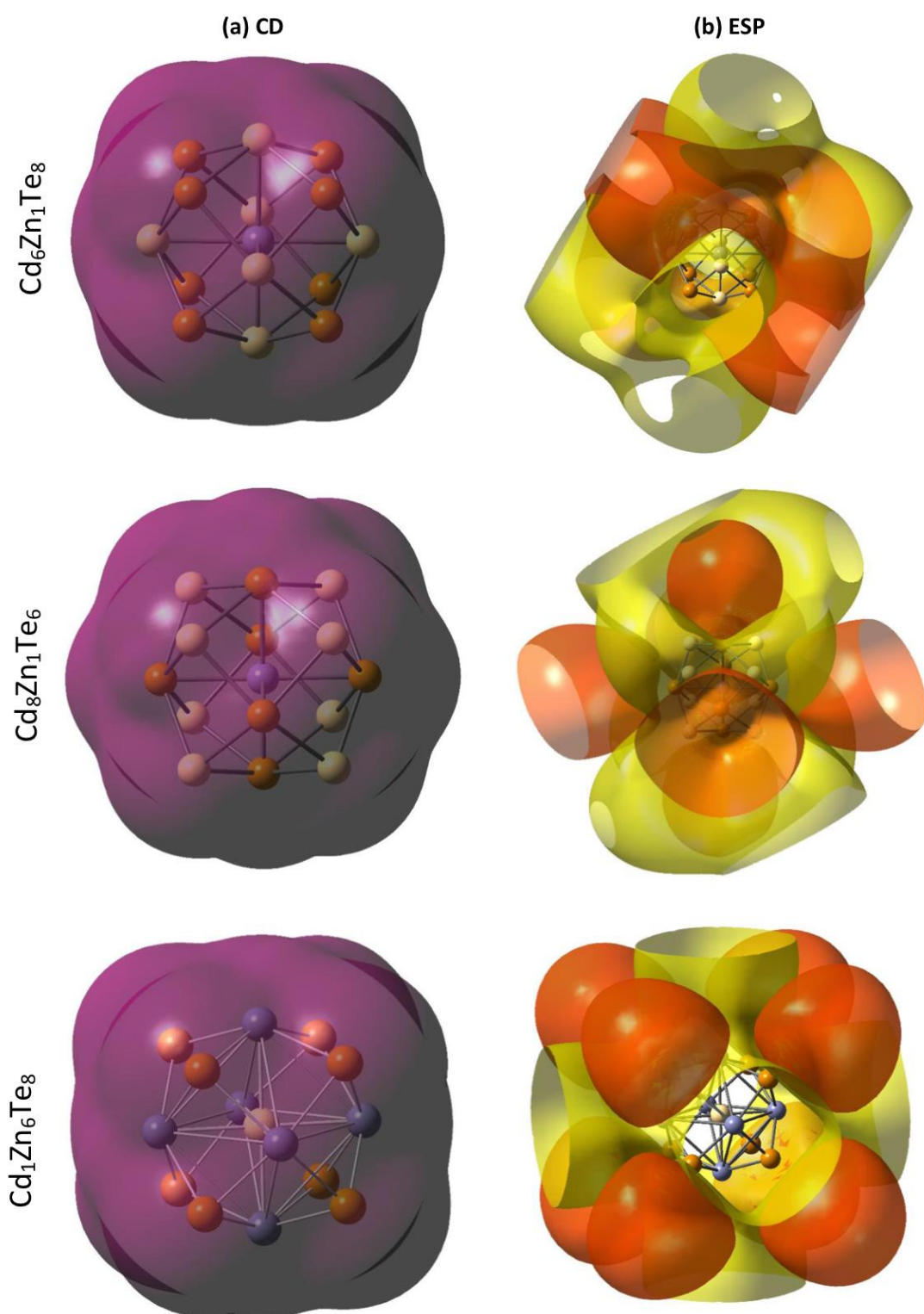


Figure 46. Charge density (CD) and electrostatic potential (ESP) pictures of CdZnTe ternary nanoparticles. ESP picture: yellow and orange colors represent positive and negative potential, respectively.

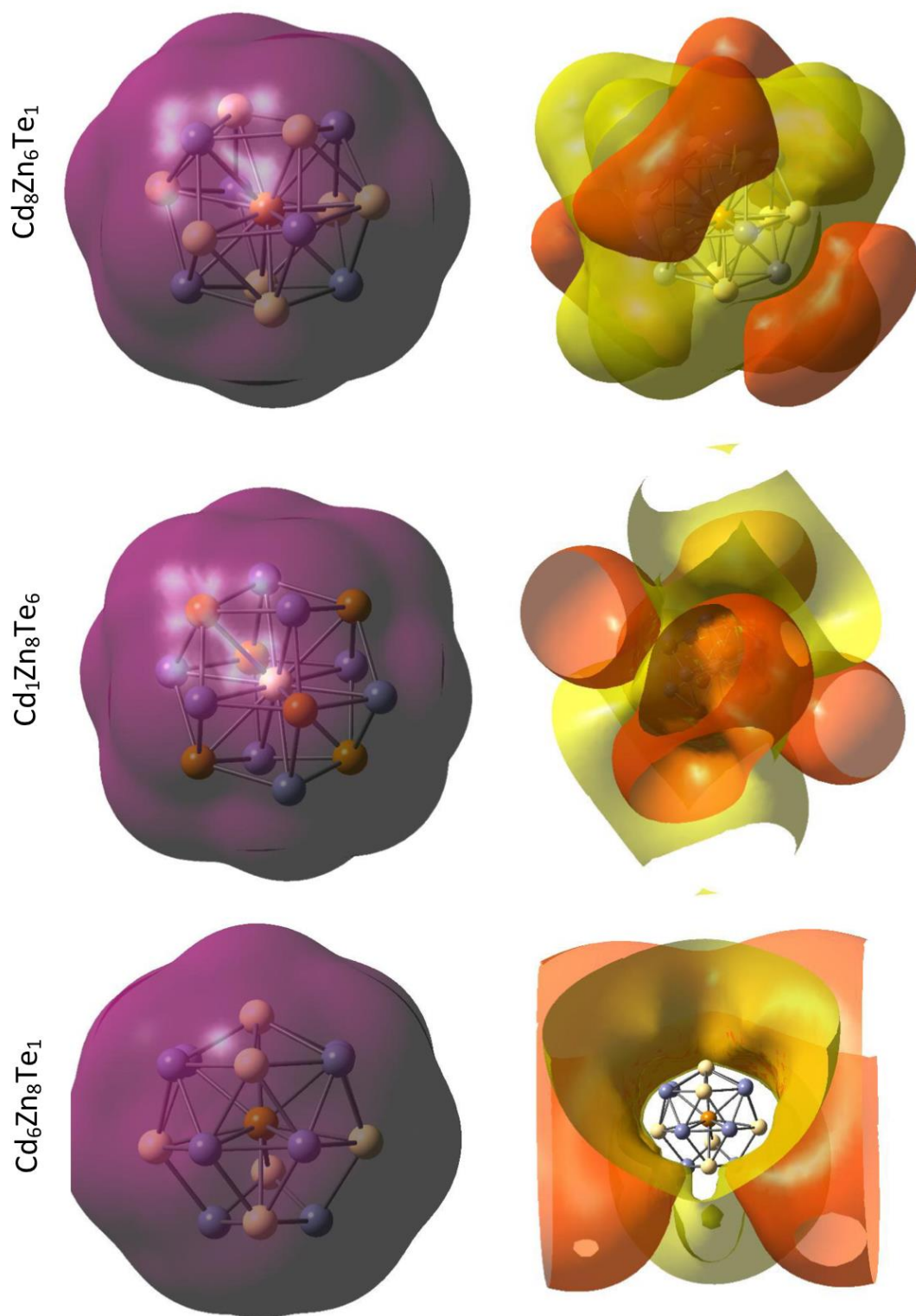


Figure 46. (Continued).

Spin density (SD) figures are given in Figure 47. As it may be seen from the figure that the spin density distribution is symmetric over the $\text{Cd}_6\text{Zn}_1\text{Te}_8$, $\text{Cd}_6\text{Zn}_1\text{Te}_8$ and $\text{Cd}_1\text{Zn}_8\text{Te}_6$ and the negative spin density is localized on Te atoms, whereas the positive spin density localization is on Zn atom in the center.

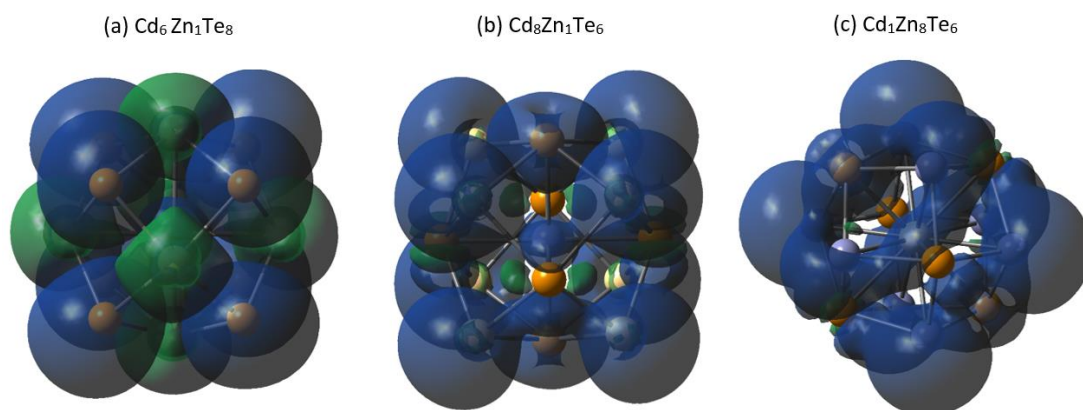


Figure 47. Spin density (SD) pictures of CdZnTe ternary nanoparticles with nonzero spin. Green (alpha spin) and blue (beta spin) colors represent the positive and negative spin density, respectively.

Density of states (DOS) is important, because the occupied and unoccupied molecular orbitals can be seen on DOS spectrum. Using Mulliken population analysis, we have plotted the density of states (DOS) spectra (see Figure 48) for all CdZnTe nanoparticles using GaussSum 2.2 software [137]. The analysis of the density of states shows that the electronic structure is strongly influenced by the nanoparticle stoichiometry. Furthermore, the density of localized states has a sharply increasing tendency in the region of -15 eV. It is also seen that the electron levels are spin polarized for the $\text{Cd}_6\text{Zn}_1\text{Te}_8$, $\text{Cd}_8\text{Zn}_1\text{Te}_6$ and $\text{Cd}_1\text{Zn}_8\text{Te}_6$ nanoparticles. Predictions based on the different compositions lead to similar distribution of orbital energies. Moreover, the results of DOS for the $\text{Cd}_6\text{Zn}_1\text{Te}_8$ and $\text{Cd}_8\text{Zn}_1\text{Te}_6$ nanoparticles between -2 and -4 eV show similar DOS profile as seen in the $\text{Cd}_{0.825}\text{Zn}_{0.175}\text{Te}$ bulk of this material [138].

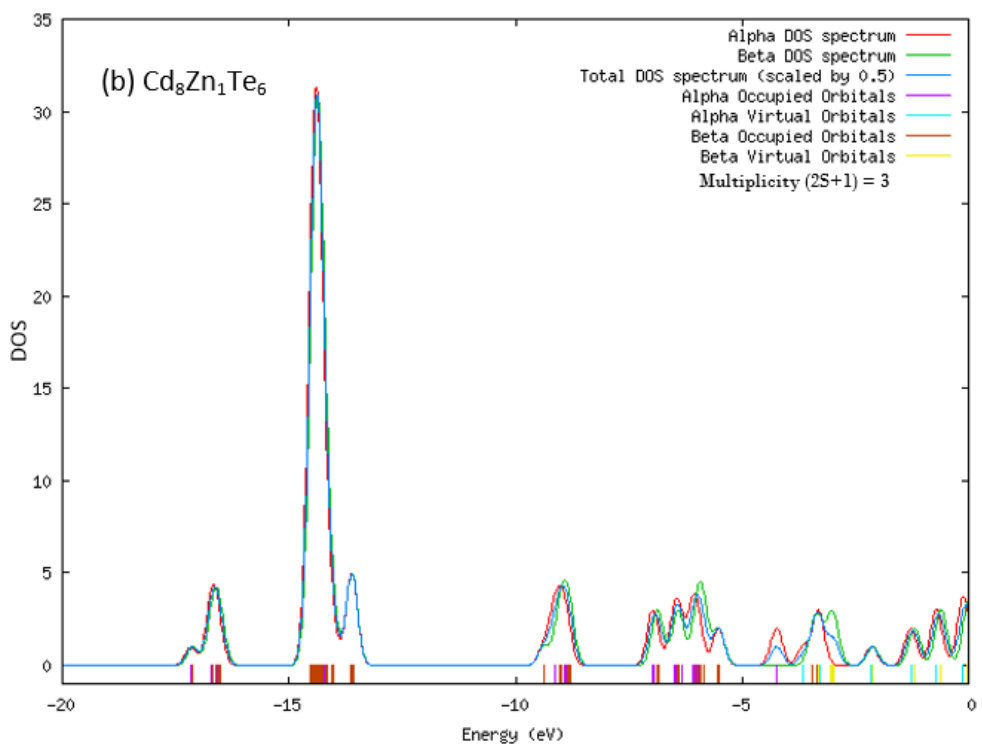
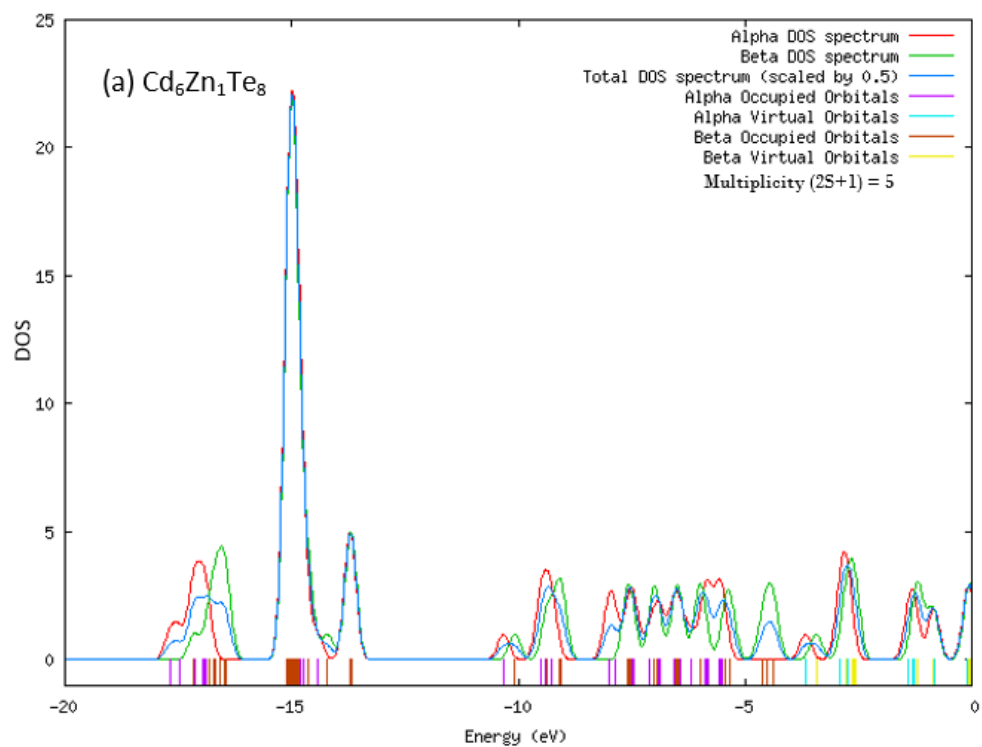


Figure 48. Density of states (DOS) spectra for CdZnTe ternary nanoparticles using Mulliken population analysis.

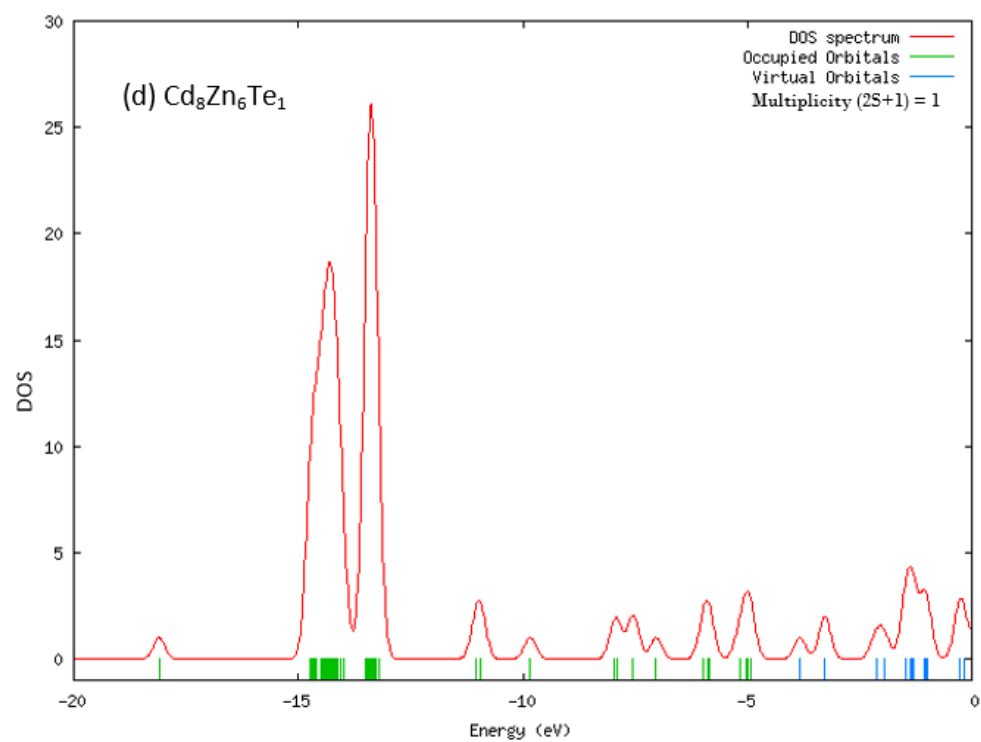
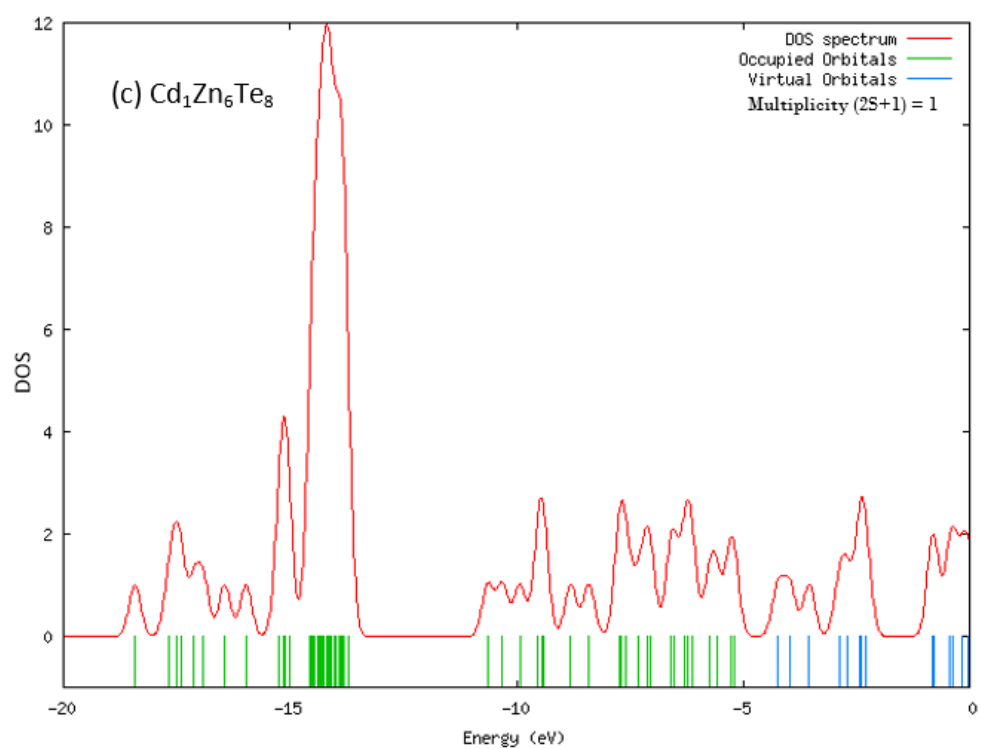


Figure 48. (Continued).

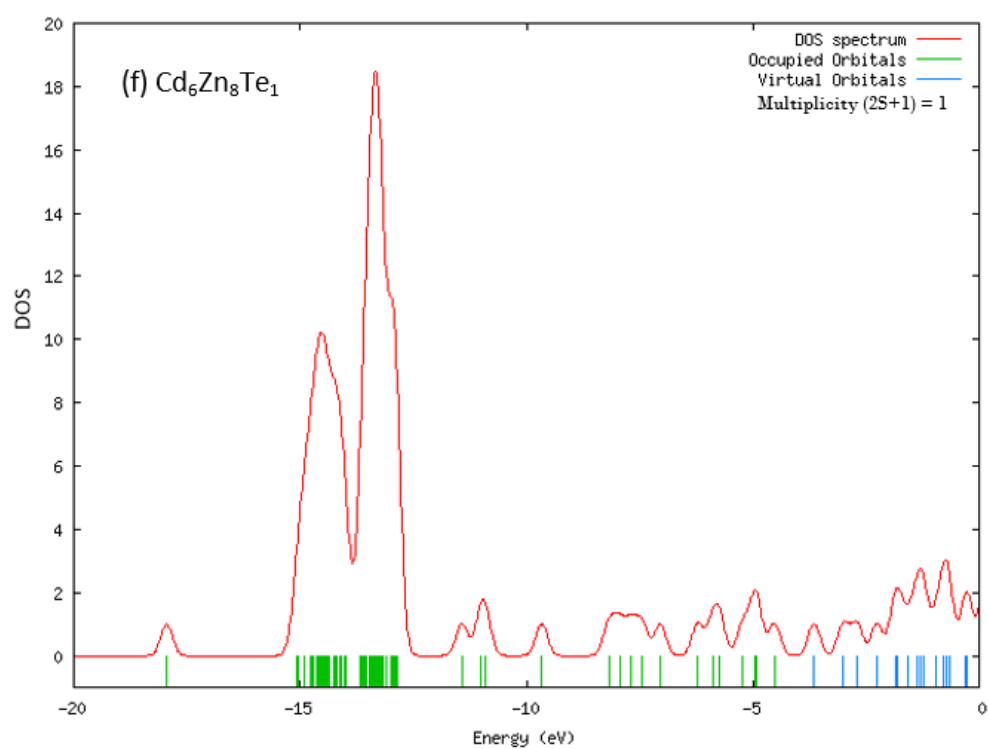
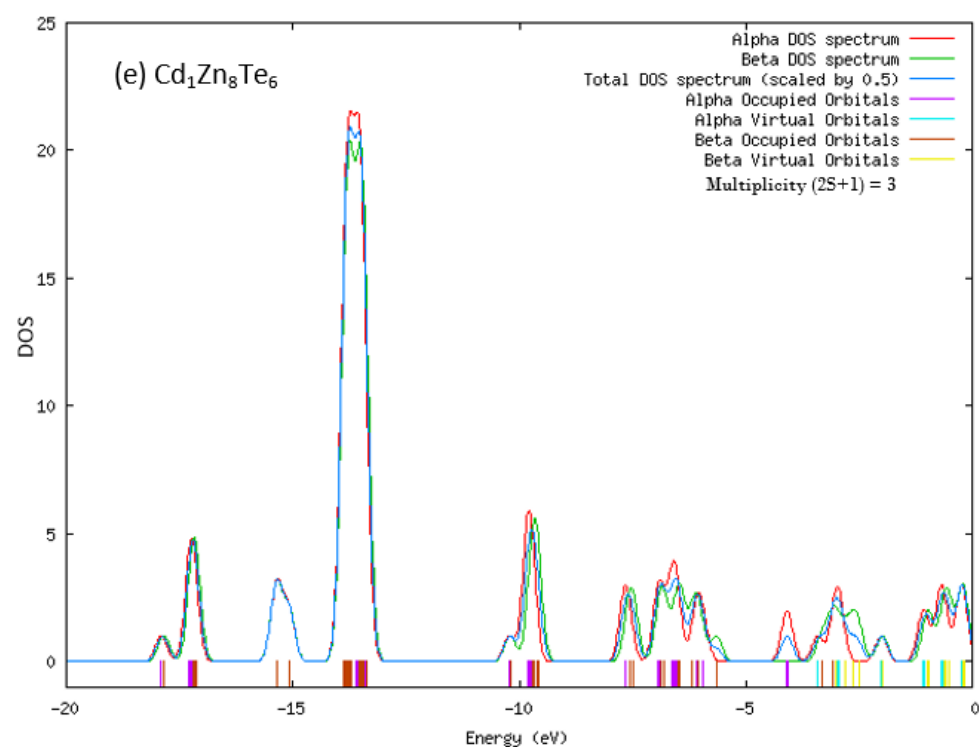


Figure 48. (Continued).

3.6 Structural and Thermal Properties of Cd-Zn-Te Ternary Nanoparticles: Molecular-Dynamics Simulations

3.6.1 Introduction

A molecular dynamics simulations using a recently developed CdZnTe bond order potential is carried out to study structural and thermodynamical properties of the CdZnTe spherical-like ternary nanoparticles with 167-357 atoms in the temperature range 100 K-600 K. The heat capacity calculation is performed as depending on the size and the stoichiometry at various temperatures using a non-equilibrated molecular dynamics simulation strategy. Moreover, the segregation phenomena of Cd, Zn, and Te atoms in Cd-Zn-Te nanoparticles are researched by the order parameter R depending on nanoparticle size and temperature. The radial distribution function has also been calculated for the $\text{Cd}_{0.50}\text{Zn}_{0.50}\text{Te}$ nanoparticle with 357 atoms at 100 K and 600 K.

3.6.2 Modelling and Calculation Procedure

In this study, we present atomistic molecular-dynamics (MD) simulations of Cd-Zn-Te ternary spherical NPs with 167-357 atoms with diameters 1.2 to 1.5 nm under heat treatment by applying non-equilibrated process. The size and composition dependence of heat capacity C_v have been investigated for CdZnTe ternary nanoparticles. After that, the variation of the order parameter under heat treatment is studied to understand the character of the stable structures and analyze segregation phenomena of Zn, Cd, and Te in Cd-Zn-Te spherical nanoparticles depending on the number of particle and temperature, and finally the behavior of the radial distribution function is investigated for $\text{Cd}_{0.50}\text{Zn}_{0.50}\text{Te}$ spherical nanoparticles at temperatures 100 and 600 K.

The simulations of spherical nanoparticles were made via LAMMPS using BOP. Thermal equilibrium is controlled by choosing a Nosé-Hoover thermostat and the canonical ensemble during the whole simulations. In the computations, the heating procedure is applied, where the temperature was raised by 25 K. The simulations are implemented with starting at 1 K, and then temperature is raised till 600 K for Cd-Zn-Te spherical nanoparticles with different size and stoichiometry. In all the simulations, each run is performed for 100000 MD steps (0.1 ps) with a time step of 0.1 fs. During the simulations the non-equilibrated MD procedure is followed. In this method, the system's temperature is gradually increased by 25 K without waiting for the system to reach the equilibrium state. Boltzmann velocity distribution is used to generate particle velocities at the corresponding temperature. The cut-off radius of 14.70 Å was used for maximum interaction range. The initial structures of the $\text{Cd}_{0.50}\text{Zn}_{0.50}\text{Te}$, as an example, spherical nanoparticle models generated from zinc-blend crystal structure are shown in Figure 49.

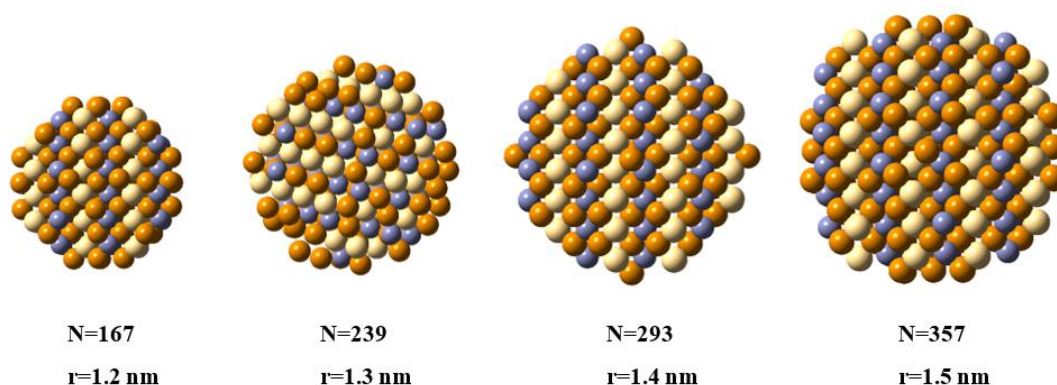


Figure 49. The initial structures of the $\text{Cd}_{0.50}\text{Zn}_{0.50}\text{Te}$ spherical nanoparticle models generated from zinc-blend crystal structure for MD simulations.

3.6.3 Results and Discussions

We have calculated the variation of the potential energy and the composition dependence of heat capacity, the variation of heat capacity with size and Zn and Cd content, the variation of order parameter with temperature and size for the $\text{Cd}_{1-x}\text{Zn}_x\text{Te}$ ternary alloys spherical nanoparticles with Zn concentrations for $x = 0.25, 0.50$ and 0.75 and finally radial distribution function (RDF) of the $\text{Cd}_{0.50}\text{Zn}_{0.50}\text{Te}$ nanoparticle at temperatures 100 K and 600 K .

Potential energy as a function of temperature for various CdZnTe compounds is depicted in Figure 50. Note that the slope of the curve does not change sharply over a wide temperature range and the value of the energy does not abruptly change.

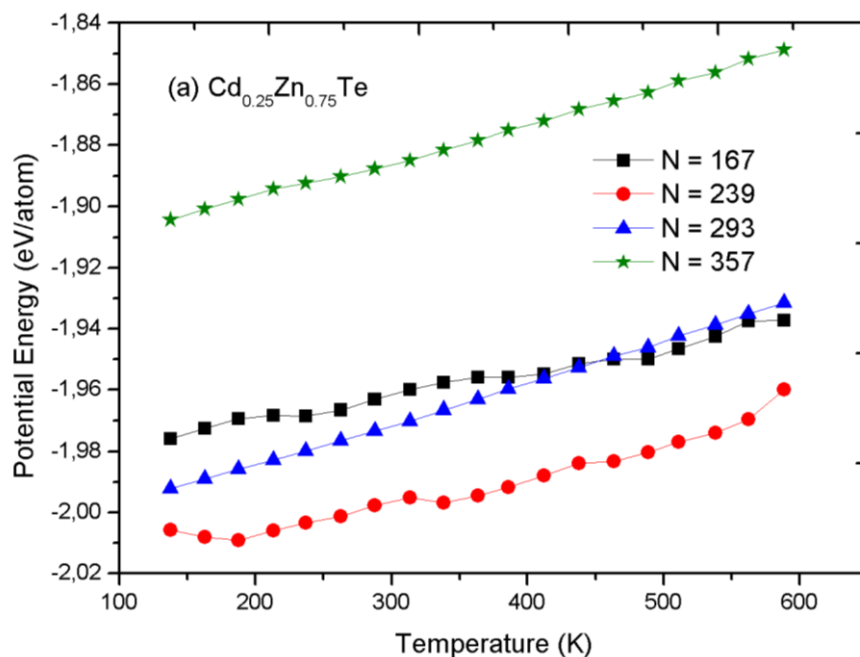


Figure 50. Variation of the potential energy as a function of temperature according to the size and stoichiometry of the nanoparticles. (a) $\text{Cd}_{0.25}\text{Zn}_{0.75}\text{Te}$, (b) $\text{Cd}_{0.50}\text{Zn}_{0.50}\text{Te}$, and (c) $\text{Cd}_{0.75}\text{Zn}_{0.25}\text{Te}$.

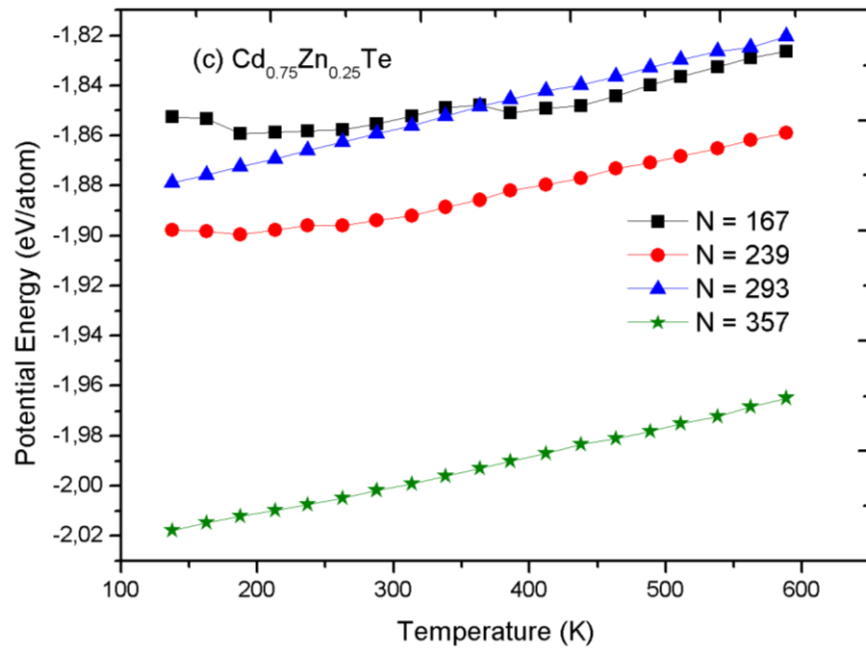
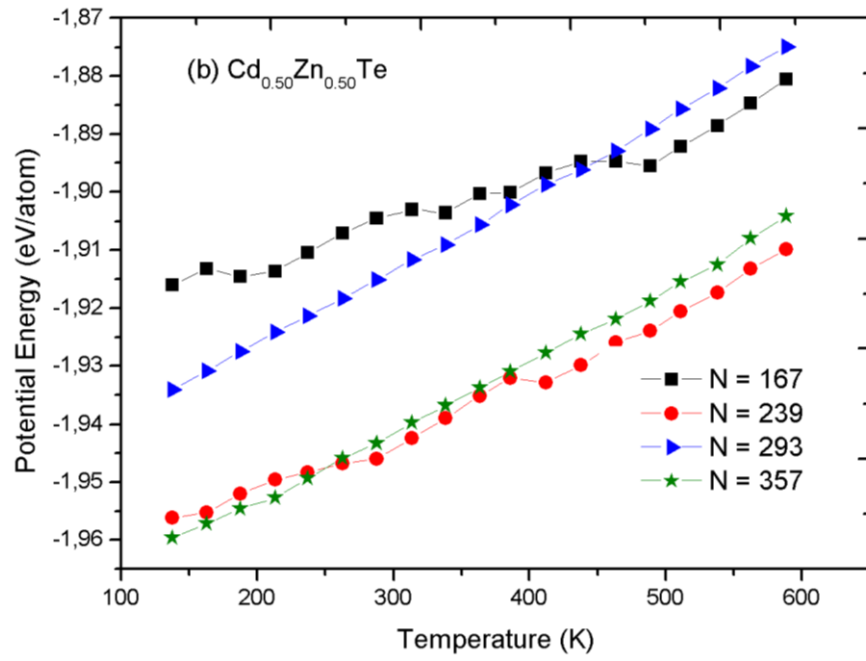


Figure 50. (Continued).

One of the aim of this study is to research the effect of size and composition on the behavior of the heat capacity using a molecular dynamics simulation. The heat capacity is formally described as the rate of internal energy in accordance with temperature (see Eqn. 3.4).

The variation of the heat capacity C_v versus number of atoms in the temperature range 100-600 K for the concentrations $x = 0.25, 0.50$ and 0.75 is shown in Figure 51. For all concentrations, the heat capacity values show an increasing trend with increasing size up to nanoparticle with 293 atoms, then starts to decrease.

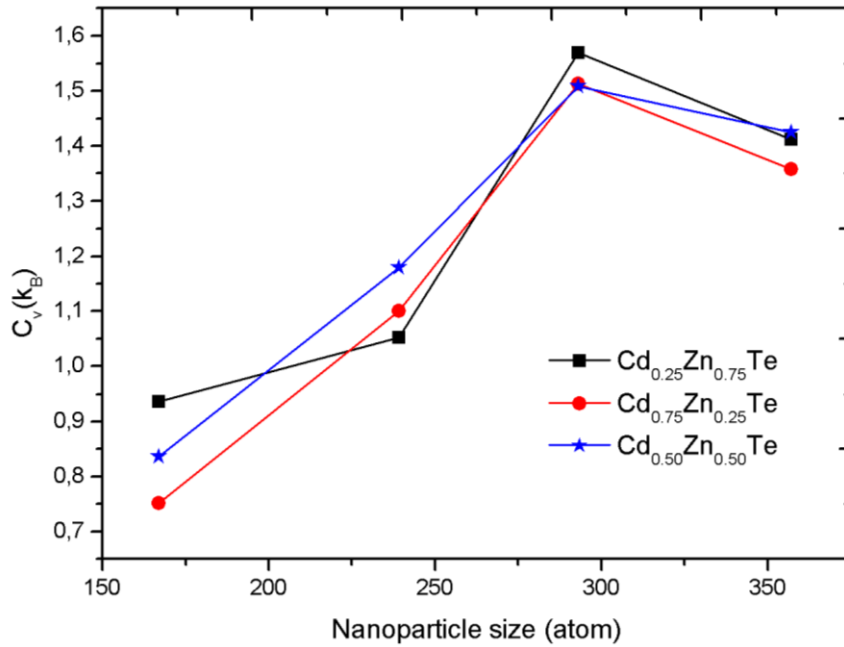


Figure 51. Size dependence of the calculated heat capacity C_v for the $\text{Cd}_{1-x}\text{Zn}_x\text{Te}$ nanoparticles in the temperature range 100 K-600 K.

Figure 52 (Heat capacity vs Zn and Cd concentration, respectively) displays the calculated heat capacity C_v values as a function of (a) Zn and (b) Cd concentration (x) for the sizes $N=167, 239, 293$ and 357 . As it can be seen from figures, the concentration of zinc and cadmium have significant influence on the heat capacity behavior in terms of nanoparticle size. $\text{Cd}_{1-x}\text{Zn}_x\text{Te}$ alloys show different values with increasing the Zn and Cd concentration for heat capacity C_v [136]. Although there is no thermal data in the literature for CdZnTe nanoparticles, we may compare the trend of the present results for nanoparticles with that of bulk values. Experimental measurements for heat capacity on CdZnTe ternary alloy bulk material shows fluctuations with respect to Zn concentration [136]. See Figure 53 for this anomaly. In this sense the present results show similar behavior as seen in the bulk [136]. From these results one can infer that the details of the evolution of C_v are strongly correlated with the size and the stoichiometry. The size dependence characteristic of heat capacity of nanoparticles has been also obtained in recent studies for metals [135] and binary alloys [19].

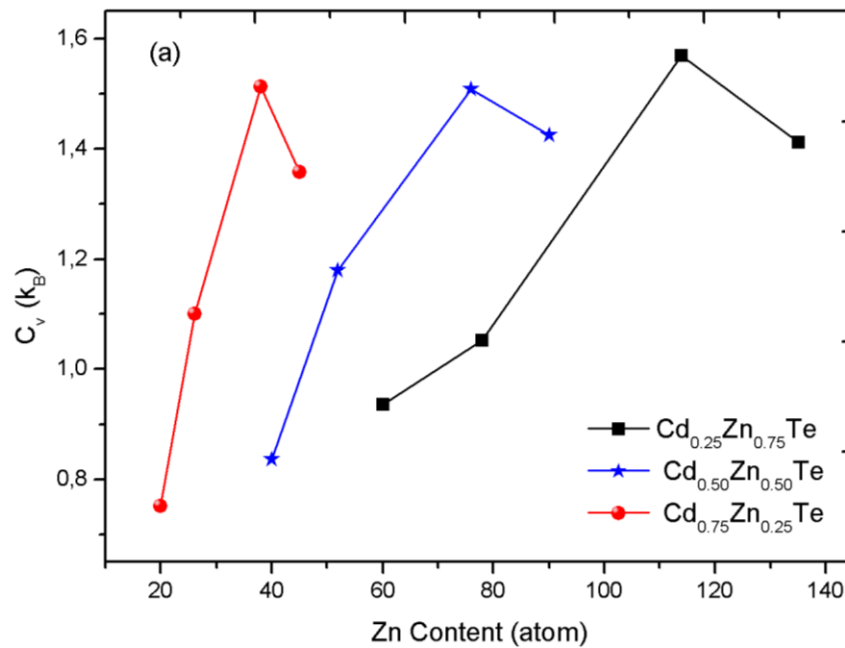


Figure 52. Variation of the calculated heat capacity C_v as a function of (a) Zn and (b) Cd concentrations (x) for the sizes $N=167, 239, 293$ and 357 .

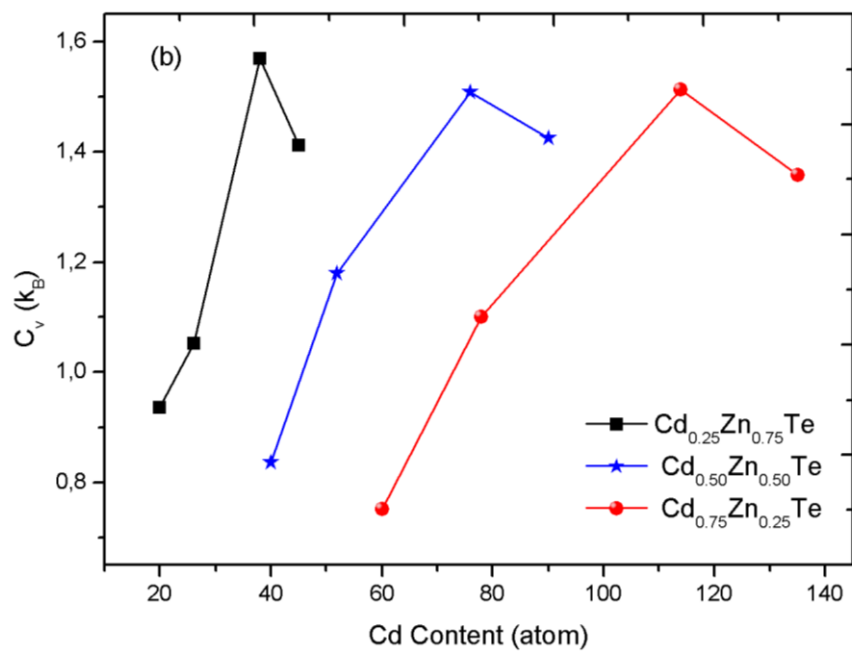


Figure 52. (Continued).

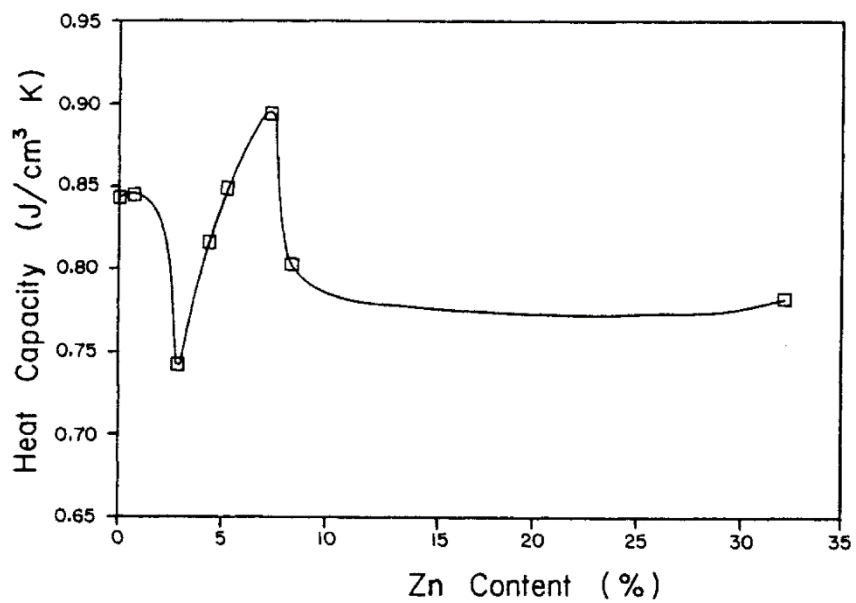


Figure 53. Experimental heat capacity profile for CdZnTe bulk material. [136].

Figure 54 (a), (b) and (c) show the order parameter-particle size graphs of considered $\text{Cd}_{0.25}\text{Zn}_{0.75}\text{Te}$, $\text{Cd}_{0.50}\text{Zn}_{0.50}\text{Te}$ and $\text{Cd}_{0.75}\text{Zn}_{0.25}\text{Te}$ ($N=167, 239, 293$ and 357) spherical nanoparticles. From Figure 54 (a), it can be found that for ternary nanoparticle, R_{Te} is larger than R_{Cd} and R_{Zn} for $N=239$ and R_{Cd} is larger than R_{Zn} and R_{Te} for $N=167, 293$ and 357 . This indicates that Te atoms for $N=239$ and Cd atoms for $N=167, 293$ and 357 tend to occupy reside on the surface. The tendency of Te and Cd is because of the lower surface and cohesive energy of Te and Cd. Low R_{Zn} values for $N=167$ and 239 , and R_{Te} values for $N=293$ and 357 indicate that Zn and Te atoms tend to locate at the center, separately. According to the order parameter plot in $\text{Cd}_{0.25}\text{Zn}_{0.75}\text{Te}$, $\text{Cd}_{0.50}\text{Zn}_{0.50}\text{Te}$ and $\text{Cd}_{0.75}\text{Zn}_{0.25}\text{Te}$ spherical nanoparticles, the composition Zn and Te atom compositions have almost similar effect on the formation of the nanoparticles. For all concentrations, the variation of the order parameter with number of atoms indicates that order parameter of $\text{Cd}_{0.75}\text{Zn}_{0.25}\text{Te}$ has larger value than that of $\text{Cd}_{0.25}\text{Zn}_{0.75}\text{Te}$ and $\text{Cd}_{0.50}\text{Zn}_{0.50}\text{Te}$.

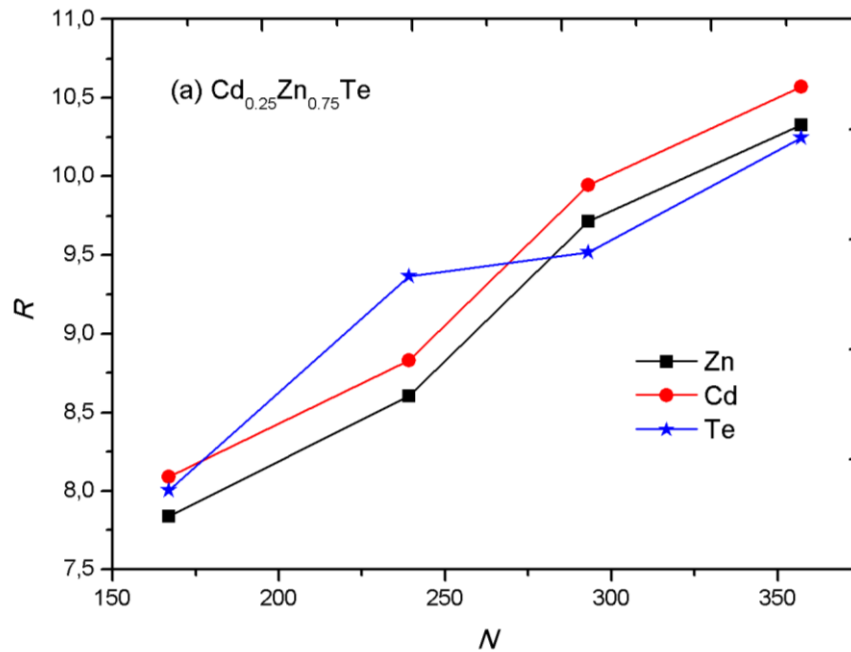


Figure 54. Variation of the order parameter R_{Cd} , R_{Zn} , and R_{Te} with respect to size ($N=167, 239, 293$ and 357). (a) $\text{Cd}_{0.25}\text{Zn}_{0.75}\text{Te}$, (b) $\text{Cd}_{0.50}\text{Zn}_{0.50}\text{Te}$ and (c) $\text{Cd}_{0.75}\text{Zn}_{0.25}\text{Te}$.

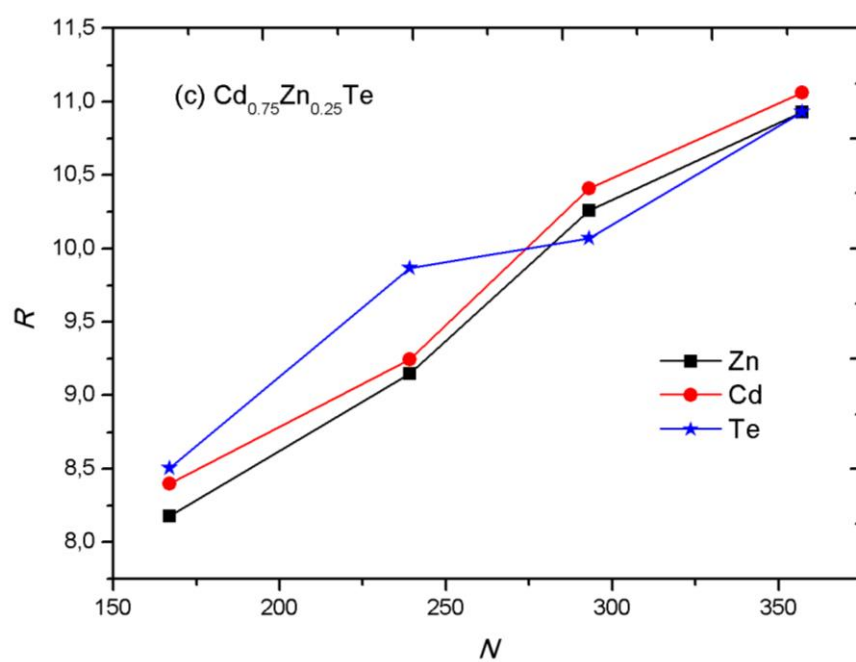
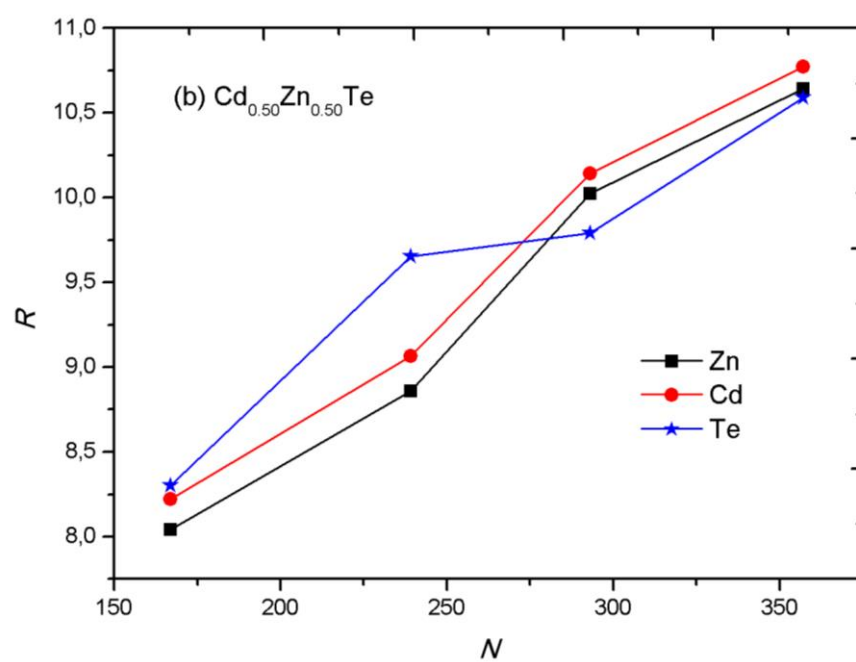


Figure 54. (Continued).

Figure 55 (a), (b) and (c) show the order parameter-temperature graphs of Cd-Zn-Te nanoparticles with $N=167$, 239, 293 and 357 atoms. The similar effects of the order parameter with temperature can also be seen in Figure 54 (a), (b) and (c).

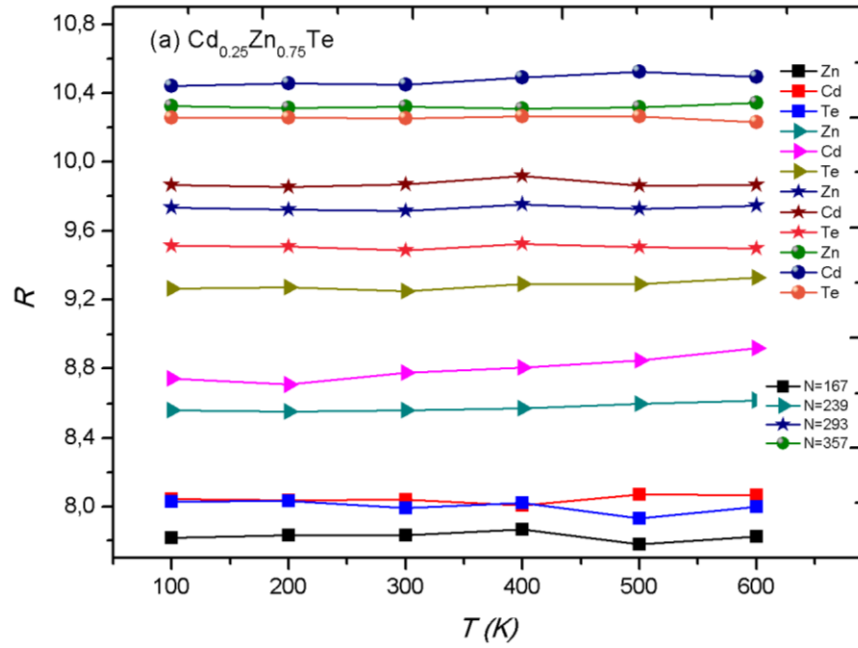


Figure 55. Variation of the order parameter R_{Cd} , R_{Zn} , and R_{Te} with respect to temperature. (a) $\text{Cd}_{0.25}\text{Zn}_{0.75}\text{Te}$, (b) $\text{Cd}_{0.50}\text{Zn}_{0.50}\text{Te}$ and (c) $\text{Cd}_{0.75}\text{Zn}_{0.25}\text{Te}$.

On the other hand, the radial distribution function (RDF) is another important statistical measure to determine the structural properties of materials. The behaviors of the radial distribution function (RDF) of the studied $\text{Cd}_{0.50}\text{Zn}_{0.50}\text{Te}$ spherical nanoparticle with 357 atoms are given in Figure 56 (a) and (b) at 100 K and 600 K, respectively. The peaks indicate that atoms are located around each other in shells of neighbors. The peaks of the radial distribution function are usually sharper at 100 K. This is due to fact that at relatively low temperature the atoms are located more closely to shell structure. However, the peaks are slightly broadened at 600 K, due to the thermal motion. The atoms begin freely to move away from lattice point. The number of obvious peaks in RDF observed at 100 K have decreased with increasing temperature (at 600 K).

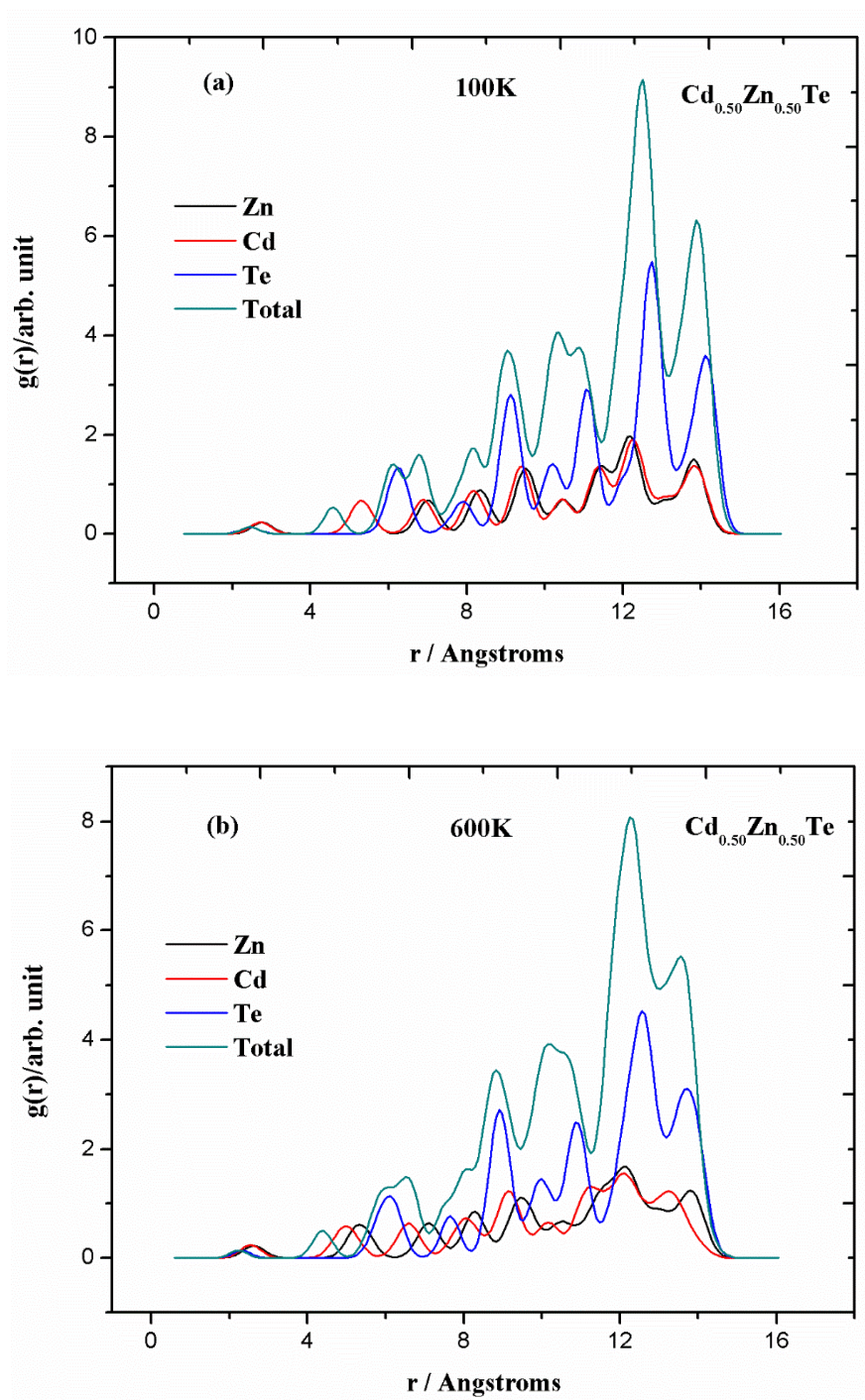


Figure 56. The radial distribution function (RDF) of the $\text{Cd}_{0.50}\text{Zn}_{0.50}\text{Te}$ nanoparticle with 357 atoms at (a) 100 K and (b) 600 K.

Figure 57 represents the structures of the $\text{Cd}_{0.50}\text{Zn}_{0.50}\text{Te}$ spherical nanoparticle with 357 atoms at various temperatures. From Figure 57, it is clearly seen that the deformation in the structure of nanoparticle starts after 300 K.

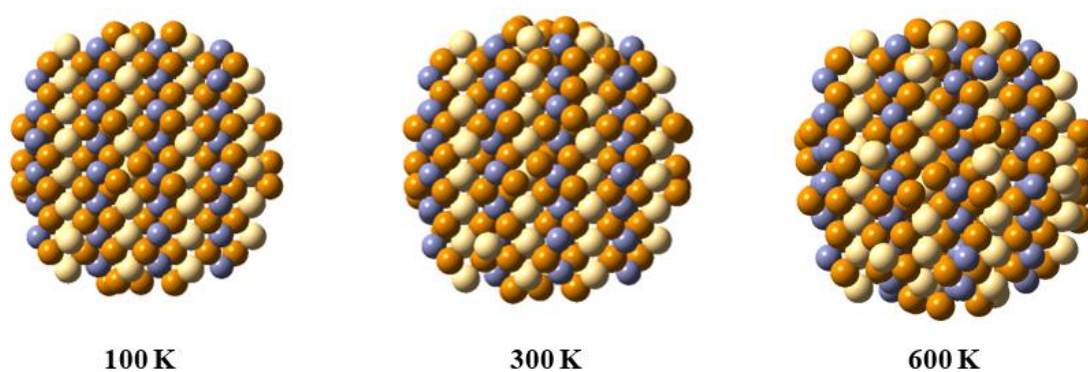


Figure 57. The structures of the $\text{Cd}_{0.50}\text{Zn}_{0.50}\text{Te}$ spherical nanoparticle with 357 atoms at various temperatures.

CHAPTER 4

CONCULUSIONS

In this thesis, CdZnTe ternary alloy nanostructures such as nanorods, clusters and nanoparticles have been investigated theoretically using molecular mechanics method and DFT calculation with B3LYP XC functional using CEP-121G basis set.

This study consists of six main parts. In the first part of the study, MD simulations using an atomistic many-body PEF for $\text{Zn}_x\text{Cd}_{1-x}\text{Te}$ ($x = 0.25, 0.50$ and 0.75) nanorods have been performed [139]. The calculations clearly showed that the $\text{Zn}_x\text{Cd}_{1-x}\text{Te}$ nanorods simulated at various temperatures and stoichiometry have different structural properties. After reaching a temperature of 300K, $\text{Zn}_{0.25}\text{Cd}_{0.75}\text{Te}$ and $\text{Zn}_{0.50}\text{Cd}_{0.50}\text{Te}$ nanorods change from a nanorod to a tubular structure as a result of increased temperature. On the other hand, $\text{Zn}_{0.75}\text{Cd}_{0.25}\text{Te}$ nanorod changes to become 2D (nanoribbon like structure) at 1200 K, it changes again to become 3D (capsule like structure) and a 1D (atom chain) structure at 2100 K. In all three nanorod structures, Zn atoms start to separate from the system after reaching 300 K. After evaporation of Zn the total energy of the systems show an increasing trend as seen from the Figures 3, 5 and 6. It is expected that the outcomes of the present study will provide useful information in understanding the structural properties of $\text{Zn}_x\text{Cd}_{1-x}\text{Te}$ ($x = 0.25, 0.50$ and 0.75) nanorods at various temperatures for both experimental and theoretical efforts.

In the second part of the study, we have used an atomistic many-body PEF to study the structural properties of ZnTe and CdTe nanorods [140]. The structural properties of CdTe and ZnTe binary nanorods are strongly dependent on temperature. The calculations showed that ZnTe and CdTe binary nanorods change from a nanorod to a capsule structure after reaching 1500 K and 2100 K, respectively.

In the case of ZnTe binary nanorod, Zn atoms separate first and a pure Te system remains and it changes to a tubular structure at 2400 K; however, in the case of CdTe binary, both atoms remain even at high temperatures and it changes again to a tubular structure at 3000K. Furthermore CdTe nanorod changes again to a capsule like structure at 3300 K. Although the Zn atoms of ZnTe system start to separate at about 900 K, the total energy of the system shows an increasing trend, as seen in Figure 4.

In the third part of the study, the mechanical properties of CdZnTe nanowires under uniaxial stretching and compression are studied based on MD simulations with Bond Order Potential (BOP) [141]. It is found that CdZnTe nanowires with 263 atoms appear more ductile than that of 641 atoms at 1 K. Moreover, the temperature and width exert significant effects on the mechanical properties of CdZnTe nanowires under stretching. Under compression, CdZnTe nanowires with 641 atoms seem like an amorphous nanoparticle. These results could help future researches for CdZnTe nanowire applications such as solar cells, optoelectronic devices, industrial imaging systems and security for their mechanical strengthen and compression properties.

In the fourth part of the study, DFT calculations at B3LYP/CEP-121G level for the structural and electronic properties of $Zn_mCd_nTe_k$ ($m+n+k=2-4$) clusters have been performed [142]. The geometries of the investigated models have been fully optimized such that all harmonic frequencies are obtained to have a positive value. The Te_2 , CdTe, $ZnTe_2$ and $CdTe_2$ clusters in their electronic ground state have been found triplet, the rest have been found singlet. When combined with the Zn and Te atoms, Mulliken charge on Cd atom has negative and positive charge, respectively. The energy gap (E_g) decreases when the number of atoms in the clusters increases. The most probable dissociation channel and energy results are consistent with the E_b values of dimers and trimers as expected. It is expected that the outcomes of the study will ensure useful information for a better understanding the electronic and chemical stabilities of the ZnCdTe clusters for both experimental and theoretical efforts.

In the fifth part of the study, the molecular dynamics simulation results obtained by using a recently developed Cd-Zn-Te bond order potential for the

structural and thermal properties of the CdZnTe ternary nanoparticles, with 15 atoms and with different stoichiometry, at various temperatures are presented for the first time [143]. It is found that the heat capacity of CdZnTe ternary nanoparticles in the temperature range from 100 K to 600 K depend on the stoichiometry of the system. The heat capacity indicates fluctuation and a sharp increase in terms of number of Cd, Zn and Te atoms. It is concluded that Zn, Cd and Te concentrations have significant influence on the heat capacity. Experimentally observed stoichiometry dependent anomaly in heat capacity of CdZnTe bulk material has been observed in the calculated heat capacity of the nanoparticles of the same material. In addition, the character of the stable structures is investigated by studying the order parameter, and segregation phenomena of Zn, Cd, and Te were analyzed in the CdZnTe ternary nanoparticles. The results for the nanoparticles provide us to understand the effect of the composition on the nanoparticles at different temperatures to guide the experimentalists, because the segregation is encountered during the growth of the CdZnTe at high temperatures, which results in non-uniformity in the stoichiometry. In addition, single point energy calculations by DFT method with B3LYP/CEP-121G level have been performed to investigate the electronic properties such as HOMO-LUMO energies, Mulliken charges on the atoms, charge densities, spin densities and DOS of the CdZnTe ternary nanoparticles. The ground state energy of Cd₆Zn₁Te₈ was obtained spin multiplicity 5, the models Cd₈Zn₁Te₆ and Cd₁Zn₈Te₆ have multiplicity 3, and the rest of the models have multiplicity 1. The heat capacity values of the nanoparticles depending on the composition are also consistent with the HOMO-LUMO band gap energy. Density of states of the CdZnTe nanoparticles with different compositions show that the electronic structure is strongly influenced by the nanoparticle stoichiometry.

In the last part of the study, molecular dynamics simulation results by using a recently developed CdZnTe BOP for the structural and thermal properties of different sizes and the stoichiometry of Cd-Zn-Te ternary spherical nanoparticles are presented at various temperatures for the first time [144]. It is found that the heat capacity of Cd-Zn-Te spherical nanoparticles in the temperature range from 100 K to 600 K depend on the size and the stoichiometry of the system. The heat capacity indicate fluctuation

and a sharp increase for $N = 167, 239$ and 293 , but it decreases for $N = 357$. It is also observed that Zn and Cd concentrations has significant influence on the heat capacity. Stoichiometry dependence of the heat capacity for the bulk of this material has also been observed experimentally. In addition, the character of the stable structures is analyzed by calculating the order parameter, and segregation phenomena of Zn, Cd, and Te were analyzed in Cd-Zn-Te spherical nanoparticles. Furthermore, the structural characteristics and the atomic distribution in Cd-Zn-Te spherical nanoparticles are studied. Moreover, it is concluded that the peaks of the RDF for the $\text{Cd}_{0.50}\text{Zn}_{0.50}\text{Te}$ spherical nanoparticle with 357 atoms are sharper at 100 K than at 600 K.

REFERENCES

- [1] C. L. Wang, H. Zhang, J. H. Zhang, M. J. Li, H. Z. Sun, and B. Yang, "Application of ultrasonic irradiation in aqueous synthesis of highly fluorescent CdTe/CdS core-shell nanocrystals," *J. Phys. Chem. C*, vol. 111, no. 6, pp. 2465–2469, 2007.
- [2] P. Yang, S. Tretiak, A. E. Masunov, and S. Ivanov, "Quantum chemistry of the minimal CdSe clusters," *J. Chem. Phys.*, vol. 129, no. 7, 2008.
- [3] A. K. Kushwaha, "Lattice dynamical calculations for HgTe, CdTe and their ternary alloy $\text{Cd}_x\text{Hg}_{1-x}\text{Te}$," *Comput. Mater. Sci.*, vol. 65, pp. 315–319, 2012.
- [4] A. Gupta, V. Parikh, and A. D. Compaan, "High efficiency ultra-thin sputtered CdTe solar cells," *Sol. Energy Mater. Sol. Cells*, vol. 90, no. 15, pp. 2263–2271, 2006.
- [5] A. Melnikov, "CdZnTe radiation detectors," *Journal of Crystal Growth*, vol. 197, no. 3, pp. 663–665, 1999.
- [6] S. Li, Y. Jiang, D. Wu, B. Wang, J. Li, Y. Zhang, W. Wang, X. Lan, H. Zhong, and L. Chen, "Synthesis and nano-field-effect transistors of p-type Zn_{0.3}Cd_{0.7}Te nanoribbons," *Mater. Lett.*, vol. 65, no. 12, pp. 1753–1755, 2011.
- [7] K. C. Mandal; S. H. Kang; M. Choi; A. Mertiri; C. Noblitt; A. Smirnov, "Crystal Growth and Characterization of CdTe and Cd_{0.9}Zn_{0.1}Te for Nuclear Radiation Detectors," *Proc. Mat. Res. Soc. Symp.*, vol. 1038, pp. 39–49, 2008.
- [8] Y. Eisen, A. Shor, and I. Mardor, "CdTe and CdZnTe gamma ray detectors for medical and industrial imaging systems," *Nucl. Instruments Methods Phys. Res. Sect. A Accel. Spectrometers, Detect. Assoc. Equip.*, vol. 428, no. 1, pp. 158–170, 1999.
- [9] G. Yang, A. E. Bolotnikov, Y. Cui, G. S. Camarda, A. Hossain, and R. B. James, "Impurity gettering effect of Te inclusions in CdZnTe single crystals," *J. Cryst. Growth*, vol. 311, no. 1, pp. 99–102, 2008.
- [10] T. Schlesinger, J. Toney, H. Yoon, E. Lee, B. Brunett, L. Franks, and R. James, "Cadmium zinc telluride and its use as a nuclear radiation detector material," *Materials Science and Engineering: R: Reports*, vol. 32, no. 4–5, pp. 103–189, 2001.
- [11] D. R. Lide, *CRC Handbook of Chemistry and Physics, 92nd Edition*, vol. 53. 2011.
- [12] Y. Wang, K. Kudo, Y. Inatomi, R. Ji, and T. Motegi, "Growth interface of CdZnTe grown from Te solution with THM technique under static magnetic field," *J. Cryst. Growth*, vol. 284, no. 3–4, pp. 406–411, 2005.

- [13] G. Sivaraman, "Characterization of cadmium zinc telluride solar cells," Universty of South Florida, 2003.
- [14] H. Bensalah, V. Hortelano, J. L. Plaza, O. Martínez, J. Crocco, Q. Zheng, V. Carcelen, and E. Dieguez, "Characterization of CdZnTe after argon ion beam bombardment," *J. Alloys Compd.*, vol. 543, pp. 233–238, 2012.
- [15] J. Toney, "Ph.D. Thesis," Carnegie Mellon University, 1998.
- [16] M. Isshiki, "Segregation coefficients of Ag, Co, I and in IN CdTe," *J. Cryst. Growth*, vol. 78, pp. 58–62, 1986.
- [17] M. L. Cohen and J. R. Chelikowsky, "Electronic structure and optical properties of semiconductors," *Physics (College. Park. Md.)*, vol. 25, no. 10, pp. 1885–1888, 1988.
- [18] P. Norton, "HgCdTe Infrared Detectors," *Opto-Electronics Rev.*, vol. 10, no. 3, pp. 159–174, 2002.
- [19] T. C. Yu and R. F. Brebrick, "The Hg-Cd-Zn-Te phase diagram," *J. Phase Equilibria*, vol. 13, no. 5, pp. 476–496, 1992.
- [20] J. Brice, "MBI casts wider net for improved breast cancer diagnosis." [Online]. Available: <http://www.auntminnie.com/index.aspx?sec=spt&sub=mbi&pag=dis&itemID=91850>. [Accessed: 12-Mar-2016].
- [21] M. S. Dresselhaus, G. Dresselhaus, X. Sun, Z. Zhang, S. B. Cronin, and T. Koga, "Low-dimensional thermoelectric materials," *Physics of the Solid State*, vol. 41, no. 5. pp. 679–682, 1999.
- [22] I. G. Alexander, "Nanostructured material." [Online]. Available: <http://eng.thesaurus.rusnano.com/wiki/article1371>. [Accessed: 17-Sep-2015].
- [23] B. K. Teo and X. H. Sun, "Silicon-based low-dimensional nanomaterials and nanodevices," *Chemical Reviews*, vol. 107, no. 5. pp. 1454–1532, 2007.
- [24] C. B. Murray, C. R. Kagan, and M. G. Bawendi, "Synthesis and characterization of monodisperse nanocrystals and close-packed nanocrystal assemblies," *Annu. Rev. Mater. Sci.*, vol. 30, pp. 545–610, 2000.
- [25] G. M. Whitesides, "The 'right' size in nanobiotechnology.," *Nat. Biotechnol.*, vol. 21, no. 10, pp. 1161–1165, 2003.
- [26] R. Grisel, K.-J. Weststrate, A. Gluhoi, and B. E. Nieuwenhuys, "Catalysis by Gold Nanoparticles," *Gold Bulletin*, vol. 35, no. 2. pp. 39–45, 2002.
- [27] D. T. Thompson, "Using gold nanoparticles for catalysis," *Nano Today*, vol. 2, no. 4, pp. 40–43, 2007.
- [28] D. Astruc, *Nanoparticles and Catalysis*. 2008.
- [29] Y. Huang, S. C. Lenaghan, L. Xia, J. N. Burris, C. N. Stewart, and M. Zhang, "Characterization of physicochemical properties of ivy nanoparticles for

- cosmetic application.,” *J. Nanobiotechnology*, vol. 11, no. 1, p. 3, 2013.
- [30] R. Minchin, “Nanomedicine: sizing up targets with nanoparticles.,” *Nature nanotechnology*, vol. 3, no. 1. pp. 12–13, 2008.
 - [31] W. Li, Y. Xu, Y. Zhou, W. Ma, S. Wang, and Y. Dai, “Silica nanoparticles functionalized via click chemistry and ATRP for enrichment of Pb(II) ion,” *Nanoscale Research Letters*, vol. 7, no. 1. p. 485, 2012.
 - [32] J. Lee, A. O. Govorov, J. Dulka, and N. A. Kotov, “Bioconjugates of CdTe nanowires and Au nanoparticles: Plasmon-exciton interactions, luminescence enhancement, and collective effects,” *Nano Lett.*, vol. 4, no. 12, pp. 2323–2330, 2004.
 - [33] N. P. Gaponik, D. V. Talapin, A. L. Rogach, and A. Eychmüller, “Electrochemical synthesis of CdTe nanocrystal/polypyrrole composites for optoelectronic applications,” *Journal of Materials Chemistry*, vol. 10, no. 9. pp. 2163–2166, 2000.
 - [34] G. J. Nohynek, J. Lademann, C. Ribaud, and M. S. Roberts, “Grey goo on the skin? Nanotechnology, cosmetic and sunscreen safety.,” *Crit. Rev. Toxicol.*, vol. 37, no. 3, pp. 251–277, 2007.
 - [35] S. R. Pinnell, D. Fairhurst, R. Gillies, M. A. Mitchnick, and N. Kollias, “Microfine zinc oxide is a superior sunscreen ingredient to microfine titanium dioxide,” *Dermatologic Surg.*, vol. 26, no. 4, pp. 309–314, 2000.
 - [36] A. Jantschke, C. Fischer, H. Braun, and E. Brunner, “Directed assembly of nanoparticles to isolated diatom valves using the non-wetting characteristics after pyrolysis,” *Nanoscale*, vol. 6, pp. 1–30, 2014.
 - [37] X. Zhong, Z. Zhang, S. Liu, M. Ban, and W. Knoll, “Embryonic nuclei-induced alloying process for the reproducible synthesis of blue-emitting $\text{Zn}_x\text{Cd}_{1-x}\text{Se}$ nanocrystals with long-time thermal stability in size distribution and emission wavelength,” *J. Phys. Chem. B*, vol. 108, no. 40, pp. 15552–15559, 2004.
 - [38] X. Zhong, M. Han, Z. Dong, T. J. White, and W. Knoll, “Composition-tunable $\text{Zn}_x\text{Cd}_{1-x}\text{Se}$ nanocrystals with high luminescence and stability,” *J. Am. Chem. Soc.*, vol. 125, no. 28, pp. 8589–8594, 2003.
 - [39] Y. Wang, Y. Hou, H. Cui, C. Sun, and Y. Lu, “Controllable Synthesis and Electroluminescence Property of Water-Sol ZnCdTe Alloy for Light-emitting Diodes,” *Int. J. Appl. Phys. Math.*, vol. 1, pp. 167–170, 2011.
 - [40] S. V. N. T. Kuchibhatla, A. S. Karakoti, D. Bera, and S. Seal, “One dimensional nanostructured materials,” *Progress in Materials Science*, vol. 52, no. 5. pp. 699–913, 2007.
 - [41] P. Harrop, K. Ghaffarzadeh, and R. Das, “Energy Harvesting: Off-grid Renewable Power for Devices, Vehicles, Structures 2015-2025,” 2015.
 - [42] A. Purkayastha, Q. Yan, M. S. Raghuveer, D. D. Gandhi, H. Li, Z. W. Liu, R.

- V. Ramanujan, T. Borca-Tasciuc, and G. Ramanath, "Surfactant-directed synthesis of branched bismuth telluride/sulfide core/shell nanorods," *Adv. Mater.*, vol. 20, no. 14, pp. 2679–2683, 2008.
- [43] W. Palosz, S. L. Lehoczky, and F. R. Szofran, "Thermochemical model of physical vapor transport of cadmium-zinc telluride," *J. Cryst. Growth*, vol. 148, no. 1–2, pp. 49–55, 1995.
- [44] A. Haloui, Y. Feutelais and B. Legendre, "Experimental study of ternary system Cd-Zn-Te," *J. Alloys Compd.*, vol. 260, pp. 179–192, 1997.
- [45] S. Li, Y. Jiang, D. Wu, Y. Zhang, J. Li, B. Yang, X. Ding, H. Zhong, L. Chen, and L. Wu, "Synthesis and X-ray responsivity of $\text{Zn}_{0.75}\text{Cd}_{0.25}\text{Te}$ nanoribbons," *Micro Nano Lett.*, vol. 6, no. 8, p. 624, 2011.
- [46] T. Gandhi, "Synthesis and Characterization of CZT Nanowires and its Potential as a Gamma Ray Detector," University of Nevada, Reno, 2008.
- [47] K. Davami, J. Pohl, M. Shaygan, N. Kheirabi, H. Faryabi, G. Cuniberti, J.-S. Lee, and M. Meyyappan, "Bandgap engineering of $\text{Cd}_{(x)}\text{Zn}_{(1-x)}\text{Te}$ nanowires.," *Nanoscale*, vol. 5, no. 3, pp. 932–5, 2013.
- [48] D. Pradhan and K. T. Leung, "Vertical growth of two-dimensional zinc oxide nanostructures on ITO-coated glass: Effects of deposition temperature and deposition time," *J. Phys. Chem. C*, vol. 112, no. 5, pp. 1357–1364, 2008.
- [49] E. Yilmaz, "An Investigation of CdZnTe Thin Films for Photovoltaics," *Energy Sources, Part A: Recovery, Utilization, and Environmental Effects*, vol. 34, no. 4, pp. 332–335, 2011.
- [50] A. Morales-Acevedo, "Analytical model for the photocurrent of solar cells based on graded band-gap CdZnTe thin films," *Sol. Energy Mater. Sol. Cells*, vol. 95, no. 10, pp. 2837–2841, 2011.
- [51] Y. G. Xiao, K. Uehara, M. Lestrade, Z. Q. Li, and Z. M. S. Li, "Modeling of SI-based thin film triple-junction solar cells," in *Conference Record of the IEEE Photovoltaic Specialists Conference*, 2009, pp. 002154–002158.
- [52] I. K. El Zawawi and M. a. Mahdy, "Air-stable $\text{Cd}_{0.23}\text{Zn}_{0.77}\text{Te}$ nanostructure thin films," *J. Mater. Sci. Mater. Electron.*, vol. 26, no. 3, pp. 1950–1958, 2015.
- [53] G. Zha, H. Zhou, J. Gao, T. Wang, and W. Jie, "The growth and the interfacial layer of CdZnTe nano-crystalline films by vacuum evaporation," *Vacuum*, vol. 86, no. 3, pp. 242–245, 2011.
- [54] M. E. Tuckerman, *Statistical Mechanics: Theory and Molecular Simulation*. 2010.
- [55] S. Nosé, "A unified formulation of the constant temperature molecular dynamics methods," *J. Chem. Phys.*, vol. 81, no. 1, pp. 511–519, 1984.
- [56] W. G. Hoover, "Canonical dynamics: Equilibrium phase-space distributions,"

- Phys. Rev. A*, vol. 31, no. 3, pp. 1695–1697, 1985.
- [57] L. Verlet, “Computer ‘experiments’ on classical fluids. I. Thermodynamical properties of Lennard-Jones molecules,” *Phys. Rev.*, vol. 159, no. 1, pp. 98–103, 1967.
 - [58] L. Verlet, “Computer ‘experiments’ on classical fluids. II. Equilibrium correlation functions,” *Phys. Rev.*, vol. 165, no. 1, pp. 201–214, 1968.
 - [59] A. Rahman, “Correlations in the motion of atoms in liquid argon,” *Phys. Rev.*, vol. 136, p. A405, 1964.
 - [60] A. Nordsieck, “On Numerical Integration of Ordinary Differential Equations,” *Math. Comput.*, vol. 16, pp. 22–49, 1962.
 - [61] C. W. Gear, *Numerical Initial Value Problems in Ordinary Differential Equations*. Prentice-Hall, EnglewoodCliffs, NJ, USA, 1971.
 - [62] C. Lanczos, “An iteration method for the solution of the eigenvalue problem of linear differential and integral operators,” *J Res Natl Bur Stand*, vol. 45, pp. 255–282, 1950.
 - [63] Y. Saad, *Iterative methods for sparse linear systems*. PWS, Boston, 1996.
 - [64] R. Haydock, “The Recursive solution of Schrodinger Equation,” in *Solid State Physics*, vol. 35, no. C, 1980, pp. 216–294.
 - [65] R. Haydock, V. Heine, and M. J. Kelly, “Electronic structure based on the local atomic environment for tight-binding bands,” *J. Phys. C Solid State Phys.*, vol. 5, no. 20, pp. 2845–2858, 1972.
 - [66] D. K. Ward, X. W. Zhou, B. M. Wong, F. P. Doty, and J. A. Zimmerman, “Analytical bond-order potential for the cadmium telluride binary system,” *Phys. Rev. B - Condens. Matter Mater. Phys.*, vol. 85, no. 11, pp. 1–19, 2012.
 - [67] D. Brenner, “Empirical potential for hydrocarbons for use in simulating the chemical vapor deposition of diamond films,” *Phys. Rev. B*, vol. 42, no. 15, pp. 9458–9471, 1990.
 - [68] J. Lennard-Jones, “Cohesion,” *Proc. Phys. Soc.*, vol. 43, p. 461, 1931.
 - [69] J. Tersoff, “New empirical approach for the structure and energy of covalent systems,” *Phys. Rev. B*, vol. 37, no. 12, pp. 6991–7000, 1988.
 - [70] J. E. Lennard-Jones, “Perturbation problems in quantum mechanics,” *Proc. Roy. Soc. London Ser. A*, vol. 129, pp. 598–615, 1930.
 - [71] B. M. Axilrod and E. Teller, “Interaction of the Van der Waals type between three atoms,” *Chem. Phys.*, vol. 11, pp. 299–300, 1943.
 - [72] Ş. Erkoç and H. Oymak, “AlTiNi ternary alloy clusters: Molecular dynamics simulations and density functional theory calculations,” *J. Phys. Chem. B*, vol. 107, no. 44, pp. 12118–12125, 2003.

- [73] H. Oymak and Ş. Erkoç, “Structural and electronic properties of $\text{Al}_k\text{Ti}_l\text{Ni}_m$ microclusters: Density-functional-theory calculations,” *Phys. Rev. A*, vol. 66, no. 3, p. 033202, 2002.
- [74] A. İnce and Ş. Erkoç, “Silicene nanoribbons: Molecular-dynamics simulations,” *Comput. Mater. Sci.*, vol. 50, no. 3, pp. 865–870, 2011.
- [75] B. Özdamar and Ş. Erkoç, “Structural properties of silicon nanorods under strain: Molecular dynamics simulations,” *J. Comput. Theor. Nanos.*, vol. 10, pp. 1–9, 2013.
- [76] R. J. Sadus, “Exact calculation of the effect of three-body Axilrod–Teller interactions on vapour–liquid phase coexistence,” *Fluid Phase Equilib.*, vol. 144, pp. 351–360, 1998.
- [77] L. Amirouche and Ş. Erkoç, “Structural features and energetics of Zn_kCd_l microclusters,” *J. Mod. Phys. C*, vol. 14, pp. 905–910, 2003.
- [78] S. K. Bhattacharya and A. Kshirsagar, “Ab initio calculations of structural and electronic properties of CdTe clusters,” *Phys. Rev. B*, vol. 75, no. 3, p. 35402, 2007.
- [79] G. K. P. Huber, and G. Herzberg, *Molecular Spectra and Molecular Structures: Constants of Diatomic Molecules*. Van Nostrand Reinhold Co., New York, 1979.
- [80] O. Babaky and K. Hussein, “Molecular constants of $^{128}\text{Te}_2$,” *Can. J. Phys.*, vol. 69, p. 57, 1991.
- [81] R. Drautz, D. A. Murdick, D. Nguyen-Manh, X. Zhou, H. N. G. Wadley, and D. G. Pettifor, “Analytic bond-order potential for predicting structural trends across the sp-valent elements,” *Phys. Rev. B*, vol. 72, no. 14, p. 144105, 2005.
- [82] D. G. Pettifor and I. I. Oleinik, “Analytic bond-order potential for open and close-packed phases,” *Phys. Rev. B*, vol. 65, no. 17, p. 172103, 2002.
- [83] D. G. Pettifor and I. I. Oleinik, “Bounded Analytic Bond-Order Potentials for sigma and pi Bonds,” *Phys. Rev. Lett.*, vol. 84, no. 18, p. 4124, 2000.
- [84] D. Pettifor, M. Finnis, D. Nguyen-Manh, D. Murdick, X. Zhou, and H. N. Wadley, “Analytic bond-order potentials for multicomponent systems,” *Mater. Sci. Eng. A*, vol. 365, no. 1–2, pp. 2–13, 2004.
- [85] P. Horsfield, M. Bratkovsky, M. Fearn, D. G. Pettifor, and M. Aoki, “Bond-order potentials: Theory and implementation,” *Phys. Rev. B*, vol. 53, no. 19, pp. 12694–12712, 1996.
- [86] D. G. Pettifor and I. I. Oleinik, “Analytic bond-order potentials beyond Tersoff-Brenner. I. Theory,” *Phys. Rev. B*, vol. 59, no. 13, p. 8487, 1999.
- [87] D. K. Ward, X. W. Zhou, B. M. Wong, F. P. Doty, and J. A. Zimmerman, “Analytical bond-order potential for the Cd-Zn-Te ternary system,” *Phys. Rev.*

- B*, vol. 86, no. 24, p. 245203, 2012.
- [88] “LAMMPS,” 2015. [Online]. Available: <http://lammmps.sandia.gov/download>. [Accessed: 27-Sep-2015].
 - [89] “Periodic boundary condition,” 2015. [Online]. Available: <http://www.compsoc.man.ac.uk/~lucky/Democritus/Theory/pbc-mi.html>. [Accessed: 27-Sep-2015].
 - [90] R.G. Parr and W. Yang, *Density-Functional Theory of Atoms and Molecules*. Oxford University Press, New York, 1989.
 - [91] J.K. Labanowski and J.W. Andzelm, *Density-Functional Methods in Chemistry*. New York: Springer, 1991.
 - [92] M. Born and R. Oppenheimer, “Zur quantentheorie der molekeln,” *Ann. Phys.*, vol. 20, no. 84, pp. 457–484, 1927.
 - [93] D. R. Hartree, “The Wave Mechanics of an Atom with a Non-Coulomb Central Field. Part II. Some Results and Discussion,” *Math. Proc. Cambridge Philos. Soc.*, vol. 24, no. 01, p. 111, 1928.
 - [94] V. Fock, “First publication on hartree-fock method,” *Z. Phys*, vol. 61, p. 126, 1930.
 - [95] P.Hohenberg and W. Kohn, “Inhomogeneous Electron Gas,” *Phys. Rev.*, pp. B864–B871, 1964.
 - [96] W. Kohn and L. J. Sham, “Self-consistent equations including exchange and correlation effects,” *Phys. Rev.*, vol. 140, no. 4A, 1965.
 - [97] M. R. Dreizler and E. K. U. Gross, in *Density Functional Theory and Its Application to Materials*, AIP Press. Melville, New York, 2001.
 - [98] John R. Smith, “Beyond the local- density approximation surface properties of (110) W,” *Phys. Rev. Lett.*, vol. 25, no. 15, pp. 1023–1026, 1970.
 - [99] J.P. Perdew and Alex Zunger, “Self-interaction correction to density-functional approximations for many-electron systems,” *Phys. Rev. A*, vol. 23, pp. 5048–5079, 1981.
 - [100] J. P. Perdew and Y. Wang, “Accurate and simple analytic representation of the electron-gas correlation energy,” *Physical Review B*, vol. 45, no. 23. pp. 13244–13249, 1992.
 - [101] S. H. Vosko, L. Wilk, and M. Nusair, “Accurate spin-dependent electron liquid correlation energies for local spin density calculations: a critical analysis,” *Can. J. Phys.*, vol. 58, no. 8, pp. 1200–1211, 1980.
 - [102] J. P. Perdew, K. Burke, and M. Ernzerhof, “Generalized Gradient Approximation Made Simple,” *Phys. Rev. Lett.*, vol. 77, no. 18, pp. 3865–3868, 1996.

- [103] J. P. Perdew; P. Ziesche and H. Eschrig, *Electronic structure of solids* '91, vol. 11. Akademie Verlag, Berlin, 1991.
- [104] C. Lee, W. Yang, and R. G. Parr, "Development of the Colle-Salvetti correlation-energy formula into a functional of the electron density," *Phys. Rev. B*, vol. 37, no. 2, pp. 785–789, 1988.
- [105] J. P. Perdew, "Density-functional approximation for the correlation energy of the inhomogeneous electron gas," *Phys. Rev. B*, vol. 33, no. 12, pp. 8822–8824, 1986.
- [106] M. Losada and S. Leutwyler, "Water hexamer clusters: Structures, energies, and predicted mid-infrared spectra," *J. Chem. Phys.*, vol. 117, no. 5, pp. 2003–2016, 2002.
- [107] S. Tsuzuki and H. P. Lüthi, "Interaction energies of van der Waals and hydrogen bonded systems calculated using density functional theory: Assessing the PW91 model," *J. Chem. Phys.*, vol. 114, no. 9, pp. 3949–3957, 2001.
- [108] J. Ireta, J. Neugebauer, and M. Scheffler, "On the accuracy of DFT for describing hydrogen bonds: Dependence on the bond directionality," *J. Phys. Chem. A*, vol. 108, no. 26, pp. 5692–5698, 2004.
- [109] J. Tao, J. P. Perdew, V. N. Staroverov, and G. E. Scuseria, "Climbing the density functional ladder: nonempirical meta-generalized gradient approximation designed for molecules and solids.," *Phys. Rev. Lett.*, vol. 91, no. 14, p. 146401, 2003.
- [110] G. I. Csonka, J. P. Perdew, A. Ruzsinszky, P. H. T. Philipsen, S. Lebégue, J. Paier, O. A. Vydrov, and J. G. Ángyán, "Assessing the performance of recent density functionals for bulk solids," *Phys. Rev. B - Condens. Matter Mater. Phys.*, vol. 79, no. 15, 2009.
- [111] V. N. Staroverov, G. E. Scuseria, J. Tao, and J. P. Perdew, "Comparative assessment of a new nonempirical density functional: Molecules and hydrogen-bonded complexes," *J. Chem. Phys.*, vol. 119, no. 23, pp. 12129–12137, 2003.
- [112] Y. Zhao and D. G. Truhlar, "Benchmark databases for nonbonded interactions and their use to test density functional theory," *J. Chem. Theory Comput.*, vol. 1, no. 3, pp. 415–432, 2005.
- [113] A. D. Becke, "Density Functional Thermochemistry III The Role of Exact Exchange," *J. Chem. Phys.*, vol. 98, pp. 5648–5652, 1993.
- [114] J. Perdew, K. Burke, and Y. Wang, "Generalized gradient approximation for the exchange-correlation hole of a many-electron system," *Phys. Rev. B*, vol. 54, no. 23, pp. 16533–16539, 1996.
- [115] A. D. Becke, "Density-functional thermochemistry. IV. A new dynamical correlation functional and implications for exact-exchange mixing," *J. Chem. Phys.*, vol. 104, no. 3, pp. 1040–1046, 1996.

- [116] A. D. Becke, "Density-functional exchange-energy approximation with correct asymptotic behavior," *Phys. Rev. A*, vol. 38, no. 6, pp. 3098–3100, 1988.
- [117] Y. Zhao and D. G. Truhlar, "Design of density functionals that are broadly accurate for thermochemistry, thermochemical kinetics, and nonbonded interactions," *J. Phys. Chem. A*, vol. 109, no. 25, pp. 5656–5667, 2005.
- [118] Y. Zhao and D. G. Truhlar, "Hybrid meta density functional theory methods for thermochemistry, thermochemical kinetics, and noncovalent interactions: The MPWB1B95 and MPWB1K models and comparative assessments for hydrogen bonding and van der Waals interactions," *J. Phys. Chem. A*, vol. 108, no. 33, pp. 6908–6918, 2004.
- [119] W. J. Stevens, H. Basch, and M. Krauss, "Compact effective potentials and efficient shared-exponent basis sets for the first- and second-row atoms," *J. Chem. Phys.*, vol. 81, no. 12, pp. 6026–6033, 1984.
- [120] T. R. Cundari and W. J. Stevens, "Effective core potential methods for the lanthanides," *J. Chem. Phys.*, vol. 98, no. 7, pp. 5555–5565, 1993.
- [121] Ş. Erkoç, "Interaction of Nitric Oxide with elements," *J. Mol. Struct. THEOCHEM*, vol. 574, pp. 127–132, 2001.
- [122] J. E. Bernard and A. Zunger, "Electronic structure of ZnS, ZnSe, ZnTe, and their pseudobinary alloys," *Phys. Rev. B*, vol. 36, no. 6, pp. 3199–3228, 1987.
- [123] B. Segall, M. Lorenz, and R. Halsted, "Electrical Properties of n-Type CdTe," *Phys. Rev.*, vol. 129, no. 6, pp. 2471–2481, 1963.
- [124] M. J. Frisch, G. W. Trucks, H. B. Schlegel, G. E. Scuseria, M. A. Robb, J. R. Cheeseman, G. Scalmani, V. Barone, B. Mennucci, G. A. Petersson, H. Nakatsuji, M. Caricato, X. Li, H. P. Hratchian, A. F. Izmaylov, J. Bloino, G. Zheng, J. L. Sonnenberg, M. Hada, M. Ehara, K. Toyota, R. Fukuda, J. Haseg, "Gaussian09, Revision B.01," *Gaussian Inc., Wallingford, CT*, 2010.
- [125] T. K. and J. M. Roy Dennington, "GaussView, Version 5," *Semichem Inc., Shawnee Mission KS*,. 2009.
- [126] C. Wang, S. Xu, L. Ye, W. Lei, and Y. Cui, "Investigation of $Zn_mCd_nX_y$ ($y = m + n$; $X = Te, Se$ and S) Clusters with TDDFT Method," *J. Clust. Sci.*, vol. 22, no. 1, pp. 49–58, 2011.
- [127] F. Schautz and M. Dolg, "Regular article Quantum Monte Carlo study of Be_2 and group 12 dimers M_2 ($M = Zn, Cd, Hg$)," *J. Chem. Physics*, vol. 2, pp. 231–240, 1998.
- [128] M. A. Czajkowski and J. Koperski, " Cd_2 and Zn_2 van der Waals dimers revisited. Correction for some molecular potential parameters," *Spectrochim. Acta - Part A Mol. Biomol. Spectrosc.*, vol. 55, no. 11, pp. 2221–2229, 1999.
- [129] S. Biernacki, U. Scherz, and C. Schrepel, "Local vibrational modes and anharmonic forces of Mg^{2+} and S^{2-} in ZnTe and CdTe crystals," *Phys. Rev. B*,

- vol. 56, no. 8, pp. 4592–4596, 1997.
- [130] P. Hassanzadeh, C. Thompson, and L. Andrews, “Absorption Spectra of Tellurium Clusters in Solid Argon,” *Society*, no. Figure li, pp. 8246–8249, 2000.
 - [131] J. Wang, L. Ma, J. Zhao, and K. A. Jackson, “Structural growth behavior and polarizability of $\text{Cd}_{(n)}\text{Te}_{(n)}$ ($n=1-14$) clusters,” *J. Chem. Phys.*, vol. 130, no. 21, p. 214307, 2009.
 - [132] K. Iokibe, H. Tachikawa, and K. Azumi, “A DFT study on the structures and electronic states of zinc cluster Zn_n ($n = 2-32$),” *J. Phys. B At. Mol. Opt. Phys.*, vol. 40, no. 2, pp. 427–436, 2007.
 - [133] J. Lv, Y. Wang, L. Zhang, H. Lin, J. Zhao, and Y. Ma, “Stabilization of fullerene-like boron cages by transition metal encapsulation,” *Nanoscale*, vol. 7, no. 23, pp. 10482–10489, 2015.
 - [134] G. H. Wu, Q. M. Liu, and X. Wu, “Geometrical and energetic properties in 38-atom trimetallic AuPdPt clusters,” *Chem. Phys. Lett.*, vol. 620, pp. 92–97, 2015.
 - [135] H. H. Kart, H. Yildirim, S. Ozdemir Kart, and T. Çağın, “Physical properties of Cu nanoparticles: A molecular dynamics study,” *Mater. Chem. Phys.*, vol. 147, no. 1–2, pp. 204–212, 2014.
 - [136] M. E. Rodriguez; et al., “On the Thermal and Structural Properties of $\text{Cd}_{1-x}\text{Zn}_x\text{Te}$ in the Range $0 < x < 0.3$,” vol. 67, pp. 67–72, 1996.
 - [137] N. M. O’Boyle, A. L. Tenderholt, and K. M. Langner, “cclib: A Library for Package-Independent Computational Chemistry Algorithms,” *J. Comput. Chem.*, vol. 29, no. 5, pp. 839–845, 2008.
 - [138] G. E. Hallani, A. Ryah, N. Hassanain, M. Loghmarti, A. Mzerd, and A. Arbaoui, “Optical Properties of Thin Ternary Semiconductor Alloys CdZnTe Prepared by Hot Wall Evaporation Technique,” *Proc. Prog. Electromagn. Res. Symp.*, no. March, pp. 1897–1899, 2011.
 - [139] M. Kurban and Ş. Erkoç, “Structural properties of $\text{Zn}_x\text{Cd}_{1-x}\text{Te}$ ($x= 0.25, 0.50$ and 0.75) ternary nanorods: Molecular Dynamics Simulations,” *Res. Rev. J. Pure Appl. Phys.*, vol. 1, pp. 35–42, 2013.
 - [140] M. Kurban and Ş. Erkoç, “Investigation of the Structural Properties of CdTe and ZnTe Binary Nanorods Under Heat Treatment: Molecular Dynamics Simulations,” vol. 5, no. 4, pp. 1–5, 2016.
 - [141] M. Kurban and Ş. Erkoç, “Mechanical properties of CdZnTe nanowires under uniaxial stretching and compression: A molecular dynamics simulation study.”(submitted for publication).
 - [142] M. Kurban and Ş. Erkoç, “Structural and Electronic Properties of $\text{Zn}_m\text{Cd}_n\text{Te}_k$ ($m+n+k = 2-4$) Clusters: DFT Calculations,” *J. Comput. Theor. Nanosci.*, vol. 12, no. 9, pp. 2605–2615, 2015.

- [143] M. Kurban and Ş. Erkoç, “Structural, electronic, thermal and vibrational properties of AB_6C_8 ternary CdZnTe cubic nanoparticles: DFT calculations and MD simulations.”(submitted for publication).
- [144] M. Kurban, O. Barış Malcioğlu and Ş. Erkoç, “Structural and thermal properties of Cd-Zn-Te ternary nanoparticles: Molecular-dynamics simulations,” *Chem. Phys.*, vol. 464, pp. 40–45, 2016.

CURRICULUM VITAE

PERSONAL INFORMATION

Surname, Name: Kurban, Mustafa

Nationality: Turkish (TC)

Date and Place of Birth: 16 January 1984, Malatya

Marital Status: Married

Phone: +90 554 344 48 34

Email: mkurbanphys@gmail.com

EDUCATION

Degree	Institution	Year of Graduation
MS	FU Department of Physics	2010
BS	FU Department of Physics	2007
High School	Malatya High School, Malatya	2001

WORK EXPERIENCE

Year	Place	Enrollment
2010-Present	METU Department of Physics	Research Assistant
2009-2010	FU Department of Physics	Research Assistant
2008-2009	MŞU Department of Physics	Research Assistant

FOREIGN LANGUAGES

English (fluent), Turkish (native)

PUBLICATIONS

1. F. Gogtas, R. Tutuk and M. Kurban., Time-Dependent Quantum Study of $H(^2S)+FO(^2\Pi)\rightarrow OH(^2\Pi)+F(^2P)$ Reaction on the $1^3A'$ and $1^3A''$ States, J. Comp. Chem. 31, 2607 (2010).
2. M. Kurban, F. Gogtas, E. Karabulut and R. Tutuk Quantum Real Wave Packet Study of $H(^2S)+FO(^2\Pi)\rightarrow HF(^1\Sigma^+)+O(^3P)$ Reaction on the $1^3A'$ State, J. Mol. Phys. 109, 789 (2011).
3. M. Kurban and Ş. Erkoç, "Structural properties of $Zn_xCd_{1-x}Te$ ($x=0.25, 0.50$ and 0.75) ternary nanorods: Molecular Dynamics Simulations", Res. Rev. J. Pure Appl. Phys. 1, 35 (2013).
4. M. Kurban and Ş. Erkoç, Structural and electronic properties of $Zn_mCd_nTe_k$ ($m+n+k=2-4$) clusters: DFT calculations, J. Comput. Theoret. Nanosci. 12, 1-11 (2015).
5. M. Kurban and Ş. Erkoç, Investigation of the structural properties of CdTe and ZnTe binary nanorods under heat treatment: Molecular Dynamics Simulations, Quantum Matter, 5, 1-5 (2016).
6. M. Kurban, O. Baris Malcıoğlu and Ş. Erkoç, Structural and Thermal properties of Zn-Cd-Te ternary nanoparticles: Molecular-Dynamics Simulations, Chemical Physics, 464, 40-45 (2016).
7. M. Kurban and Ş. Erkoç, Structural, electronic, thermal and vibrational properties of AB_6C_8 ternary CdZnTe cubic nanoparticles: DFT calculations and MD simulations, (submitted for publication).
8. M. Kurban and Ş. Erkoç, Mechanical properties of CdZnTe nanowires under uniaxial stretching and compression: A molecular dynamics simulation study, (submitted for publication).

PROCEEDINGS PRESENTED IN NATIONAL AND INTERNATIONAL MEETINGS

- 1- M. Kurban, E. Karabulut, R. Tutuk and F. Gogtas, Quantum Wave Packet Study of D+FO Reaction, TFD26, 24-27 September 2009, Bodrum, Book of Abstracts, p. 316.
- 2- M. Kurban, E. Karabulut, R. Tutuk and F. Gogtas, The investigation of Photo-Dissociation by Time Dependent Quantum Method, TFD26, 24-27 September 2009, Bodrum, Book of Abstracts, p. 317.
- 3- R. Tutuk, E. Karabulut, M. Kurban and F. Gogtas., Time Dependent Quantum Study of the $H(^2S) + FO(^2\Pi) \rightarrow OH(^2\Pi) + v F(^2P)$ Reaction, TFD26, 24-27 September 2009, Bodrum, Book of Abstracts, p. 339.
- 4- E. Karabulut, M. Kurban, R. Tutuk and F. Gogtas., Quantum Dynamics Study of $H + LiF$ reaction, Turkish Physical Society 27th International Physics Congress, 14-17 September 2010, İstanbul, Book of Abstracts, p. 457.
- 5- E. Karabulut, M. Kurban, R. Tutuk and F. Gogtas., Isotope effects in the $X + LiF \rightarrow XF + Li$ ($X = H, D$) reaction, Turkish Physical Society 27th International Physics Congress, 14-17 September 2010, İstanbul, Book of Abstracts, p. 458.
- 6- R. Tutuk, E. Karabulut, M. Kurban and F. Gogtas., Quantum Wave Packet Study of the $H + CaCl(v, j) \rightarrow HCl(v', j') + Ca$ Reaction, Turkish Physical Society 27th International Physics Congress, İstanbul, 14-17 September 2010, İstanbul, Book of Abstracts, p. 88.
- 7- M. Kurban, E. Karabulut, R. Tutuk and F. Gogtas., Quantum Real Wave packet Study of $H(^2S) + FO(^2\Pi) \rightarrow HF(^1\Sigma^+) + O(^3P)$ Reaction on the $1^3A'$ State, Turkish Physical Society 27th International Physics Congress, 14-17 September 2010, İstanbul, Book of Abstracts, p. 468.
- 8- M. Kurban, F. Gogtas, E. Karabulut and R. Tutuk., Time-Dependent Quantum Dynamics study of Reactive Scattering of the $H + OF$ Reaction on the $1^3A'$ and $1^3A''$ States, Turkish Physical Society 27th International Physics Congress, 14-17 September 2010, İstanbul, Book of Abstracts, p. 469.

- 9- M. Kurban and F.Gogtas, Quantum Wave Packet Calculation of Reaction Probabilities, Cross Section and Rate Constant for H+FO System on the $1^1A'$ State, Turkish Physical Society 27th International Physics Congress, 14-17 September 2010, İstanbul, Book of Abstracts, p. 471.
- 10- M. Kurban, E. Karabulut and F. Gogtas, Time- Dependent Quantum Study of the Reaction of Hydrogen Isotopes and Flouroxide Molecule, Turkish Physical Society 27th International Physics Congress, 14-17 September 2010, İstanbul, Book of Abstracts, p. 470.
- 11- M. Kurban and Ş. Erkoç, Structural properties of $Zn_xCd_{1-x}Te$ ($x=0.25$ and 0.50) nanorods: NanoTR8, 25-28 June 2012, Hacettepe University, Ankara. Abstract Book, PP-234.
- 12- M. Kurban and Ş. Erkoç, Structural properties of ZnTe and CdTe binary nanorods: Molecular Dynamics Simulations, 30th International Physics Congress, 2-5 September 2013, Istanbul, Turkey, p. 371.
- 13- M. Kurban and Ş. Erkoç, Structural and electronic properties of $Zn_mCd_nTe_k$ ($m+n+k=2-4$) clusters: Density functional theory calculations, NanoTR9, 24-28 June 2013, Ataturk University, Erzurum, Abstract Book, p. 124.
- 14- M. Kurban, O. B. Malcıoğlu and Ş. Erkoç, "Size dependence and heat capacity of CdZnTe and CdZn nanoparticles: Molecular dynamics simulations", TFD31, 21-24 July 2014, Bodrum. Book of Abstracts, p. 295.
- 15- M. Kurban, O. B. Malcıoğlu and Ş. Erkoç, "A molecular dynamics study of the heat capacity of CdTe and ZnTe nanoparticles", TFD31, 21-24 July 2014, Bodrum. Book of Abstracts, p. 296.
- 16- M. Kurban and Ş. Erkoç, "Proper Gaussian basis sets for density functional studies of cobalt oxide clusters", TFD31, 21-24 July 2014, Bodrum. Book of Abstracts, p. 297.
- 17- M. Kurban, O. B. Malcıoğlu and Ş. Erkoç, " $Zn_xCd_yTe_z$ Nanoparçacıklarının Termodinamik Özelliklerinin Moleküler Dinamiği Benzetimi ile incelenmesi", 20. Yoğun Madde Fiziği Ankara Toplantısı, 26 Aralık 2014, Ankara. Özet Kitabı, sayfa P16.

- 18- M. Kurban, and Ş. Erkoç, "Geometrical and energetic properties of 15-atom ternary Cd-Zn-Te clusters", 9th International Physics Conference of the Balkan Physical Union, 24-27 August 2015, Istanbul. Book of Abstract, p.373.